Opto-acoustic thin-film transducers for imaging of Brillouin oscillations on living cells

Fernando Pérez Cota

A thesis presented for the degree of

Doctor of Philosophy

Faculty of Engineering

The University of Nottingham

2015

UNITED KINGDOM · CHINA · MALAYSIA

I would like to dedicate this thesis to my wife who brings the best out of me...

Acknowledgements

I would like to acknowledge and give my sincere gratitude to CONACYT for sponsoring my doctoral studies. I would like to thank Prof Matt Clark for the opportunity offered to undertake this project, his support and guidance. Thank to Dr. Kevin Webb for his support and for his constant contributions to the application of the work carried out here. I would also like to express thanks to Dr. Richard Smith for taking part in the supervision of this project, the many hours of discussion and the one-to-one support fundamental for the success of the work presented here. To my family, who supported me and encouraged this endeavour, I offer special thanks. Finally, I would like to acknowledge the colleges in the Applied Optics Group from the Faculty of engineering who always had disposition to share their time or resources for the sake of science.

Achievements

The work presented in this thesis has been disseminated in several national and international publications and oral presentations.

Publications:

- **Thin-film optoacoustic transducers for subcellular Brillouin oscillation imaging of individual biological cells** F Pérez Cota, R. J. Smith, E. Moradi, L. Marques K. F. Webb and M. Clark. *Appl. Opt.*, 54(28):8388, 2015.
- **Thin-film transducers for the detection and imaging of Brillouin oscillations in transmission on cultured cells** F Pérez Cota, R. J. Smith, E. Moradi, K. F. Webb and M. Clark. *JPCS* 684, AFPAC 2015
- **Optically excited nanoscaled ultrasonic transducers**, Smith R. J. , Pérez-Cota F., Marques L., Xuesheng C., Ahmet A., Webb K, Aylott J., Somekh M. G. and Clark M., *J. Acoust. Soc. Am.* 137(1) 2015.

Oral presentations:

- **Cell imaging based on Brillouin oscillations detection in transmission using thin-film transducers** F Pérez Cota, R. J. Smith, E. Moradi, L. Marques, K. F. Webb and M. Clark. LU (2015) oral presentation.
- **Thin-film transducers for detection in transmission of Brillouin scattering for imaging of cultured cells** F Pérez Cota, R. J. Smith, E. Moradi, L. Marques K. F. Webb and M. Clark. AFPAC (2015).
- **Design and application of nano-scaled ultrasonic transducers** F. Pérez Cota, R.J. Smith, L. Marques, K. F. Webb and M. Clark. RCNDE ERS Glasgow (2014), oral presentation.
- **Design and application of nano-scaled transducers** F. Pérez Cota, R.J. Smith, K. F. Webb and M. Clark. IOP Optics and Ultrasound II day meeting at The University of Nottingham (2014), oral presentation.
- **Nano-scale transducers for picosecond ultrasonics in living cells** LU (2013) oral presentation. F Pérez Cota, R. J. Smith, K. F. Webb and M. Clark.

- **Brillouin imaging of cultured cells using picosecond laser ultrasound** R. J. Smith, F. Pérez Cota, L. Marques, K. F. Webb and M. Clark. IOP Optics and Ultrasound day meeting at The University of Nottingham (2013).
- **Nano-scale transducers for picosecond ultrasound in living cells** F. Pérez Cota, R. J. Smith, K. F. Webb and M. Clark. AFPAC (2013).

Abstract

In any given media, the speed of sound is considerably slower than speed of light, and the exploration of the acoustic regime in the GHz range gives access to very short acoustic wavelengths. Short acoustic wavelengths is an intriguing path for high resolution live-cell imaging. At low frequencies, ultrasound has proved to be a valuable tool for the mechanical characterisation and imaging of biological tissues. There is much interest in using high frequency ultrasound to investigate single cells due to its mechanical contrast mechanism. Mechanical characterisation of cells has been performed by a number of techniques, such as atomic force microscopy, acoustic microscopy or Brillouin microscopy. Recently, Brillouin oscillations measurements on vegetal and mammal cells have been demonstrated in the GHz range. In this thesis, a method to extend this technique, from the previously reported single point measurements and line scans, into a high resolution acoustic imaging tool is presented. A novel approach based around a three-layered metal-dielectric-metal film is used as a transducer to launch acoustic waves into the cell being studied. The design of this transducer and imaging system is optimised to overcome the vulnerability of a cell to the exposure of laser light and heat without sacrificing the signal to noise ratio. The transducer substrate shields the cell from the laser radiation by detecting in transmission rather than reflection. It also generates acoustic waves efficiently by a careful selection of materials and wavelengths. Facilitates optical detection in transmission due to simplicity of arrangement and aids

to dissipate heat away from the cell. The design of the transducers and instrumentation is discussed and Brillouin frequency images (two and three dimensions) on phantom, fixed and living cells are presented.

Contents

List of Figures

Chapter 1

Introduction

The following thesis explores the use of picosecond laser ultrasound (PLU) for live cell imaging. Techniques to image the mechanical properties of living cells with sub-optical resolution are very limited. In this thesis I present a novel method for the detection of Brillouin oscillations to perform acoustic imaging on living cells, where the in-depth resolution is higher than optical due to the use of short ultrasound wavelengths. This is accomplished by performing PLU measurements using a specially designed three layer thin-film transducer. The transducer protects the cell against laser exposure while increasing signal amplitude. As a result two or three dimensional images of the Brillouin frequency were obtained on phantom, fixed and living cells.

1.1 Introduction to cells

Biological cells are the building block of living tissue[1]. Their structure and function governs the behaviour and appearance of every known living organism. Cells are comprised of subcompartments, and there is an immense amount of diversity of cell types not just from species to species but also within individual organisms. The cells inside

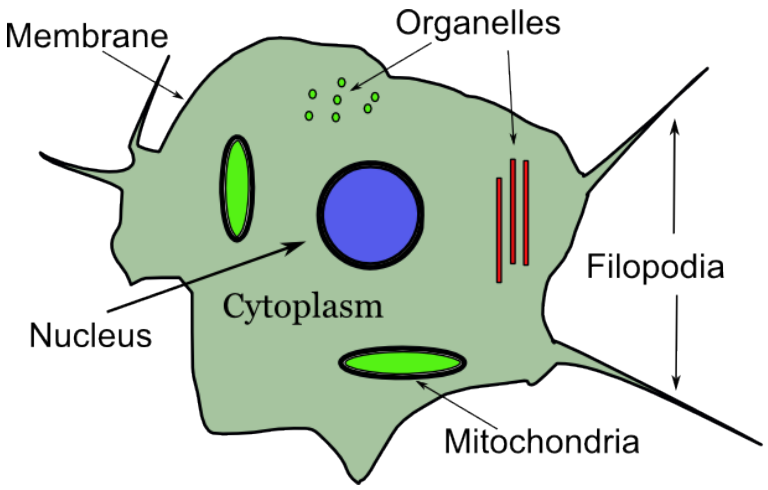

Figure 1.1: Basic diagram of a biological cell. This generic diagram is representative of a eukaryotic cells present in plant and animals.

our body are a source of information to understand diseases and disorders that affect millions of people all over the world. Deeper understanding could lead to developing new break through technologies from which all people could benefit. However, understanding the function and behaviour of cells is a challenging task which is the subject of much research.

Cells are composed of many structures and substructures which can be categorised into three main parts; the membrane which separates the cell from the exterior, the organelles (including the nucleus) and the cytoplasm that consist of a watery substance called cytosol in which the organelles are suspended (see figure 1.1). A cell is also constituted by many compounds like water, carbohydrates, amino acids and lipids. This complexity makes a cell a very interesting and challenging subject for imaging optically or mechanically.

1.2 Introduction to microscopy

The invention of the magnifying glass allowed the invention of the telescope which opened the skies for observation. Similarly, the microscope opened a window for the world of the very small. In the middle of the seventeenth century, Robert Hooke published drawings of what he observed with his microscope and used the word cell to describe the structures he saw in the sections of cork[2]. Soon after, Antonie Van Leeuwenhoek improved the microscope by fabricating better spherical lenses and made the first description of microorganisms[3]. One of his students (Nicolas Hartsoeker) believed that tiny humans were present within sperm cells. This gives an idea of how much the knowledge of microorganisms depends on what people saw under the microscope. By the middle of the nineteenth century modern cell theory, which states that all living organisms are made out of cells and that they are the building block of life, was born with the work of Mattias Schleiden and Theodor Schwaan. At a similar time, Louis Pasteur posited that "spontaneous generation" and fermentation was actually caused by microorganisms. His work led Joseph Lister to develop and use antiseptic methods for his surgical tools in order to prevent infection. By the twentieth century, the microscope was used for the diagnosis of disease at a cellular level, where cervical cancer is an early example of diagnosis which has saved thousands of lives[4].

The microscope is based on the refraction of light. The light emitted by an object is bent to build a magnified image. The microscope is composed of an objective lens and an ocular lens (conventional compound microscope) which combined provides the means to observe a magnified image of the object (see figure 1.2).

There is a fundamental limit to the resolution of a microscope. This limit is given by the diffraction of light from a circular aperture. According to the Rayleigh criteria,(see

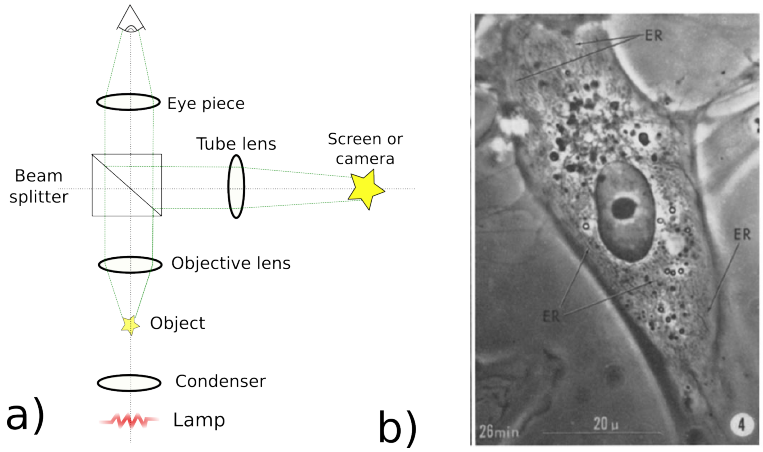

Figure 1.2: Basic diagram of a light microscope and an image of a cell. (a) Drawing of a conventional microscope. (b) Phase contrast image of a single cell (©*Rose et al,1960. Originally published in the Journal of Cell Biology. 8:423-430.*)[5].

section A.2) the lateral resolution of an optical microscope is given by:

$$x_{min} \cong 0.61 \frac{\lambda}{NA} \tag{1.1}$$

where λ is the optical wavelength and NA the numerical aperture (a measure of the acceptance angle of the objective). For the case of depth, the resolution is given by:

$$z_{min} \cong 2 \frac{\lambda}{NA^2} \tag{1.2}$$

Shorter wavelengths means greater resolution. Practically, objective lenses can have an NA up to ~ 1.4 (in oil). With an optical wavelength of 400nm, a microscope can reach a resolution of approximately 200nm and 400nm for the lateral and depth resolutions respectively. This means that microorganisms like viruses or large molecules can not be observed with an optical microscope.

1.3 Live cell imaging

Progress in microscopy and cell imaging has gone hand in hand with knowledge of microbiology and cell function. To understand life processes within a cell, it is important to observe a living organism. The optical microscope allows live cell imaging but also is practical to implement making it a very powerful tool which, at this time, remains the most relevant technology for the study of living cells[6].

Living biological cells are challenging subjects to study. Their requirements to remain functioning (temperature, media etc), the lack of optical contrast, their dimensions and complexity make cells difficult to image. For this reason, improvements of the basic compound arrangement used in the early microscopes were developed in the last century. For example, phase contrast microscopy[7] (see figure 1.2b) converts changes of phase at the sample plane, produced by the presence of material with different refractive indexes, into changes of intensity in the image plane to increase contrast. Interference microscopy[8] also converts relative changes in optical phase, experienced by light travelling through the sample, into changes in intensity. Confocal microscopy[9] uses a special arrangement where detected light comes only from a restricted volume reaching full diffraction-limited resolution at a cost of acquisition time (due to raster scanning). However, the resolution of the optical microscope remained unchanged.

In this section, the most used live-cell imaging tool (fluorescence microscopy[10]) and their related super-resolution branches[11], which overcome the limits of diffraction, will be discussed.

1.3.1 Fluorescence Microscopy

The discovery of the green fluorescent protein (GFP)[12], was a milestone in the capacity to probe the functions of a cell. The ability of such technology to target and image specific proteins or molecules through gene expression has given researchers the op-

portunity to test hypotheses and to understand cell function in depths never achieved before. These modern techniques often aim to break the barriers of diffraction-limited instrumentation, or simply to add a new way to observe different cell functions.

Fluorescence is the re-emission of light at a different wavelength by particular molecules when excited. When a photon is absorbed it excites an electron which spontaneously decays a short time after. The emitted photon (emission wavelength) has a different wavelength to that absorbed (excitation wavelength). In fluorescence microscopy this effect is used to image specific areas or molecules of a given cell. This is done by the use of stain or labels (such as GFP).

Stains are molecules that are attached to the cell in order to facilitate visualisation when imaging. A sample is exposed with the excitation wavelength and then the emitted light is captured by the use of optical filters. The image created by the fluorescence is then the distribution of the targeted protein or molecule within the cell (see figure 1.3b).

Its capacity to study dynamics of living cells and the protein and molecule pathways has provided insights into cell function, and made it possible to identify the internal components and processes of cells with a high degree of accuracy. However, the spatial resolution of a fluorescence microscope is still limited by diffraction and the use of the fluorescent proteins has raised concerns about their potential toxicity and the effect this might have on the health of the cells[13;14].

1.3.2 Super-resolution optical imaging

Radiation of short wavelength can achieve greater resolution than the optical microscope (see equation 1.1). Such imaging has revealed cell sub-structures of fixed (dead) specimens with great detail[15;16]. However, the function of those structures and their relation with the state of a given organism are difficult to understand if the specimen is no longer functioning.

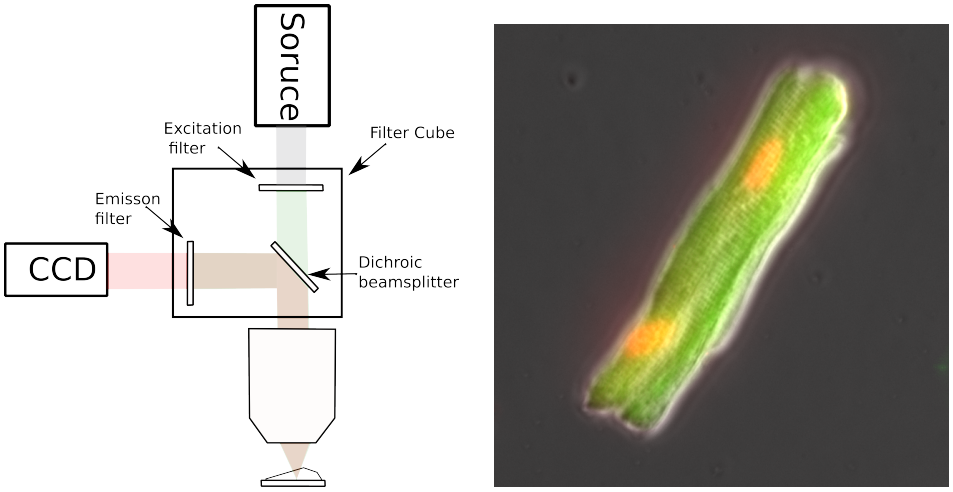

Figure 1.3: Fluorescence microscope. a) Simplified schematic of a fluorescence microscope setup; an excitation filter is used to block the fluorescence wavelength (or emission wavelength) from the light source to avoid background noise. The emission filter is used to block the excitation wavelength and observe pure fluorescence. The dichroic beams splitter allows excitation wavelength to be transmitted while reflecting the emission to avoid waste of light. The filter cube can be replaced to observe fluorescence from different dyes. b) Fluorescence diagram of a rat cardiac cell; the membrane is shown in green while the nucleus in orange.

For this reason, fluorescence microscopy, which allows live cell imaging, has faced a transition to super-resolution (resolution beyond the diffraction limit) in either x-y or z dimensions[11]. This kind of resolution can be achieved by non linear methods, for example, by limiting the emission of light to areas smaller than a diffraction spot or depth of focus. Super-resolution has been achieved through different techniques such as stimulated emission depletion (STED)[17], stochastic optical reconstruction (STORM)[18], among others.

Stimulated emission depletion microscopy

STED uses two lasers to overcome the diffraction limit (see figure 1.4). Two synchronised pulsed lasers excite and deplete the fluorescence. Since the depleting laser is focused into a ring, the central area of the excitation laser remains unaffected. The difference in area of the lasers illumination is a small area where the fluorescence is em-

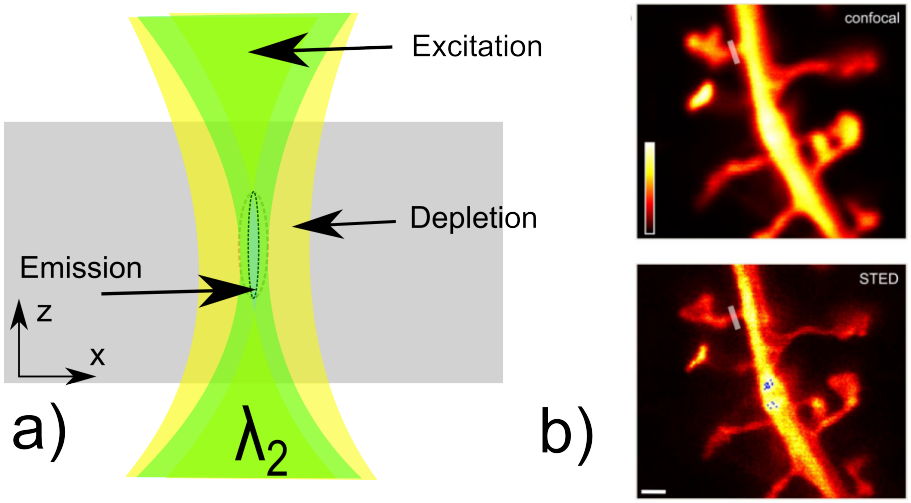

Figure 1.4: Example of STED microscopy. (a) STED microscopy principle. The volume where the light is emanated from is reduced by a depletion laser. (a) Comparison of the STED image of dendritic spines against confocal microscopy (*Nägerl et al*[19], Copyright (2008) National Academy of Sciences, U.S.A.) There is possible to see an increase in resolution.

anated from and is effectively smaller than the diffraction limit of the excitation laser. Using this technique, lateral resolution up to 30nm has been achieved and imaging on living cells has been performed[19;17]. The main disadvantage of this approach is the high flux of laser light (for each pixel) which induces high photo-bleaching (depletion of fluorescence) and potential damage to the specimen.

Stochastic optical reconstruction microscopy

STORM[18] takes advantage of the random switching of fluorophores to achieve super-resolution. Since fluorophores turn on and off at different times, a single fluorophore produces a diffraction limited spot, allowing an accurate spatial location of the source molecule. By taking a number of images for as many fluorophores as possible, their centroids can be identified and this information be used to produce an image with a resolution beyond the diffraction limit (see figure 1.5a). This technique has been demonstrated on living cells in two[20] and three[21] dimensions. However, this technique

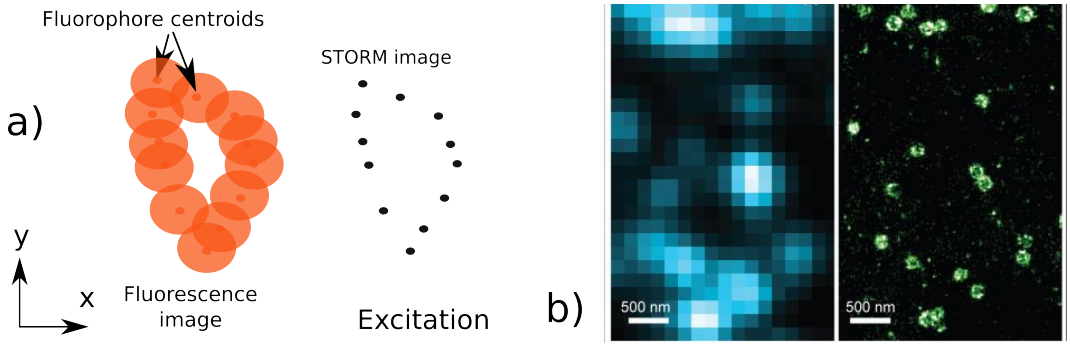

Figure 1.5: STORM microscopy example.(a) Diagram of STORM principle, fluorophores light up at different times giving the chance to render the the diffraction limited spot to a much smaller point. (b) Comparison of conventional (left) and super-resolution(STORM) images of the clathrin-coated pits in a BS-C-1 cell (*From Huang et al, 2008*[21]*. Reprinted with permission from AAAS.*). There is possible to see a very significant increase in resolution.

ideally require sparse distribution of the fluorophores to avoid errors in their location.

1.4 Mechanical methods applied to biological cells

As an alternative to optical imaging, mechanical imaging and characterisation is of great interest. The elastic properties of cells such as elasticity, speed of sound or strain and their relation with fundamental cell processes (like mitosis or migration) are largely unknown at sub-cellular level. For this reason, characterisation based on standard mechanical testing and imaging based on mechanical contrast have been reported. For instance, the forces required to detach[22] or deform a cell[23] have been measured using techniques like micro-pipette aspiration[24], atomic force microscope (AFM)[25], and optical trapping[26]. Cell imaging based on mechanical parameters has also been the topic of much research. Techniques like atomic force microscope, ultrasound[27] and Brillouin microscopy[28] have been studied to image and characterise cells. In this section, some of these techniques are reviewed.

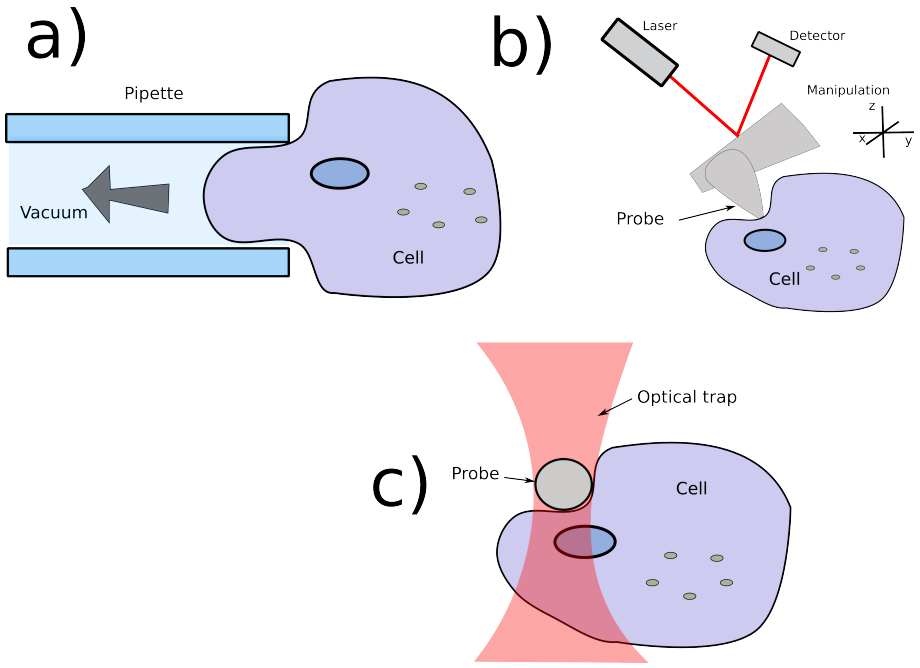

Figure 1.6: Mechanical characterisation of cells. (a) Micro-pipette aspiration. Highly invasive technique that probes over the whole cell. (b) AFM microscopy. Invasive technique which probes in smaller areas of the cell but it can only probe near the surface. (c) Optical trapping. Similar method to AFM but using a particle to sense the cell. Here there is also the use of intense lasers which could also be damaging to a cell.

1.4.1 Mechanical characterisation

Micro-pipette aspiration method

The micro-pipette aspiration method[24], aspirates a cell to a small glass tube (see figure 1.6a). The tube has a diameter of the order of a few micrometers. Changes in the cell's shape are tracked while the cell is aspirated. The suction pressure applied to the cell is carefully calibrated to estimate the viscoelastic properties of the cell[29]. The downside of this technique is that it is highly invasive (since the examined cell is sucked into a tube) and it can't resolve variations in the mechanical properties at the sub-cellular level.

Atomic force microscopy (AFM)

Nanoscale imaging is the main use of the AFM microscope, however it can also be used to probe the stiffness of surfaces. In an AFM microscope, a cantilever with a conical protuberance applies a force to the specimen. A laser is focused into the back of the cantilever and then detected by the knife edge method[30] (see figure 1.6b). As the tip is scanned, the cantilever moves up and down depending on the surface. The optical intensity detected is proportional to the cantilever deflection providing a measurement of topology or stiffness. Elasticity can be estimated by measuring the forces in all axes applied to the surface that causes deformations[23;22]. Using this method, it has been found that the elastic properties of cells at particular points were different between healthy and cancer cells[31]. The pressure applied by the AFM probe can be invasive to cells, causing changes to changes to morphology or function[32]. This contact method is difficult to be extended to imaging due to its invasiveness however is still possible to image living cells using an AFM as it will be described on section 1.4.2. Additionally, these kind of measurements are performed at the surface level meaning that sensitivity to mechanical properties below the surface is limited.

Optic trapping

Optical trapping consists of holding a particle or small object with a highly focused laser beam[33]. This is a non contact form of cell manipulation which also has force measurement capabilities[26] (see figure 1.6c). These capabilities can be used to measure membrane elasticity[34;35;36], topography[37], binding forces[38] and tool boxes have been developed to estimate those forces[39]. These techniques rely on high photon flux to produce forces large enough to manipulate cells or to move a particle (i.e. polystyrene bead) with a known force to sense the surface. The high energy flux is potentially harmful for biological cells, fine calibration is required to perform quantitative measurements and the penetration depth is limited to near the surface.

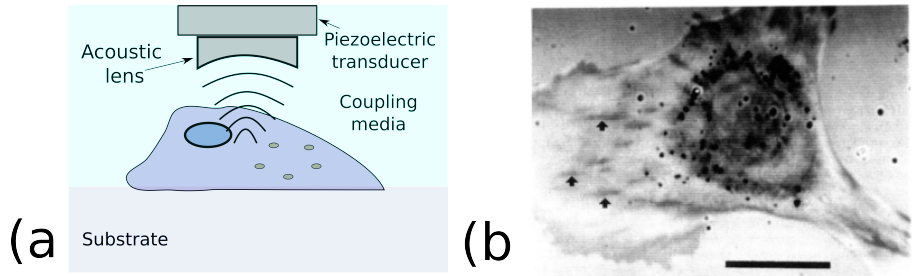

Figure 1.7: Acoustic microscopy on cultured cells (*Hildebrand et al,1981*[27]. Reprinted with permission from J. A. Hildebrand). (a) Schematic diagram of acoustic microscopy. (b) Example of image taken with acoustic microscopy from a chicken heart fibroblasts. This is a non-invasive technique which can probe mechanically across a cell with higher resolution than contact techniques. However its resolution is limited due to acoustic attenuation to 720nm at 1.7GHz.

1.4.2 Mechanical imaging of cells

Ultrasound

Ultrasound is a promising method for live-cell imaging. Given the much lower speed of sound compared with that of light, sub-optical acoustic wavelengths can be obtained at GHz frequencies. This provides a means for high resolution imaging without the harmfulness of, for instance, an electron beam.

Ultrasound is an indirect method for the imaging and characterisation of mechanical properties, for instance, the speed of sound depends on the elasticity and stiffness of the specimen. However it is less invasive than contact techniques. It can also make measurements in smaller volumes that can be near the surface or in-depth. Such characteristics give ultrasound a clear advantage over other methods of mechanical characterisation. Ultrasound has a long history in medical imaging[40] where it is routinely used for imaging of human internal organs and embryos. It also is widely used in industrial environments for non-destructive inspection of materials[41;42].

The scanning acoustic microscope (SAM) is the main tool for high-frequency ultrasound imaging. It focuses the generated ultrasound by an acoustic lens and then detects the scattered sound coming back (see figure 1.7). In its simplest form, the intensity of

the scattered sound is used to build an image by scanning point by point. However, if the intensity is resolved in time, echoes coming from different interfaces can be used to evaluate the speed of sound and thickness of features in particular samples.

The SAM has been used to image biological cells. With an aqueous coupling medium (cell media), imaging of living cells have been performed where the cells remained unaffected by the acoustic fields[27]. The acoustic microscope has also been used to measure the elastic properties of cells[43;44] by postprocessing the time-resolved data acquired by a SAM. The speed of sound inside a cell has been reported to be different to that of the media[45].

The acoustic microscope is a viable contact-less,wireless label-free tool to perform mechanical characterisation of living cells[43;44;45;27]. However, the piezoelectric transducers typically used to generate and detect ultrasound in a SAM work at a frequency that is limited by several factors which, when it comes to imaging, limit their resolution. Attenuation of sound at high frequencies, for example in water at 4.4GHz, is reported to be very large (1900dbm^{-1})[46], which limits propagation of sound below the focal length of the acoustic lenses. Similarly, electronics in the GHz range are also challenging to build and work with. For these reasons, imaging of cells based on the SAM then have a resolution that is not high enough to resolve most inner features of cells. Liquid helium has been used to reduce the acoustic attenuation in the low GHz region (15GHz). Here, the generated wavelengths are sub-optical[47;48]. However, the extremely low temperatures are clearly not suitable for live-cell imaging. At room temperature, the maximum frequency of a SAM on cell media is reduced to 1-2GHz which corresponds to longer wavelengths than that of light and hence poorer resolution.

Brillouin microscopy

Brillouin microscopy[49] provides indirect means to measure the speed of sound in order to image the mechanical properties of a given sample. It is based on the inelastic scat-

tering of light by high frequency vibrations spontaneously produced inside the specimen in a random way (also referred as phonons, see figure 1.8). When a photon is scattered by a phonon, it experiences a Doppler shift (upwards or downwards) that depends on the velocity of the phonon (speed of sound). If the photons are detected as a function of frequency, then the frequency shift (Brillouin frequency) can be measured. The shift can be seen downwards (Stokes) or upwards (anti-Stokes) with the same magnitude. The measured shift depends on the speed of sound and the refractive index of the materials (see equation 2.13).

Since a transparent material is needed to observe this effect, it is particularly suited for the observation of polymers[50;51], semiconductors[52], or biological tissue (Brillouin microscopy is an optical technique and as such, the resolution is limited by optical diffraction allowing higher resolution than a SAM). This technique has been applied to measure the speed of sound of muscle[53], bone[54] and eye[55] tissue. It also has been used to image eye in vivo[56], ex vivo biological cells[57], among others.

Cellular images reported by Palombo et al[57] show little inner cell detail, however they allowed the calculation of the sound velocity assuming the cell has a constant refractive index. The lack of inner detail is most likely to be related to a low resolution. This possibly comes from the low scattering efficiency where typically 10^{-12} to 10^{-10} photons are scattered[49]. Then, to improve resolution, high numerical aperture (NA) lenses are used. Such lenses capture light from a broad angular range; which reduces the accuracy of the frequency shift measurement (see equation 2.13) and also reduce the measured volume which decrements the amount of scattered photons.

Moreover, confocal arrangements have been used to improve axial resolution (which is particularly poor for low NA lenses) but this means that a large fraction of the light is lost (excluded by the pin-hole of confocal arrangement) making imaging a time consuming process (up to minutes per point). To overcome this, highly efficient spectrometers have been used, however the laser power required to achieve practical

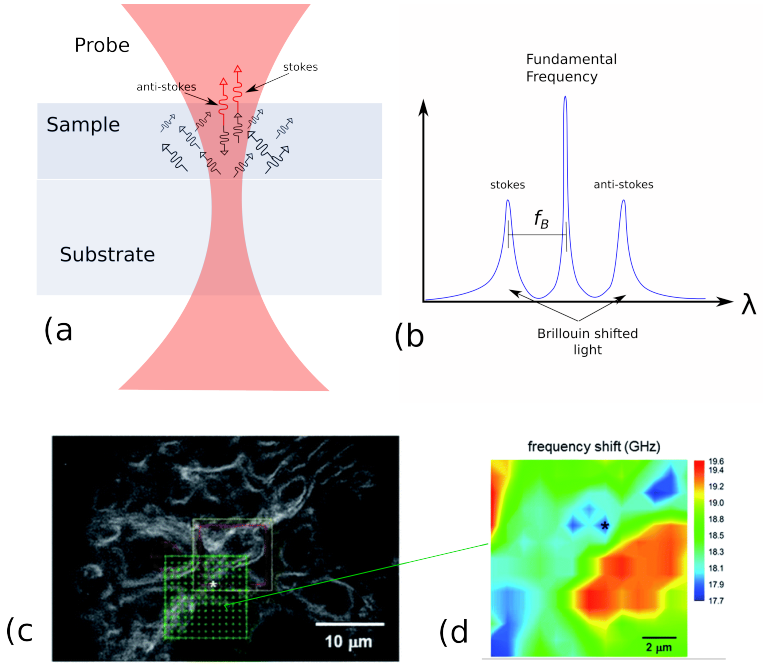

Figure 1.8: Spontaneous Brillouin scattering detection. (a) Schematic of scattering by random phonons where only photons scattered on the rigth direction (stokes or anti-stokes) and with the correct frequency can reach the detector. (b) Representation of a detected spectrum where the frequency shift between the fundamental frequency and the Brillouin peaks (stokes $+f_B$ and anti-stokes $-f_B$)is the Brillouin frequency. (c) Dark field image of cells in culture where the green area corresponds with the Brillouin image seen in (d)(*Palombo et al, 2014*[57]).

SNR and acquisition times are typically too high to be biocompatible when the probing spots become near diffraction-limited.

Atomic force microscopy

On an AFM, The tip of the probe has commonly a radius ranging from a few micrometres to a few nanometers giving resolutions even higher than some electron microscopes[58]. Given its high resolution, great effort went into image proteins and protein interactions[59;60;61]. In the case of imaging biological cells often the experiments suffered from cell damage and detachment when high resolution imaging was attempted. For these reasons methods to hold the cells have been implemented including adhesion proteins, fixing or holding by a micropipette. Using a fixing method, various types of cells were measured with high resolution by *Shao et al*[62] including kidney cells, fibroblasts, and cardiomyocytes among others. The invasiveness of the tip has also been reduced by vibrating operational mode[25]. In this mode the tip is made to vibrate and the effect of the near surface on this vibration is measured. This reduced damage and allowed the observation of living processes.

The increase of the acquisition speed provided by newer generation AFM microscopes have allowed to observe relatively fast events. However, the AFM is still constrained to the vicinities of the surface which is a limitation intended to be resolved by photonic force microscopy. Here the tip is replaced by a nanoparticle embedded in the specimen and trapped by laser beams. This new approach brings new challenges which may be solved in the future[58].

1.5 Picosecond Laser ultrasound

Given the interest in the study of cells, any new technique that can provide further information is of great interest. Imaging methods are more relevant if they are non-

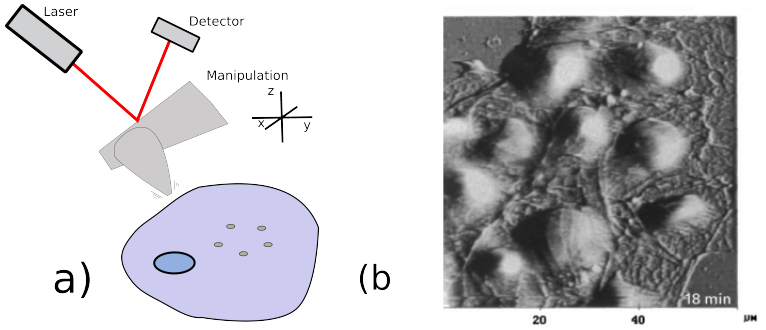

(a)

Figure 1.9: (a) Diagram of the vibration mode of an AFM. Image of a AV12 cell obtain using AFM (*You et al,2000*[32]). The inner structures of the cells are not revealed by AFM images due to the incapability of the method to measure beyond the surface.

invasive since they allow the study of cells while still functioning. A method based on picosecond laser ultrasound (PLU) and Brillouin scattering can overcome some of the limitations of both acoustic and Brillouin microscopy in what is normally called Brillouin oscillations[63] (see section 2.3). This all-optical method uses the pump-probe technique[64] to generate ultrasound and detect it via Brillouin scattering. By generating a coherent acoustic pulse, the scattering efficiency is increased significantly, typically by four to six orders of magnitude compared to Brillouin microscopy while overcoming the bandwidth limitations of the acoustic microscope. As Brillouin oscillations is a time-resolved technique, it can resolve in-depth changes with acoustic wavelength (typically sub-optical, see section 5.4.3). However, the use of transducers becomes necessary and the lateral resolution, at this time, is still limited by optical diffraction.

Brillouin oscillations have been demonstrated in vegetal cells by Rossignol *et al*[65]. In their work, different Brillouin frequencies(∼5-6GHz) were measured for the vacuole and nucleus of an onion cell, which suggests there is good acoustic contrast within the cell. This is a well suited method for cultured cells since the cells grow attached to a transducer (typically a titanium substrate). Additionally, the sound is detected as it travels through the sample reducing the effects of the high attenuation at these

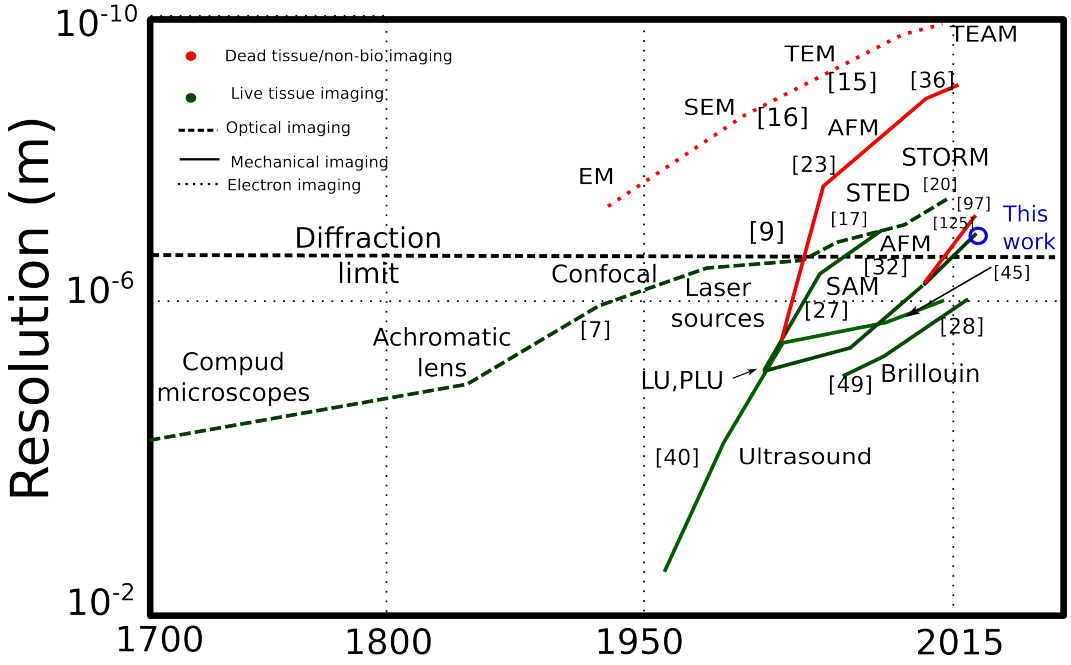

Figure 1.10: Arbitrary selection of imaging techniques and their resolution achieved in live cells or tissue. Red lines represent techniques not applicable to living tissue. The work presented in this thesis provides a step up in resolution on mechanical live-cell imaging compared to acoustic and Brillouin microscopy. The information presented in this graph is only an approximation.

frequencies. The viability of this technique for living cells in terms of laser exposure and temperature rise was analysed and concluded to be safe in principle[66]. However, this technique has not been applied yet to live cell imaging. Such images could provide new insights in cell research.

Figure 1.10 shows the resolution of some optical and mechanical imaging techniques. There, it can be seen that the resolution achieved by the PLU technique presented here is the highest resolution for mechanical live cell imaging except for the atomic force microscope. However the atomic force microscope is limited to the vicinities of the surface while Brillouin oscillation measurements can penetrate into the specimen. Also it shows that live-tissue imaging beyond the diffraction limit is remarkably limited and it was only in the last 10 years that the optical microscope went over this limit.

1.6 Aim of the thesis

The imaging of the Brillouin frequency of living or cultured cells based on picosecond laser ultrasound had not been performed before. The importance of mechanical cell imaging and characterisation and the potential of Brillouin oscillations for three dimensional sub-optical non-destructive cell-imaging, has inspired this work.

The aim of this thesis is about the development of a high resolution ultrasound technique for live-cell imaging. Here the goal is to design and apply multilayer thin-film opto-acoustic transducers that allows the imaging of live biological cells. The transducers and measuring system should address the challenges that prevented the production of images with Brillouin oscillations: cell damage, signal amplitude and acquisition speed. To achieve this, the transducers and measuring system are implemented in such a way that it improves scattering efficiency (signal amplitude) while protecting the cell from laser radiation. The acquisition speed is to be improved by the use of a pump-probe technique without moving parts[67]. All these improvement have enabled to perform imaging relating to the mechanical properties of living cells with sub-optical wavelengths. Such imaging would be of great interest of cell-research community and might provide new insights on cell biology.

1.7 Thesis structure

With a brief introduction to the problem and motivation of this research, the rest of this thesis is organised as follows. Chapter 2 presents a detailed background of the problem aimed to be solved in this thesis as well as more discussion of the proposed solution and objectives. Chapter 3 presents detailed modelling of the proposed opto-acoustic transducers and a optimal design is discussed. Chapter 4 presents the methods applied for the preparation and measurement of specimens and samples. In chapter 5, the results of the measurements are presented where the models are validated and

Brillouin oscillations images (2D or 3D) of phantom, fixed and living cells are shown. In chapter 6, future developments of these transducers are presented as well as future improvements of the measurement procedures. Finally the conclusions from this work are discussed in Chapter 7.

Chapter 2

Background

2.1 Introduction

Picosecond laser ultrasound (PLU) is an intriguing path for the high resolution imaging of the mechanical properties of living cells. The mechanical nature of the acoustic waves provides an alternative mechanism for contrast and it is less invasive than their electromagnetic counterparts. For instance, it is unlikely for sub-optical wavelength ultrasound to break molecular bonds within a cell, as is possible by short electromagnetic waves. This is due to the nature of light and sound, the energy contained in photons and phonons:

$$E_{photon} = \hbar f_{photon} \tag{2.1}$$

and

$$E_{phonon} = \hbar f_{phonon} \tag{2.2}$$

where f_{photon} and f_{phonon} are the frequencies of photons and phonons respectively and $\hbar$ is the Planck constant. Compared to phonons, photons of the same wavelength carry significantly more energy (5-6 orders of magnitude) than can interact directly with

electrons. This interaction can break atomic/molecular bonds which can disrupt cell function.

By the use of Brillouin oscillations, acoustic wavelengths of the order of 300 nm can be probed by 780nm light which can be used to resolve features in-depth with higher resolution than the optical microscope. Moreover, the Brillouin frequency depends only on the speed of sound, the probing wavelength and refractive index, making it a powerful tool for optical and mechanical characterisation. In addition, a single Brillouin oscillation measurement can lead to the measurement of a large volume, which can be then sectioned by signal processing potentially providing 3D imaging.

In this chapter, some of the most relevant mechanisms for the generation and detection of ultrasound using short light pulses is discussed. Then the latest advances on PLU methods to characterise and image cells are discussed highlighting their achievements and limitations. Finally, a detailed discussion of the objectives of this thesis are presented.

2.2 Laser ultrasound

Laser ultrasound (LU) is a technique to generate and detect ultrasound by using light. LU is an alternative to piezoelectric transducers with clear advantages; couplant-less, wire-less operation and broader generation bandwidth. It relies on the temperature rise produced by the absorption of a focused short light pulse on an opaque material to generate an acoustic wave. The width of the optical pulse can be as short as few femtoseconds leading to the generation of ultrasound in the THz range[68]. There are a number of detection methods ranging from opto-elastic effect[64], knife-edge[30;69], interferometry[70] and transducers[71]. However, those methods still need an electronic acquisition system which is difficult to implement in the GHz range due to the high attenuation of electronic signals in this regime. Ultra-fast photodiodes in the tens of

GHz are commercially available but they tend to be difficult to use in laser ultrasound because the light sound interactions in the GHz range tends to be weak.

The pump and probe technique is used to detect acoustic waves in the GHz range and above and this method does not require the use of fast electronics[72]. Here another time-delayed short laser pulse is used for the detection of the fast events (see section 4.3). Laser ultrasound based on the pump-probe technique is commonly referred as picosecond laser ultrasound (PLU), where the detected signals are typically in the picosecond time scale. These high frequencies easily overcome the bandwidth limitations of the SAM. It also has helped to improve the efficiency of Brillouin scattering measurements (Brillouin oscillations). All these advantages make picosecond laser ultrasound a potential alternative for mechanical imaging of living cells. In this section, the mechanisms of generation and detection of ultrasound by laser light pulses will be discussed. Additionally, some of the laser ultrasound techniques and methods will be reviewed within the context of this work.

2.2.1 Laser ultrasound generation

The optical generation of ultrasound is produced by the absorption of light in opaque materials (mainly metals). The absorption of a focused short pulse of light produces heat which causes the material to expand rapidly generating stress that launches a strain pulse (see figure 2.1). Exposing a high energy laser beam to an absorbing sample can lead to additional effects apart from temperature rise like radiation pressure or ablation. However, we work in a lower energy regime where temperature rise is the only observed effect.

Generating ultrasound by short light pulses help to keep average powers low while peak powers are high enough to produce sound pulses. The shorter the pulse the more energy is concentrated in high frequencies.

To generate high frequency ultrasonic pulses, very fast optical pulses are required,

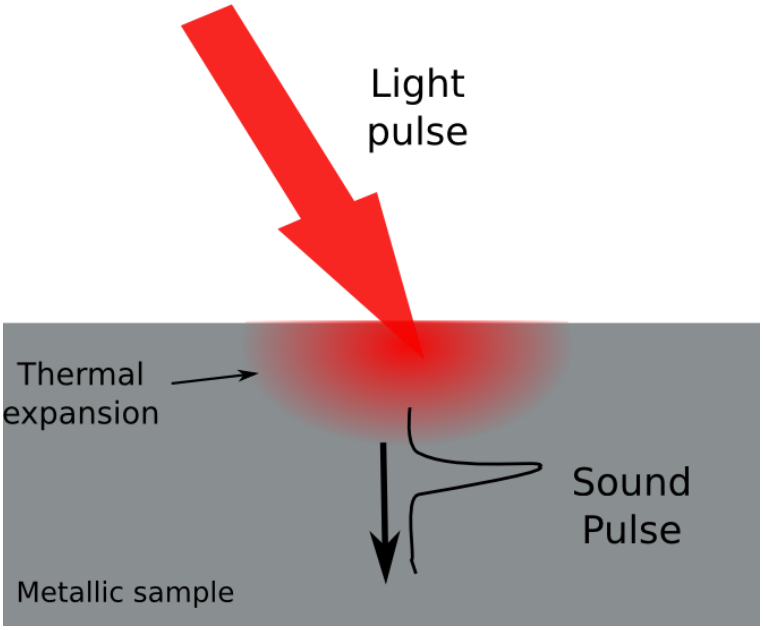

Figure 2.1: Thermoelastic generation of acoustic waves. Short laser light pulse is absorbed in a sample causing rise in temperature which launches acoustic waves due rapid change in local pressure induced by thermal expansion.

for example to generate a 10GHz a 1.8 pico-second pulse would be required. The energy contained in each pulse is difficult to measure directly. However the total energy of a pulse ϵ_p can be evaluated based on the average power:

$$\epsilon_p = \frac{P_{avg}}{f_p}$$

where f_p is the repetition rate (number of pulses per second) and P_{avg} the average power. The peak power can be also calculated with the following relation:

$$P_{peak} = \frac{\epsilon_p}{\tau}$$

where σ is the duration of the pulse. Another useful measure is the energy density

defined as the energy radiated over an area:

$$\mu_p = \frac{P}{\mathfrak{a}}$$

where P can be either the average or peak power and $\mathfrak{a}$ is the irradiated area which for a laser spot, with a radius r, becomes $\mathfrak{a} = \pi r^2$. For example, a pulsed laser beam with repetition rate of 100MHz, pulse duration of 150fs and average power of 1mW will produce pulses with a energy of 10pJ, a peak power of ∼66.6W.

Consider the experiment presented in figure 2.1 where a short light pulse (∼150fs) is incident on the surface of a metallic film. The skin depth (δ_p, see section A.3) is smaller than the illuminated area $\mathfrak{a}$ on the film as well as its thickness. Then, the total energy absorbed by the film ϵ_T in a volume becomes:

$$\epsilon_T(z) = \frac{(1-R)\epsilon_p e^{-z/\delta_p}}{\mathfrak{a}\delta_p}$$

where R is the optical reflectivity (see section 3.2). This absorption of energy produces a temperature rise $\Delta T(z)$ given by:

$$\Delta T(z) = \frac{\epsilon_T}{C}$$

where C is the heat capacity. Since the material is assumed isotropic and the only displacement considered is in the z direction, then the elastic wave equation that describes the strain propagation becomes:

$$\frac{\delta \sigma_z}{\delta z} = \rho_0 \frac{\delta^2 \mu_z}{\delta t^2} \tag{2.3}$$

where σ_z is the longitudinal stress (applied force), ρ_0 the material density and μ_z the

displacement in z. From there, the longitudinal stress is given by:

$$\sigma_z = \rho_0 \nu^2 \eta_z - 3B\beta\Delta T(z) \tag{2.4}$$

where ν is the sound velocity, β the thermal expansion coefficient, B the bulk modulus and the strain η_z (deformation upon stress) is given by:

$$\eta_z = \frac{\delta\mu_z}{\delta_z} \tag{2.5}$$

For an initial condition of z=0, t=0, $\sigma_z = 0$, the initial temperature rise becomes[73;74];

$$\Delta T_0 = \frac{(1-R)\epsilon_p}{\mathfrak{a}\delta_p C}$$

and the initial strain is given by:

$$\eta_0 = \frac{3B\beta\Delta T_0}{\rho_0 \nu^2}$$

Solving these equations, the solution for the strain becomes:

$$\eta(z,t) = \eta_0 e^{-z/\delta_p} - \frac{\eta_0}{2}[e^{-(z+\nu t)/\delta_p} + e^{|z-\nu t|/\delta_p} sgn(z-\nu t))] \tag{2.6}$$

These calculations[73;74] allow the evaluation of the strain distribution and temperature rise caused by a laser pulse in a material that is thick enough enough so the whole of the light is absorbed and the generated sound propagates in the material until is fully attenuated. For instance. Figure 2.2 shows a simulation of the strain generated by a sound pulse derived from equation 2.6 for a titanium film. There it is possible to see the spatial distribution of the strain along the z axis for three different instances of time.

For more complicated cases, where some of the conditions shown above are different

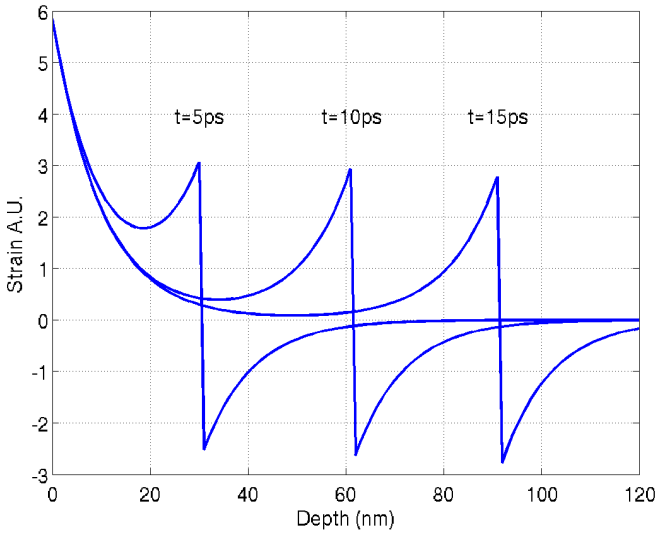

Figure 2.2: Simulation of the strain distribution across a the z axis in a titanium film. The strain is caused by a light pulse at three different moments in time.

(more than one layer and more than one heat source), these models become increasingly difficult to solve. For example, a multilayer structure is modelled in *Matsuda et al*[75]. There, the thickness of the layers are in the nm to μm range which means that some assumptions are no longer correct and while the formulation for multiple thin layers can be solved, the process is complex. However, to obtain a quantitative solution of such models, it is required the knowledge of a number of parameters which not always are known.

Opto-acoustic transducers for laser ultrasound generation

Ultrasound generation by laser is typically limited to metals which generate waves with particular characteristics. However, there are cases where, for example, strengthening of surface waves might be more adequate, or the case where the specimen exhibits very small optical absorption. In such cases an opto-acoustic transducer is used to generate the ultrasound with the desired characteristics. For example, patterned transducers are used to generate surface waves[71], metallic thin films to examine translucent di-

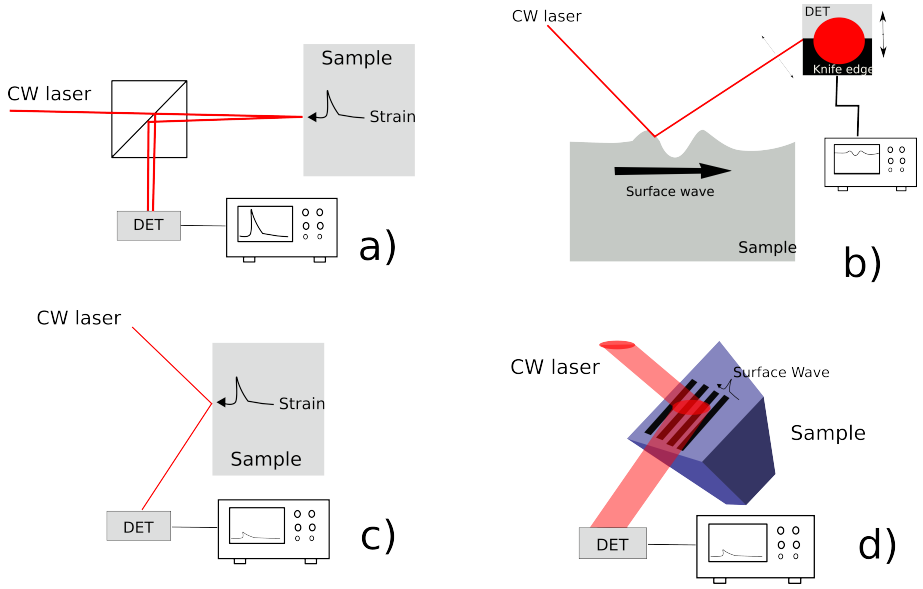

Figure 2.3: Simplified schematic of ultrasound detection. (a) Example of interferometry arrangement [78]. (b) Knife edge detection of a surface wave. (c) Simple detection of a strain based on opto-elastic effect [64]. (d) Detection of a surface wave based on a patterned transducer [71]

electric [63] or semiconductors [76]. A simple titanium thin film has been used to radiate GHz frequency into biological cells [77] where despite the lack of optical absorption of the cells, measurements were performed successfully. However, these methods have the disadvantage that they need to be in contact with the sample coupling not only sound but heat as well.

2.2.2 Laser ultrasound detection

There are a number of different detection methods applicable to laser ultrasound, these are based on interferometry, the opto-elastic effect, beam deflection or a combination of any of these. The interaction between sound and light provides a way to detect ultrasound while overcoming some of the limitations of piezo-electric transducers such as the need for couplant, limited bandwidth, and fabrication in the micro-scale. In this section we will review some of the continuous and pulsed laser detection methods commonly used in LU and PLU experiments.

Opto-elastic effect

The opto-elastic effect is the modulation of the refractive index due to the change in pressure associated with acoustic waves. This effect has been exploited to deflect, modulate or to frequency-shift optical beams. Those effects produce change in phase or amplitude of an optical beam that can be detected in different ways. Each material exhibits a different rate of change of the refractive index with respect to the strain (opto-elastic coefficient, $\delta n/\delta \eta$). The variation of refractive index induced by a given strain is then given by:

$$\delta n(z,t) = \frac{\delta n}{\delta \eta}\eta(z,t). \tag{2.7}$$

To produce a quantitative model of change in refractive index produced by a give strain, it is necessary to know the opto-elastic coefficient which has not been reported for the materials used in this thesis (gold and indium tin oxide). One of the simplest ways to detect an acoustic wave via the opto-elastic effect is by monitoring the reflectivity on the surface of a material (commonly metal[64], see figure 2.3c). The reflectivity of a metal-air boundary is dictated by the refractive indexes of the materials and the incident angle of the light beam as represented by the Fresnel coefficients (see section 3.2). When an acoustic wave reaches the surface, the refractive index of the metal is modulated by the strain affecting the reflectivity of the interface and providing a method to measure the wave. The sensitivity of this method is commonly low meaning that high-intensity beams are needed in order to achieve usable signal-to-noise ratio. Despite this, this is a widely used detection method in PLU due to its simplicity.

It is also important to mention that the refractive index is not only modulated by the strain but also by the temperature change as:

$$\delta n(z,t) = \frac{\delta n}{\delta T}\Delta T(z,t) \tag{2.8}$$

where $\delta n/\delta T$ is the thermo-optic coefficient. The effect of the temperature on the intensity of the reflected signals is normally referred as the thermal background. This change in intensity is slow compared to the period of our signals (see section 3.4.1) which can be easily removed by signal processing (see section 4.5.1).

Interferometry

Interferometry is a common method of detection of ultrasound. This is achieved by interacting an object beam in such way that its phase is modulated by an acoustic field. The modulation can be induced in several ways. One way to achieve this is to expose a surface where the ultrasound is arriving. (see figure 2.3a). From equation 2.6 it is possible then to calculate the displacement induced by a strain as:

$$\mu_z(z,t) = \int_0^{\inf} \eta(z,t)\delta z \tag{2.9}$$

and this displacement, at normal incidence will change the phase of the optical beam:

$$\delta\phi = \frac{4\pi}{\lambda}\mu_z$$

providing means to quantify the response expected from a given strain. If the relative phase of the modulated beam is out of phase with the reference by π, then the variations in phase are converted to variations in amplitude in a linear way providing means to measure the waves. This method provides typically higher modulation depths compared to simple monitoring of the reflected intensity at an interface because the intensity change produced by interference is larger compared to that produced by refractive index modulation. Detection of ultrasound by interference though has several variations related to stabilising the measurements and the modes of separation and recombination of the beams. For example, two wave mixing in fibres[79] or free space[80] or Fabry-Perot interferometers[81] are common interferometric configurations.

Beam deflection/distortion

Deflection or distortion detectors use the effects on the beam shape and position induced by an acoustic wave (commonly surface waves) for its detection. For instance, the knife edge detector rely on the change in the reflected beam induced by a wave bouncing (longitudinal) or propagating (surface) on the surface of a specimen. The position of a spot reflected off the surface where the sound is propagating changes according to the acoustic field producing an illumination that moves in similar way (see figure 2.3). If half of the detector is blocked (by a knife edge), the intensity detected will change according to the surface displacement. This method is commonly used to detect surface waves because of its simplicity. However this methods needs polished surfaces which are not always available. Refinements of this method include split detectors in differential configuration and speckle capable CCD. For instance, a split detector is used instead a knife edge to increase modulation depth by subtracting the output of the both detectors (each one equally illuminated when there is no ultrasound). Speckle capable detectors are based on smart CCD detectors which convert each speckle into its own split detector[69]. In this way, the deflection still can be used to detect ultrasound from a rough surface.

Similar to the knife edge detector, in the beam distortion detection method[82] the probe reaching to the detector is partially blocked. But instead of a knife edge, this time by an iris. The iris allow maximum light transmission while also intensity modulation specially for large NA lenses where the distortion of the beam produces a significant intensity modulation.

Opto-acoustic transducers for laser ultrasound detection

As mentioned earlier, generation transducers are used in special situations where there is not enough absorption, or when the generated soundwave requires certain characteristics on propagation modes or bandwidth. Transducers can also be used for the

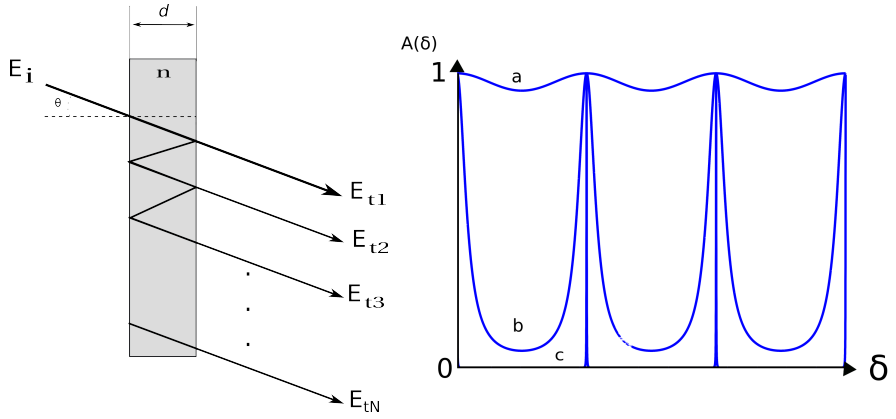

(a) (b)

Figure 2.4: Multiple beams interference on an optical cavity. a) Schematic of a simple cavity and the paths followed by the beams. b) Transmission of a cavity for different finesse factors 0.5, 4 and 324 for curves a b and c respectively. The finesse of the cavity (sharpness of the peaks) depends on the reflectivity of the layers, losses within the cavity and coherence length of the light source.

enhancement of the detection of ultrasound.

One method of detection based on a detection transducer, relevant to this work, is via optical cavity transducers. There, the interference of multiple waves inside of parallel partially reflecting layers is used to produce an interference pattern with periodic dips (reflection) and peaks (transmission). For example, a dielectric film will serve as an optical cavity because light reflected/transmitted at the film interfaces bounces back and recombines in a sort of optical feedback system. The resultant interference will then be composed of a number of waves (see figure 2.4), with a phase shift given by the cavity characteristics, the beam coherence length and the wavelength.

By solving the multiple interference between parallel layers, it is possible to derive the transmittance and reflectivity of the cavity[83;84]:

$$I_t = A(\delta) = \frac{1}{1 + Fsin^2(\delta/2)} \tag{2.10}$$

and

$$I_r = Fsin^2(\delta/2)A(\delta) \tag{2.11}$$

where $A(\delta)$ is known as the Airy function, $\delta = k_0 n 2dcos\theta$ the phase contribution due to the optical path difference that depends on the film characteristics (thickness d and refractive index n), and the propagation constant k. The factor F is defined as the finesse of the cavity and it is a measure of the width of the resonance peaks and is given by:

$$F = 4r^2/(1-r)^2 \tag{2.12}$$

where r is the reflectivity of the interfaces. The transmittance of cavity given by equation 2.10 is shown in figure 2.4b. As the reflectivity r of the interfaces increases, the finesse coefficient increases and the transmission peaks become narrower. This narrowing effect is very useful. For instance, if the wavelength is selected to be on the slope of one of the peaks, then the intensity of the reflected or transmitted beams will be very sensitive to the cavity size. If the cavity size is comparable in size to an acoustic wave, its size will be modulated by the displacement induced by the wave travelling through it producing a mechanism for light modulation. By detecting in this way, there is the possibility to increase the sensitivity to the acoustic waves by the interference produced inside the cavity (see section 3.1.1).

This kind of detection has effectively been used to increase sensitivity to MHz waves ultrasound to produce three dimensional images of tissue[85;86] and transducers in the GHz range have also been demonstrated[87;88]. The disadvantage of this method is that the transducers need to be attached to the specimen. However, this is necessary for transparent specimens in most LU situations.

There are also grating transducers, which take advantage of diffraction of light from

periodic structures to enhance the detection of surface waves[71]. Here, the height of the grating is adjusted to induce interference within the grating converting the change in grating size(induced by a surface wave) into change of intensity.

Pump and probe technique; picosecond ultrasound

The pump and probe technique is used to overcome the limitations of detection at high frequencies related to continuous lasers and electronics in picosecond laser ultrasound. It uses a pulsed laser not only to generate but also to detect the ultrasound. This is done by separating the pulses in pump and probe parts. The pump is used to generate the ultrasound while the probe laser is used to measure it. The probe beam is delayed in a controlled way (normally by a mechanical delay line[73]) to sample the event in time by sequentially repeating the event and adjusting the delay. Finally the trace of an event is built from the measurements of every delay position. This approach does not require high speed photodiodes or detectors (see section 4.3.)

Based on this technique, acoustic measurements in the GHz range have been performed on metals[64;89], semiconductors[90] and many other materials. The scale of these measurements is relevant to the characterisation of small objects such as thin films[89], particles[91;92], fibres[93] or biological cells[65]. Further details of this method are discussed in section 4.3.

2.3 Time-resolved Brillouin scattering

Brillouin oscillations measurements are a promising way of taking cell mechanical imaging forward because it can overcome the main limitations of Brillouin and acoustic microscopy. In this section, Brillouin scattering and Brillouin oscillations will be discussed in detail as well as their application to the characterisation of cells.

As mentioned previously, Brillouin scattering occurs when sound is scattered from

a acoustic wave in a translucent solid or liquid media. The scattered light beam experiences a frequency shift because the scattering element is moving. This shift, the Brillouin shift, can be measured in two ways; spectrometry (see section 1.4.2) or time resolved PLU measurements. In the latter, the scattered light interferes with a reference beam. The intensity modulation resulting from this interference (commonly known as Brillouin oscillations) is resolved in time. There is a clear distinction between the two methods where, to avoid confusion, the spectrometric conventional approach will be referred as Brillouin microscopy and the PLU approach as Brillouin oscillations.

From a classical point of view, an acoustic wave generates a grating due to the opto-elastic effect in the strain regions (crest of the waves, see equation 2.7). An incident optical wave will be then partially reflected according to the Fresnel coefficients (see section 3.2) if it satisfies the Bragg condition:

$$\lambda_B = 2n\Lambda cos\theta$$

where n is the refractive index of the media, Λ the period of the grating and θ the incident angle (see fig 2.5). A wavelength satisfying the condition will be delayed by a full wavelength for every round trip of the grating period Λ making all the beams scattered from each section of the grating to be in phase and therefore interfere constructively.

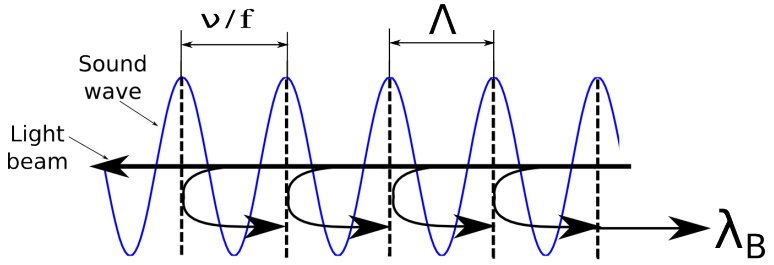

Figure 2.5: Bragg grating made out of a soundwave. The acoustic maximum serves as the scattering element due to the opto-elastic effect. The period grating depends on the acoustic source (frequency) and material (speed of sound). The incident light ($\theta = 0$) that satisfies the Bragg condition it is reflected by the grating.

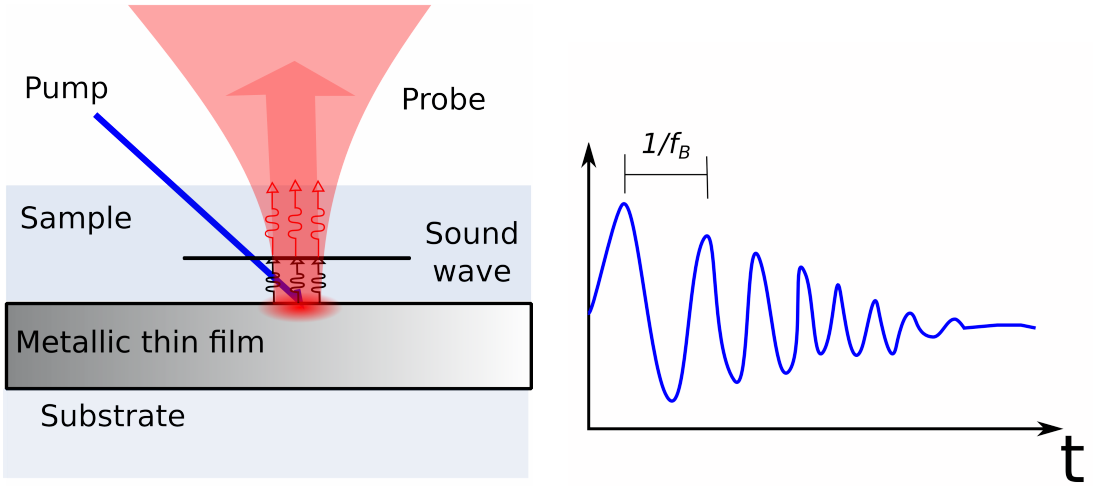

(a) (b)

Figure 2.6: Schematic of Brillouin scattering detection using PLU. (a) Schematic of detection. The pump beam of a pump and probe system generates an acoustic wave. The probe beam is scattered by the acoustic wave efficiently. The beam reflected from the metallic thin film serves as a reference beam which allows the observations of Brillouin oscillations on a detector. (b) Representation of Brillouin oscillations signal without thermal background. The amplitude decays quickly, however the temporal axis can be converted to spatial axis to allow sectioning.

Since the period Λ is given by a sound wave it can be written in terms of the speed of sound ν and the acoustic frequency f as $\Lambda = \nu/f$, rewriting equation 2.13 as:

$$\lambda_B = \frac{2n\nu}{f} cos\theta$$

.

Then the frequency of an acoustic wave necessary to scatter a light with wavelength λ in a translucent material is given by:

$$f_B = \frac{2n\nu}{\lambda} cos\theta \tag{2.13}$$

where n and ν are the refractive index and speed of sound of the sample material, θ

the optical incident angle and λ the optical wavelength.

Since the speed of light is greater than the speed of sound, the propagation of light can be considered instantaneous. It takes then to the soundwave (grating) one temporal period $T_a = 1/f$ to move one spatial period Λ (see figure 2.5). Thus, the phase of the optical wavelength, which satisfies the Bragg condition, is modulated at the rate of the acoustic frequency. If the scattered wave is then made to interfere with a reference beam, Brillouin oscillations are observed and the frequency of this modulation is the Brillouin frequency f_B. Brillouin frequencies are typically in the GHz range depending on the material properties and wavelength. For example, the frequencies of water and glass are approximately $\sim$5 and 22Ghz respectively (at λ=780nm).

The scattering efficiency (the ratio between input and scattered photons) in Brillouin microscopy is very low ($\sim 10^{-9}$-10^{-12}) because only a few of the spontaneously generated vibrations have the direction and frequency appropriate to scatter a particular probing wavelength into the detector (see figure 1.8). This means large average power and long integration times must be used. If, instead of relying on spontaneously generated vibrations, a coherent acoustic field with the right direction and frequency is generated, then the amount of scattered light will be increased. This is achieved by the use of PLU and the pump-probe configuration. The pump pulse incident into a metal film creates a strain pulse which propagates perpendicularly to the plane of the metal layer and parallel to the optical axis. When the probe pulse arrives, part of it is scattered from the coherent acoustic field. The rest of the beam is reflected in the transducer and interferes with the scattered light to observe Brillouin oscillations (see figure 2.6).

This method can lead to a direct measurement of the speed of sound in translucent samples if the refractive index of the material is known. Similarly, the elastic modulus can be measured if the density is also known. This represents a major potential for quantitative measurements if the Brillouin frequency and speed of sound/refrac-

tive index are measured simultaneously. Using this technique, measurements in polymer shells[92], dielectrics[77], semiconductors[76] or biological cells[65] have been performed. However no imaging on two or three dimensions of the Brillouin frequency have been reported to date on live biological cells.

In this form of Brillouin scattering detection, the Brillouin frequency can be resolved in time. If the refractive index of the media is known, the speed of sound can be calculated using equation 2.13. In doing so, the temporal axis can be converted to a spatial axis(z) which allows the measurement of the Brillouin components spatially. This method can measure signal for a long pathlength (several acoustic wavelengths) to then segment into sections as small as half acoustic wavelength ($\sim$150nm in water at λ=780nm). The accuracy of such measrements may be low given that the measurement of the Brillouin frequency is based on half a single cycle. This is a promising way of three dimensional high-resolution mechanical imaging. However, its lateral resolution is diffraction-limited and decreases as the sound travels deeper in z by; the spread of the optical spot as the sound travels away from the transducer, and the rapid attenuation of the signal which reduces spectral resolution (capacity to resolve small changes in the Brillouin frequency).

2.4 Laser ultrasound in biological cells

Acoustics in the GHz regime has inspired much interest as a tool for imaging and characterisation of cultured cells. This particular application, which is directly related to this work, will be reviewed in this section.

2.4.1 Brillouin oscillations

Most PLU measurements on cells are based on Brillouin oscillations because of their capability of directly measuring the speed of sound if the refractive index is known (or

vice versa). This feature has been used as a basis to calculate the mechanical properties of the cells. Brillouin scattering PLU experiments are based around an opto-acoustic transducer commonly composed of a single metal thin-film that allows the thermoelastic generation of ultrasound. Such a configuration is suitable for cultured cells that can grow directly on top of transducers, avoiding the need for any kind of couplant. This kind of detection reduces the effect of acoustic attenuation, since the generated strain is monitored as it travels through the sample giving the opportunity to probe high frequency ultrasound.

Figure 2.6 shows a diagram of PLU detection of Brillouin oscillations. A pump laser, applied from above or below, is used to generate ultrasound. The probe pulse comes at a delay to probe the sound (typically 0-10ns). Part of the probe beam is scattered back to the detector. The remaining beam is reflected by the transducer and interferes with the scattered light to produce Brillouin oscillations.

Measurements of the Brillouin oscillations on vegetal cells were reported recently [65]. There, onion cells were placed on a titanium thin film to detect Brillouin oscillations similar to as shown in figure 2.6. The article concluded that a different Brillouin frequency was observed from the nucleus and the cytoplasm of the cells (see figure 1.1) indicating good contrast of the Brillouin frequency at sub-cellular level. Later, theoretical models were developed to match the experimental results and the viability of these experiments discussed predicting good biocompatibility [66].

In a conventional Brillouin detection arrangement, both pump and probe lasers enter the cell, causing photo-damage and preventing extended measurement periods. To avoid that, an alternative method of generation was implemented by pumping the acoustic wave from below through a glass or sapphire substrate that serves as a heatsink [94] (see fig 2.7). This configuration is useful to reduce the damage suffered by the cell due to the absorption of pump beam and the heat generated by it. However, there is a significant reduction of signal amplitude, probably because the difficulty of

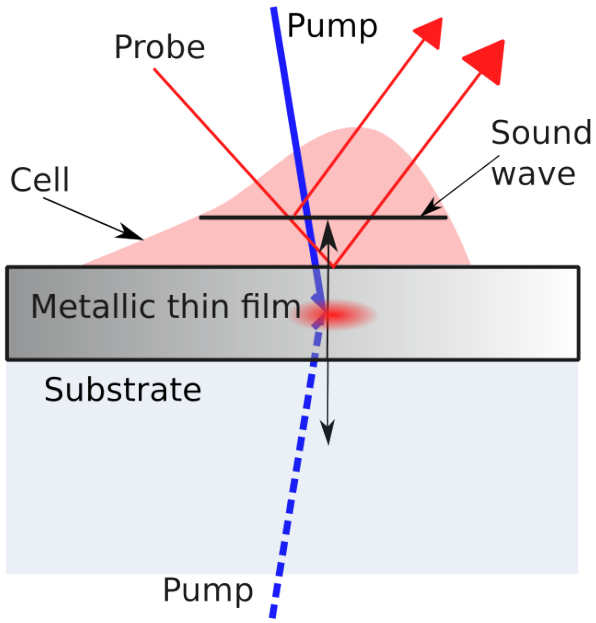

Figure 2.7: Schematic of Brillouin scattering detection. The pump beam generates an acoustic wave without stressing the cell. The beam is absorbed by the metallic film while the substrate acts like a heatsink. The probe beam is scattered by the acoustic wave via opto-elastic effect. The beam reflected from the metallic thin film serves as a reference beam which allow the observations of Brillouin oscillations on a detector.

aligning and stabilising opposite-facing high numerical aperture objectives. Nevertheless, in the same work parallel measurements of the echoes inside the thin film allowed to estimate the reflectivity of the titanium-cell interface. This measurement was used to aid fitting of the density and stiffness of the examined cells[94].

Based on a similar configuration, the mechanical properties (elastic modulus and viscosity) of the nucleus from fixed bone cells was reported[95]. Those estimations were obtained with the aid of model fitting and parallel (same measurement) detection of surface motion based on interferometry. Additionally, single point measurements were expanded into line scans, where the thickness of the cell was estimated. In the same work, the increase of resolution by the use of a shorter wavelength probe beam was also demonstrated.

The same technique was used to make a study of vegetal cell wall concluding based on modulus measurement that the structure of the wall resembles a composite material[96]. This is a remarkable result which shows great potential for cell imaging and characterisation. The aid of optical and mechanical models is necessary because of the indirect nature of the measurements. Since the Brillouin frequency depends directly on the refractive index and the speed of sound (see equation 2.13), it is not possible to calculate the speed of sound without knowing the refractive index, which is unknown at the scale probed. This means that parameters like the refractive index, speed of sound or density need to be fitted to a theoretical model to explain the experimental results.

2.4.2 Other PLU methods

PLU methods have been used to sense[97] and image[88] protein binding. There, the transducer is an acoustic resonators comprised of by more than one layer. The multiple layers allow detection of the resonance by interference. The resonance narrows the bandwidth making this a single acoustic wavelength technique. By observing the changes in the resonance frequency and amplitude of the transducer the presence of mass can be detected.

Biological cells have also been tested[98] with similar techniques and their adhesion tested by measuring the acoustic reflectivity of the cell/substrate interface. When a broadband acoustic pulse arrives at the cell/transducer interface, part of it is reflected and part transmitted according to the impedance and contact of the cell.

Figure 2.8 shows a diagram of this configuration. Both detection and generation of ultrasound by lasers is through the substrate into the metallic film. The film is thick enough that the cell is not exposed to the laser radiation. The generated strain propagates through the metallic thin film and reaches the cell/film interface. There part of the sound propagates into the cell while the other part is reflected. The reflec-

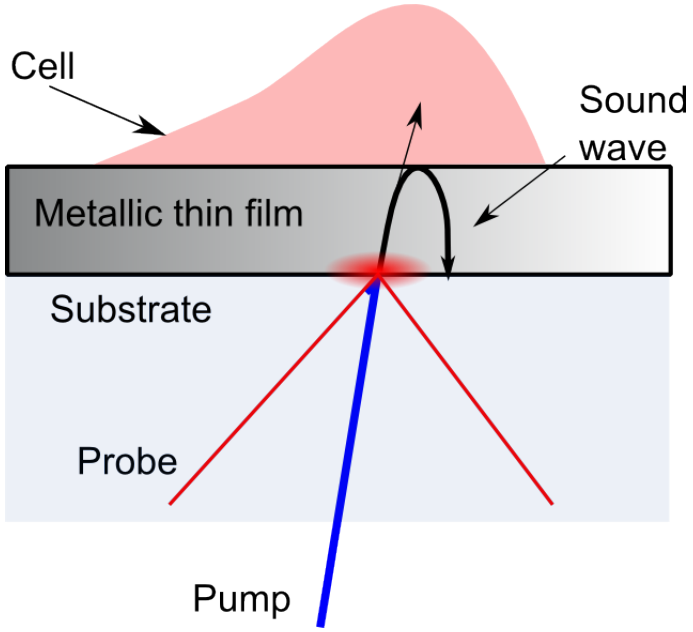

Figure 2.8: Schematic of picosecond ultrasound adhesion probing. Pump and probe are in contact with the transducer only and they are used to measure the acoustic reflectivity of the transducer/cell interface.

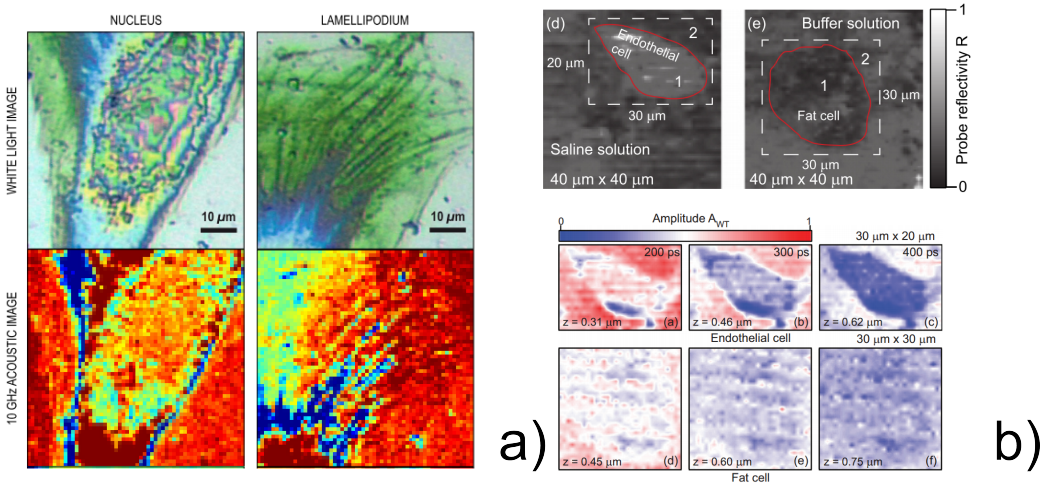

Figure 2.9: Recently reported cell images using PLU. (a) Map of acoustic reflectivity on a transducer/cell interface at 10GHz, (*Dehoux et al*[99], lincensed under CC BY 4.0). The cell is dehydrated but shows significant contrast. (b) Amplitude of the Brillouin oscillation signal on two different cells (Reprinted with permission from *Danworaphong et al*[100]. Copyright 2015, American Institute of Physics). The optical pictures of the cells are of very poor quality. The amplitude of the obtained Brillouin signals are shown for three time sections. For the fat cell there is virtually no information and for the endothelial cell there is a different attenuation rate from the media to the cell.

tion is detected by the probe beam. The amplitude of the reflection depends on the conditions at the interface of the cell and the titanium film allowing measurement of the attachment of the cell with good contrast and in a wide range of frequencies (see figure 2.9a). These results show promising potential by showing contrast of the inner features of the cell. This technique though, does not reach deep into the sample and is only sensitive to the vicinity of the transducer.

2.4.3 Future in PLU imaging of biological cells

PLU is a tool with great potential for cell imaging as seen in figure 2.9a. However, these are not based on Brillouin oscillations and lack of in-depth capabilities.

Other images recently reported based on Brillouin oscillations (amplitude of the Brillouin components, see figure 2.9b[100]) show little useful information where the optical pictures are arguably cells.

Additionally, all PLU images of cells reported so far have been performed on fixed, dehydrated specimens and are unlikely to be extended to living specimens. Possible reasons for this problem are:

- The damage induced by the laser in the cells given by the absorption of laser light.
- The damage induced by the heat generated in the sound generation process.
- Low acquisition speed of the pump and probe technique which is commonly based on a mechanical delay line.
- Low energy at the acoustic frequency of interest.
- Low signal amplitude due to the probe laser having to travel through the cell twice before reaching the detector.

- Low signal amplitude due to losses in the detection path, where multiple elements are used to separate beams travelling in opposite directions.

Even though important results have been achieved using the techniques reviewed in this section, being able to image the Brillouin frequency on living cells can provide us with a whole new look to cell imaging as the resolution would be capable to resolve cell features at sub-cellular level potentially providing important insights into cell biology.

2.5 Objectives

In summary, ultrasound in the GHz regime in the form of Brillouin oscillations is a promising technique for cell imaging. The ability to measure the speed of sound gives the opportunity to estimate mechanical properties such as the elastic modulus or the density and to image mechanically with high resolution (optical in x,y and acoustic in z). It has been demonstrated, among others, that the contrast of the Brillouin frequency at sub-cellular level is measurable. However, it is difficult to expand such measurements into imaging because of two principal limiting factors: exposure to laser light and heat. Both limitations are intimately related to the generation of ultrasound by a transducer. It is the main objective of this work to address those limitations by developing thin-film transducers to image the Brillouin frequency of single biological cultured cells.

2.5.1 Possible configurations for Brillouin detection

Detection of Brillouin oscillations in transmission is possible provided that there is high transmission for the probing wavelength λ_{probe}. Then if the reflected or transmitted beams are detected when the sample is in the upright position (lasers facing transducer, conventional way) or inverted (lasers facing glass substrate), four different detection schemes arise. Figure 2.10 shows the variations and the different paths followed by the

probe beam for each one of them.

The conventional Brillouin detection happens when the sample is upright (we will refer to it as conventional in reflection). In the proposed configuration in this work (details in the next section), the signals are detected from the transmitted beam with the inverse position (we will refer to it as inverted in transmission). Detection in transmission with upright sample (conventional in transmission) and reflected with sample upside-down (inverted in reflection) are possible as well (see figure 2.10).

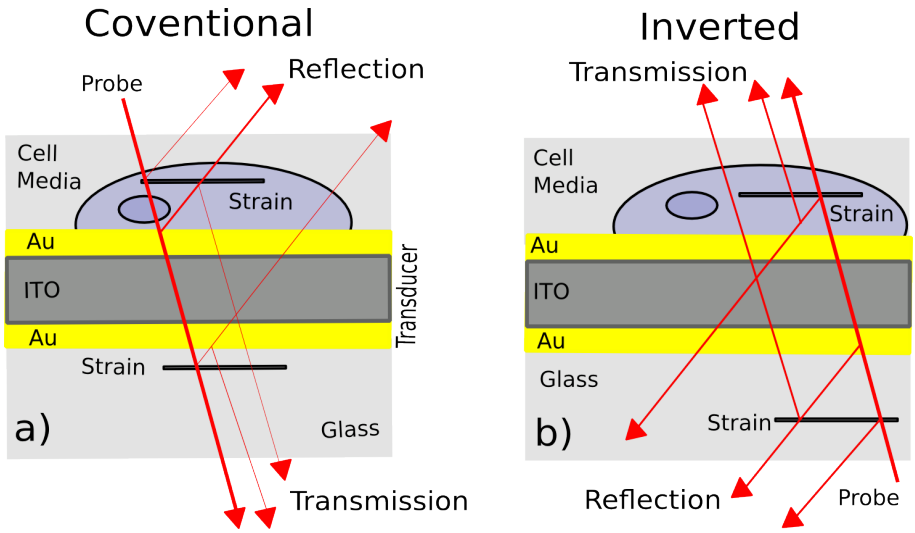

Figure 2.10: The high transmission transducer approach to Brillouin detection. (a) Conventional configuration where the whole of the light is expose to the specimen. (b) Inverted configuration used to protect the cells from heat, laser radiation (pump comes from top, not shown for clarity) and to simplify detection set-up.

The different configurations can be compared by their capability to protect the cells against probe and pump laser light. Table 2.1 shows this comparison assuming that the transmittance of the transducer is 30% for the probe and 10% for the pump beams. There is possible to see that in conventional detection (reflection or transmission) the cells sees the total amount of the input light plus the fraction of the beam that is reflected on the transducer for both laser beams. Compared to that, in the inverted configuration, it is possible to reduce the exposure of probe light to 40% while exposure

Detection	% of λ_{pump}	% of λ_{probe}
Conventional	150%	155%
Inverted	10%	40%

Table 2.1: Comparison of light exposure between conventional and inverted configurations using high probe transmittance transducer (30%) with 10% pump transmission. In the conventional configuration the reflected beam travels in and out the specimen increasing exposure beyond the input power (100%).

of pump light to 10%.

It is clear from table 2.1, that detection in transmission (inverted) has the ability to protect the cell undertaking PLU imaging. However, more light is available in the conventional detection mode which allows larger modulation depths but lower detection levels (due to losses in larger number of optical elements in the experimental array, see section 4.2).

Light detected by the inverted in reflection configuration could be used in the tip of a fibre as a probe. It is also be possible to detect both reflected and transmitted beams simultaneously. That allows the subtraction of the signals to increase SNR, as well as to extract information from the resonance of the transducer. Those possible applications are explored briefly in chapter 6.

2.5.2 The transmittance approach to the detection of Brillouin oscillations

Brillouin scattering is a useful tool to characterise transparent and semitransparent materials like semiconductors[90] dielectrics[101] or cultured cells[65]. It is the combination of a mechanical property (speed of sound) and an optical property (refractive index, see equation 2.13). This is interesting feature because it provides not only a way to image mechanically but to do it with high resolution. Line scans and low SNR images of the Brillouin oscillation amplitude have been reported (see section 2.4). However, images of the Brillouin frequency or speed of sound at GHz frequencies on living cells

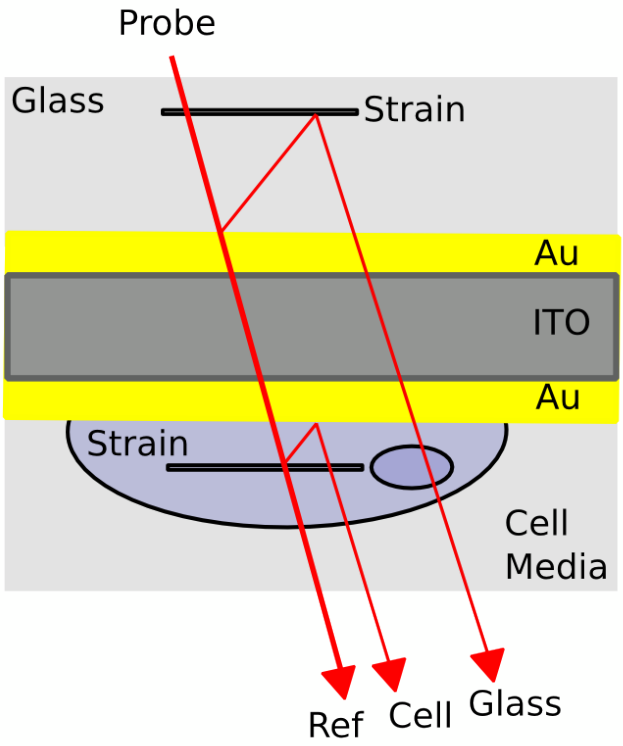

Figure 2.11: Transmittance detection of Brillouin scattering. The cells is partly protected from pump and probe radiation while there is no SNR loss. The heat produced by the absorption of the pump pulse is partially dissipated before reaching the cell.

have not been reported yet.

The transmission approach presented here intends to solve some of the difficulties to image the Brillouin frequency by protecting the cell from light exposure and also by simplifying the detection by using a fast data acquisition asynchronous optical sampling (ASOPS) pump probe system. The novel approach uses the transducer as a shield and transmission detection to reduce laser light exposure to the specimen. That is achieved by applying the laser beams through the transparent substrate and detecting the probe on the other side (see figure 2.11). This is achieved with a three layer thin-film transducer where the optical cavity formed by the metal-dielectric-metal configuration allows a design optimised for high transmission of the probe wavelength λ_{probe}(780nm).

This configuration also allows the pump beam to be blocked due to the high absorption of gold at λ_{pump}(390nm), while aiding heat dissipation.

Blocking λ_{pump} allows the increase of the input power without exposing the cell to additional light and higher input power means higher signal amplitude. It also increases acoustic energy in the band of interest given by the mechanical resonance, which also could boost signal amplitude.

The objectives of this work then are listed as it follows:

- To develop and test thin film transducers for the detection in transmission of Brillouin scattering on cultured cells.
- The transducers should provide protection against pump light exposure while maintaining SNR.
- The setup, based on a ASOPS system, will be used to increase acquisition speed compared to a mechanical delay line.
- To produce images of the Brillouin frequency on fixed and living cells.
- To use the time resolved measurements to section in depth and resolve the thickness or position of features of the cells.

Chapter 3

Thin film transducers applied to cell imaging

3.1 Introduction

Picosecond lasers can easily damage delicate subjects such as biological cells. The damage comes from two sources; heat and light absorption. The heat is produced by the absorption of light in the thin film used to generate the sound. The thin film is typically made out of titanium, it absorbs light strongly, efficiently generating sound and heat. Light absorption in the cell itself can also lead to cell damage by the interaction between light and the molecules that constitute the cell. These molecules can be damaged and cause cell malfunction, which leads ultimately to cell death. For the case of picosecond laser ultrasound it is not clear yet which source of damage is the most relevant. Moreover, low signal-to-noise ratio is common issue related to picosecond ultrasound experiments, the low levels of detection light and small modulation depth of the signals make necessary the use of extensive averaging.

In this chapter, the three thin-layer opto-acoustic transducer for the generation of GHz ultrasound is introduced. The optimisation of the transducer for the detection

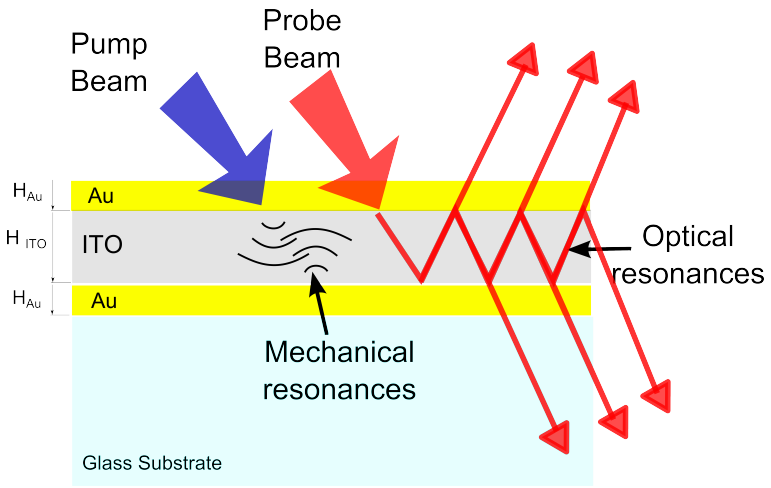

Figure 3.1: Metal-dielectric-metal configuration of the three layer transducer. The transducer is excited by ligth pulses (pump) which generates a mechanical resonance. The transducer resonance can be measured also by light pulses of diffrent frequency (probe)

of Brillouin oscillations without causing cell damage will be explored, with the aim to expand single measurements of the Brillouin frequency to acquire images. Optical models will be presented for the transmittance, reflectance and absorption. Mechanical models based on finite element modelling (FEM) will be presented and their results will be discussed in relation to design implications. Finally, based on the model results, a transducer optimised for Brillouin detection will be described.

3.1.1 The three thin layer opto-acoustic transducer

The transducer used in this work consists of three thin layers of gold, ITO (indium tin oxide) and gold as shown in figure 3.1. The transducer was initially designed to generate and detect GHz acoustic waves. However, it can also be designed to fulfil other purposes. The layers form a Fabry-Pérot cavity which has an optical transmittance and reflectance that depends on the cavity size (dielectric thickness H_{ITO} and metal thickness H_{Au}) and the optical wavelength. From the optical model described in this chapter, the transmission and reflection versus ITO thickness (H_{ITO}) for fixed gold

layer thicknesses and wavelength was calculated as shown in figure 3.2.

As the distance between the gold layers changes, the reflectance and transmittance experience a dip and a peak respectively. Around those areas the rate of change in transmittance/reflectance is high for a small change in distance between the layers. If an acoustic wave is compressing the transducer, it will change the distance between the layers and hence the instantaneous reflectivity/transmittance accordingly. Therefore a device designed with the correct dimensions can experience high sensitivity to incoming waves as a change in size of the optical cavity. This sensitivity is represented as the ratio of the change in the reflectivity or transmittance with respect to the change in the distance between the layers with the expressions $\delta \mathrm{R}/\delta \mathrm{H}_{ITO}$ and $\delta \mathrm{T}/\delta \mathrm{H}_{ITO}$ respectively.

Figure 3.2 bottom, shows the sensitivity of a device with 20nm gold layers. Assuming a single wavelength (780nm) and a unity input intensity, the sensitivity becomes $\delta \mathrm{R}/\delta \mathrm{H}$ and $\delta \mathrm{T}/\delta \mathrm{H}$ in nm^{-1} for the reflected and transmitted beams respectively. The model used to calculate the optical response is described in detail in section 3.2. We can see that for that particular example, the sensitivity is $0.04\mathrm{nm}^{-1}$ for the reflection case.

In the application proposed in this work (discussed on section 2.5.2) the detection mechanism is in the form of Brillouin oscillations is performed in transmission. For that reason, the static transmittance should be as large as possible to achieve large detection levels. This can be achieved at the peak of transmittance where the sensitivity is low (see figure 3.2). The cavity has also mechanical properties which are of interest. For instance, the response of the transducers to a pulse of light excitation defines the frequencies and amplitudes of which the transducer will radiate acoustic waves which are useful design parameters.

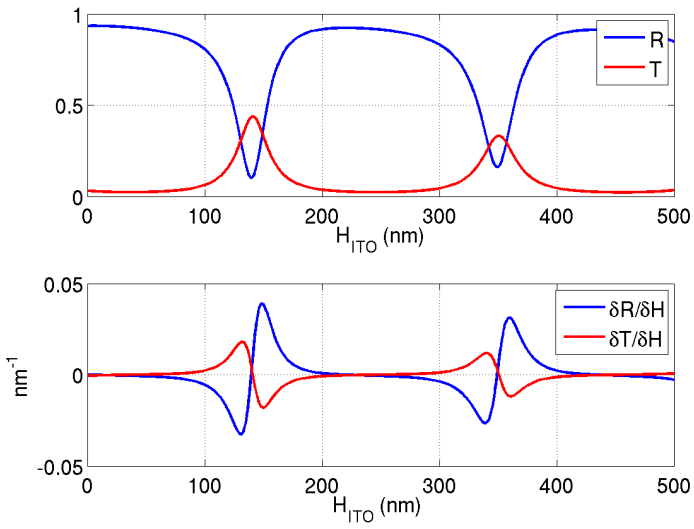

Figure 3.2: Optical behavior of a transducer against dielectric thickness (H_{Au}=30nm). Top, reflectivity and transmittance. Bottom, sensitivity to the change of the distance between metal layers. If the transducer is compress by a sound wave, the instantaneous reflectivity and transmittance will change depending on the sensitivity.

3.2 Optical characterisation of the thin-film transducers

In this section, the optical characteristics of the transducers for both pump and probe wavelengths are calculated. Based on Fresnel coefficients and the matrix transfer method, an optical model of the transducer is used to determine those characteristics. Snell's law allows the calculation of the angles of the reflected and transmitted beams propagating through a refractive index discontinuity. The amplitude of the transmitted and reflected beams and its relationship with the polarisation of the light is calculated by the Fresnel equations. This approach allows us to modelling of complicated multilayer systems such as the thin-film transducers used in this work.

Let us assume a incident plane wave and that the reflected and transmitted beams are also plane as well and the media is perfectly transparent.

$$\mathbf{E}_i = E_{0i} e^{i(\mathbf{k}_i \cdot \mathbf{r} - w_i t)}$$

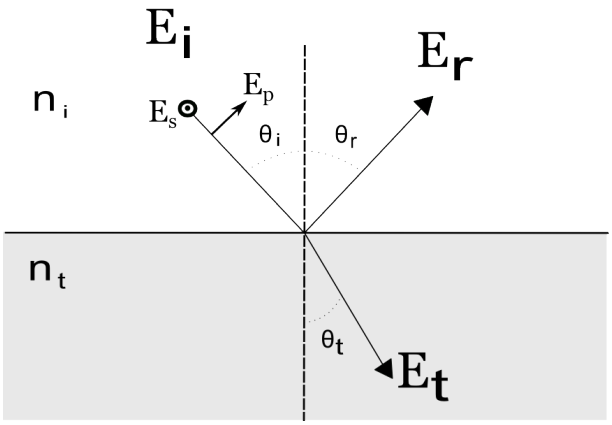

Figure 3.3: Reflection and transmission of a electromagnetic wave at an interface. Fresnel equations can be used to evaluate the amplitude of the reflected and transmitted at an interface between two materials.

For the case of such a wave propagating through a medium discontinuity, there are two cases where the equation can be solved, when $\mathbf{E}_i$ is perpendicular (s-polarized) or parallel(p-polarized) to the plane of incidence (see fig 3.3)

From the electromagnetic theory, the boundary conditions for the electric and magnetic components are; that the parallel component of the magnetic field $\mathbf{B}$ and the perpendicular component of the electric field $\mathbf{E}$ (s-polarization) are continuous across the boundary between the two media which are given by;

$$-\mathbf{B}_i cos\theta_i + \mathbf{B}_r cos\theta_r = -\mathbf{B}_t cos\theta_t \tag{3.1}$$

where θ_i,θ_r and θ_t are the incident, reflected and transmitted angles respectively and by

$$\mathbf{E}_i + \mathbf{E}_r = \mathbf{E}_t \tag{3.2}$$

Taking into account equation $\mathbf{E} = v\mathbf{B}$, where v is the speed of light in a given

media, we can rewrite the magnetic components of equation 3.1 as:

$$-\frac{\mathbf{E}_i}{v_i}cos\theta_i + \frac{\mathbf{E}_r}{v_r}cos\theta_r = -\frac{\mathbf{E}_t}{v_t}cos\theta_t$$

since $v_i = v_r$ and from Snell's law $\theta_i = \theta_r$:

$$-\frac{cos\theta_i}{v_i}(\mathbf{E}_r - \mathbf{E}_i) = -\frac{\mathbf{E}_t}{v_t}cos\theta_t$$

Writing $\mathbf{E}_t$ and $\mathbf{E}_r$ in terms of equation 3.2 and using the relation $v = \frac{c}{n}$, where c is the speed of light in vacuum and n the refractive index of the media, we can write expression for the ratio $\frac{\mathbf{E}_r}{\mathbf{E}_i}$:

$$\frac{\mathbf{E}_r}{\mathbf{E}_i} = \frac{\frac{n_i cos\theta_i}{c} - \frac{n_t cos\theta_t}{c}}{\frac{n_i cos\theta_i}{c} + \frac{n_t cos\theta_t}{c}}$$

where c cancels itself giving the ratio of amplitude of the reflected wave with respect to the incident as:

$$r_s = \frac{\mathbf{E}_{0r}}{\mathbf{E}_{0i}} = \frac{n_i cos\theta_i - n_t cos\theta_t}{n_i cos\theta_i + n_t cos\theta_t} \tag{3.3}$$

Similarly, for the the amplitude of the transmitted wave:

$$t_s = \frac{\mathbf{E}_{0t}}{\mathbf{E}_{0i}} = \frac{2n_i cos\theta_i}{n_i cos\theta_i + n_t cos\theta_t} \tag{3.4}$$

where n_i and n_t are the refractive indexes of the incident and transmitted media respectively with θ_i and θ_t as their angles as shown in figure 3.3. Now for the case when the electric field is parallel to the incidence plane (p-polarization), the boundary conditions for the magnetic and electric fields are given by:

$$\mathbf{B}_i + \mathbf{B}_r = \mathbf{B}_t$$

and

$$\mathbf{E}_i cos\theta_i - \mathbf{E}_r cos\theta_r = \mathbf{E}_t cos\theta_t$$

Following similar process as before we arrive at:

$$r_p = \frac{\mathbf{E}_{0r}}{\mathbf{E}_{0i}} = \frac{n_t cos\theta_i - n_i cos\theta_t}{n_i cos\theta_t + n_t cos\theta_i} \tag{3.5}$$

and

$$t_p = \frac{\mathbf{E}_{0t}}{\mathbf{E}_{0i}} = \frac{2n_i cos\theta_i}{n_i cos\theta_t + n_t cos\theta_i} \tag{3.6}$$

Equations 3.3, 3.4, 3.5 and 3.6 are known as the Fresnel equations and they give the relationship of amplitude of a wave depending on its incident angle and refractive index for parallel(p) or perpendicular(s) polarizations. Due to the simplicity of the geometry of our thin-film transducer, it was possible to produce a theoretical model of the transducers in one dimension. This approximation is fair since the width of the transducer is greater than the optical wavelength. The model consists of five layers including air, material$_1$, material$_2$, material$_3$, material$_4$ and air again. A flow diagram of this model is shown in figure 3.4. The software consists of two main parts; the main section which changes the parameters of the transducer (thickness, refractive index, incidence angle see figure 3.4a) and a second part that solves the transmittance and reflection for such parameters (see figure 3.4b). The second part relies on an optical matrix transfer method and Fresnel coefficients to construct a solution of the multiple layer structure assuming homogeneous plane-parallel faces[102].

For this model the transducer is composed of multiple layers with complex refractive indexes. The amplitudes on each layer are related by a product of 2x2 matrices in similar order to the transducer itself. One matrix is used to include the effect of an interface (refraction matrix $\mathbf{R}$) in terms of the complex Fresnel coefficients for parallel

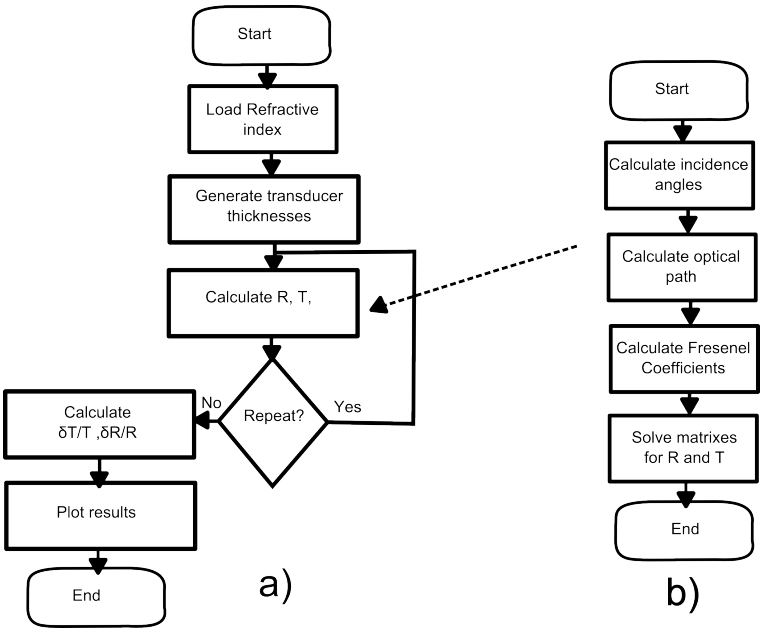

Figure 3.4: Flow diagram of optical model used to calculate sensitivity, transmittance and absorption for the transducers at λ_{probe} and λ_{pump}. (a) Main algorithm to calculate R and T for a range of thickness of the layers based on (b) where R and T are calculated for a particular combination of the thickness of the layers.

and perpendicular polarizations tp, ts, rp, rs:

$$\mathbf{R}_{12} = \frac{1}{t_{p12}} \begin{bmatrix} 1 & r_{p12} \\ r_{p12} & 1 \end{bmatrix} \tag{3.7}$$

and another matrix was used to include the propagation (propagation matrix $\mathbf{P}$) in terms of the optical path ($\delta = ln$, where l is the path length and n the refractive index) induced to the beam on each layer ($\delta_1..\delta_N$):

$$\mathbf{P}_1 = \begin{bmatrix} e^{i\delta_1} & 0 \\ 0 & e^{-i\delta_1} \end{bmatrix} \tag{3.8}$$

By multiplying all the matrices on the same order as they are arranged in the actual transducer, a transfer Matrix $\mathbf{M}$ is then:

$$\mathbf{M} = \begin{bmatrix} m_{11} & m_{12} \\ m_{21} & m_{22} \end{bmatrix} = \mathbf{R}_1\mathbf{P}_1...\mathbf{R}_{N-1}\mathbf{P}_{N-2} \tag{3.9}$$

where N is the number of layers. Then the solution for the system on with infinite layers ad the edges is given by:

$$\begin{bmatrix} E_i \\ E_r \end{bmatrix} = \mathbf{M} \begin{bmatrix} E_t \\ 0 \end{bmatrix} \tag{3.10}$$

where the incident field is normalised E_i=1. Solving the equation for the reflected E_r and transmitted E_t electric fields, the total transmittance and reflectance for a given wavelength and polarisation for a transducer design is given by;

$$T = |E_t|^2 = |\frac{1}{\mathbf{M}_{11}}|^2$$

and

$$R = |E_r|^2 = |\frac{\mathbf{M}_{21}}{\mathbf{M}_{11}}|^2$$

The transmittance T and reflectance R were calculated for normal incidence and from there absorption (α=1-R-T) and sensitivity (δT/δH,δR/δH) were evaluated. Once having the reflectivity and transmission, it was possible to calculate the individual reflectance and transmittance for the first layer as:

$$\begin{bmatrix} 1 \\ E_r \end{bmatrix} = \mathbf{R}_1\mathbf{P}_1 \begin{bmatrix} E_{t2} \\ E_{r2} \end{bmatrix} \tag{3.11}$$

and the rest of the layers is given by

$$\begin{bmatrix} E_{tN-1} \\ E_{rN-1} \end{bmatrix} = \mathbf{R}_N\mathbf{P}_N \begin{bmatrix} E_{tN+1} \\ E_{rN+1} \end{bmatrix} \tag{3.12}$$

where N=3... N-2. This allowed to evaluate the absorption occurring at each layer as[103]:

$$\alpha_N = n_N(|E_{rN}|^2 - |E_{rN}|^2) + n_{N+1}(|E_{rN+1}|^2 - |E_{rN+1}|^2) \tag{3.13}$$

where the refractive indexes are only their real parts. The results of these calculations are presented in the following sections and are used to understand the optical performance of the transducers proposed here. The model also makes further assumptions; plane optical (single wavelength) and acoustic waves and to calculate the sensitivity, the change in thickness induced to the gold layers is not considered. This is a fair approximation since the acoustic wavelength is considerably larger than the thickness of the gold layers. Moreover, the results show good agreement with experimental results as shown in chapter 5.

3.2.1 Probe wavelength (780nm)

Both detection and generation of ultrasound occur in the same transducer, however for clarity we will reefer, when appropriate, to detection transducer to the optical properties at the probing wavelength and generation transducers to the optical properties at the pump wavelength. The probe beam (780nm) is used to probe the mechanical wave generated by the detection transducer by measuring variations in the beam intensity at the detector. The quality of the signals seen by the probe will depend on the amplitude of the generated waves, the amount of noise, the sensitivity of the device and the amount of light detected. In this section, we will concentrate on the last two. The generation efficiency and noise are discussed in section 3.2.2 and 4.4.2 respectively.

Figure 3.5 shows the results of the model for a wide range of gold (5-60nm) and ITO (100-200nm) thicknesses. There, transmittance T, reflection R, and sensitivity for the reflected (δR/δH) and transmitted (δR/δH) beams are presented. In figure 3.5a we can see that the sensitivity for the reflection case reaches a maximum of 0.5nm^{-1} while the transmission (figure 3.5c) case is about half of this value. This means that the reflection case is twice as good for detecting incoming waves. The transmission and reflection shown in figure 3.5d and 3.5b respectively show similar shape that nearly complement each other to the unity. Maximum transmittance for thick gold layers (20-30nm) can be as high as 0.35 which would be suitable for detection in transmission.

3.2.2 Pump wavelength (390nm)

The pump beam is the mean by which a soundwave is created by the thermoelastic effect. The optical energy of a pulse of light is instantaneously absorbed by the generation transducer creating rapid thermal expansion. This expansion induces the propagation of a broadband acoustic wave. As the acoustic energy propagates, part of that energy is transmitted to the substrate and specimen while the rest resonates inside the generation transducer (see section 3.3).

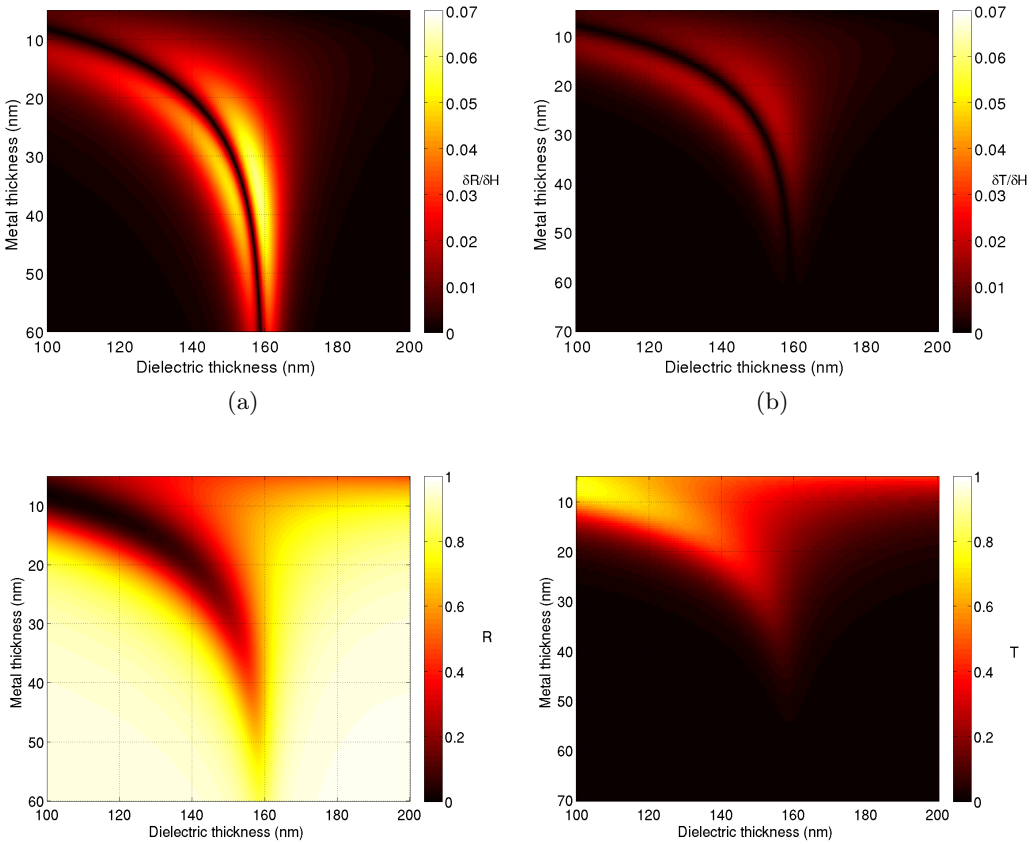

Figure 3.5: Transducer sensitivity δR/δH (a) δT/δH (b), reflectance (c) and transmittance (d) at λ_{probe} for a range of layer thicknesses.

The optical absorption coefficient of gold at 390nm is high ($\alpha = 61.5\text{x}10^6$) [104] and approximately five times bigger than at 780nm, leading to a short skin depth (δ_p =32nm). In terms of design, this is a very good feature since it means that regardless the dimensions of the generation transducer layers, as long as they are comparable to the skin depth, the generation transducer will generate waves efficiently. That versatility allows the tuning of the layers for high transmission and low sensitivity of λ_{probe} without compromising acoustic generation.

Figure 3.6 shows the results of the optical model for λ_{pump}. In figure 3.6a, the

absorption (from the all the layers) remains fairly flat with variations of less than 20%. In figure 3.6b, the transmission drops rapidly with gold thickness suggesting that little improvement to the exposure reduction can be achieved above 12nm of gold. However, thicker gold layers can make the device resonate at lower frequencies because the round trip time of the acoustic wave inside the generation transducer is increased (see section 3.3).

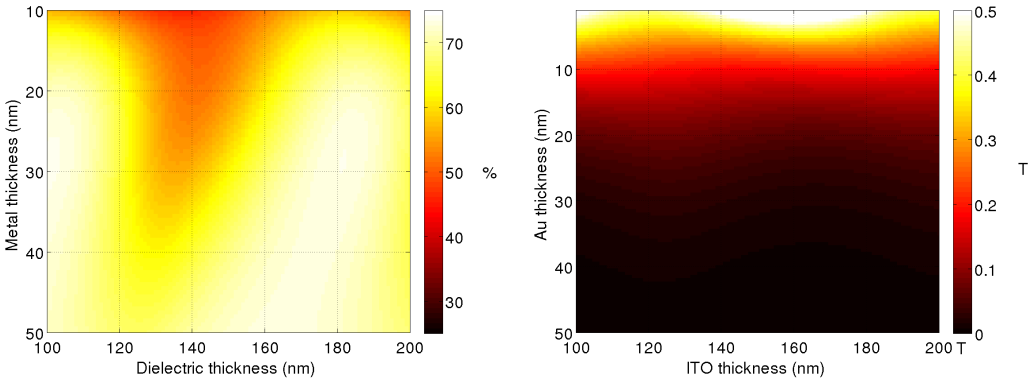

(a) (b)

Figure 3.6: Result of optical model for pump wavelength. Percentage of light absorbed by the transducer (a) and its related transmittance (b) at λ_{pump} in a range of thicknesses

3.2.3 Layer material choice

Metal layers of gold are used because of their suitability for our application (transmittance detection of PLU) in comparison to commonly LU materials like aluminium or chromium. Nevertheless, the performance of gold has been compared against materials that can be applied with a sputter coater, as well as those commonly found in the literature (gold, silver, copper, chromium, aluminium and titanium). This comparison is specifically for the application described on section 2.5.2 and it is based on the models described in section 3.2.

First, the transmittance at λ_{probe} (780nm) for detection transducers with 15nm of

H_{metal} and varying H_{ITO} was modelled. Figure 3.7a shows the result of these models. From there, is possible to see that aluminium chrome and titanium have very low transmittance which makes them unsuitable for detection in transmission. The three remaining materials (gold, copper and silver) show similar capabilities with maximum transmittance of approximately 0.5.

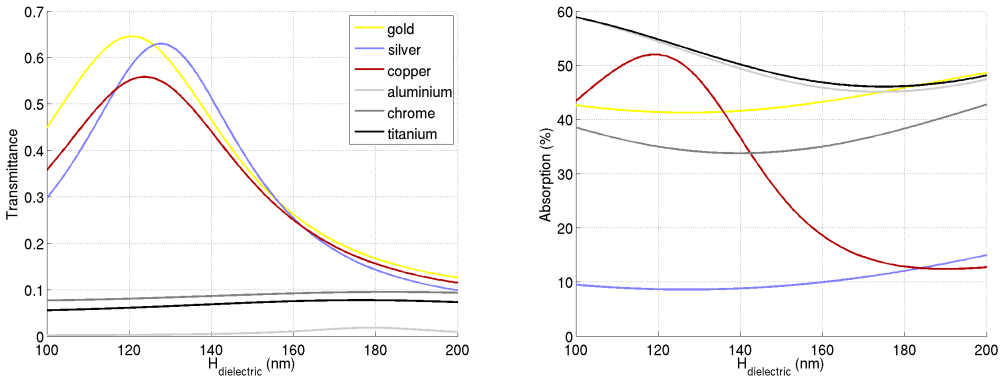

(a) (b)

Figure 3.7: Comparison of the performance of detection transducers working in transmission build from different metals. (a) Transmission at λ_{probe}(780nm). There chromium, titanium and aluminium show poor transmittance which make them unsuitable for detection in transmission. (b) Absorption at λ_{pump} (390nm). There, silver shows low absorption becoming poorly suited to generate acoustic waves.

Absorption was also calculated for generation transducers (λ_{pump}=390nm) and 15nm of H_{metal}. Figure 3.7b shows that the absorptions for gold and copper are similar, however for silver absorption is ∼4 times smaller meaning that it will generate smaller acoustic waves. That leaves only gold and copper. However, the compatibility of copper for cell culture is poor whereas gold has been widely demonstrated as a suitable cell culture substrate.

If a different deposition technology is used (such as evaporation or radio-frequency sputtering), then the availability of different materials could lead to a wider range of alternatives. This is particularly critical for the dielectric case because ITO is the only dielectric available for the sputter coating technology used in this work (DC sputter-

ing). ITO is not the ideal material since it has significant absorption which affects the performance of the optical cavity (see section 6.2).

3.2.4 Detection transducer sensitivity to plane acoustic waves

The main detection mechanism used in this work is in the form of Brillouin scattering. Because of the detection transducer sensitivity to the optical cavity size (H_{ITO}), its own resonance will be detected and that is an extra effect that needs to be considered when designing a transducer for detection of Brillouin scattering in transmission.

For the purposes of Brillouin detection we want to know what the acoustic resonant frequency of the generation transducer will be, and how sensitive the detection transducer is to this frequency. The more sensitive the detection transducer is, the bigger the signal additional signal will be. Sensitivity is shown in figure 3.5 for transmission and reflection. As mentioned before, the best sensitivity is for the reflectivity case. There is also a dark fringe in the sensitivity maps related to the maximum transmittance or reflectance. Experimentally, this dip does not completely eliminate the detection transducer response. A possible reason for this is that the model makes several assumptions; the incident light is a single wavelength plane wave and the acoustic wave is also a plane wave that only affects the inner layer of the cavity. However, the incident light is convergent, the bandwidth of the laser is relatively broad ($\Delta\lambda \approx \lambda^2/\sigma \approx$4nm) and the acoustic waves also affect the gold layers.

The characteristics of the devices, described in this chapter, for ultrasonic generation and detection in the GHz range could be exploited for cell imaging in a similar way to Brillouin scattering. While this is not widely explored in chapter 5, it will be briefly addressed in chapter 6.

3.3 Mechanical characterisation of generation transducers

From a mechanical point of view, the generation transducers are simple three layer structures which resonate when excited by a laser pulse and, if in contact with another medium, radiate elastic waves. The resonance frequency of the transducer is important for several reasons, depending on the application. When the generation transducers are working as acoustic sources, it is important to know their resonance frequency, so independently fabricated detection transducers can detect each signals from generation transducers. If the detection transducers are used for Brillouin detection, the resonance frequency of the generation transducer becomes an extra signal which may overlap the signal of interest. However, as we will see in section 3.4 and chapter 6 the detection transducer can be designed and applied in different ways.

An analytical solution of the mechanical motion of the generation transducers is not easy to formulate, instead we use a finite element (FE) method to simulate the motion of the generation transducers when exited by a pulse of light. The FE method has the ability to break a difficult problem (i.e a complex structure) into small parts (known as meshing). By linking the solution of each part, it is possible to reach to an approximate solution of a given problem, which often does not have an analytical solution.

There are graphically-based computer applications to solve physical problems with the finite element method. These take advantage of the power of modern computers to reach to the solutions. In this work, *Comsol Multiphysics* version 3.5a software was used. The model was created using this software and then exported to matlab(2007) to iterate the model for a range of different dimensions of the generation transducer layers.

The model used to simulate the generation transducers was simplified to axial symmetry(r, z, thermal) and single dimension (z, thermo-mechanical). The model is

thermally-mechanically coupled, which takes the laser input as an injection of energy. The input is related to the laser power, pulse width and absorption of the layers in the generation transducer. Then the model computes thermal expansion and motion related to the increase in temperature taking place where the laser light is absorbed. The first part of the model (thermal) solved the heat equation:

$$\rho C_p \frac{\delta T}{\delta t} - \nabla(k\nabla T) = Q \tag{3.14}$$

where ρ is the density of the material, C_p the heat capacity, k the thermal conductivity, T the temperature, t the time, ∇ the Laplace operator and Q the energy flux. The subdomain (layer) initial conditions for the substrate and the water were Q_0=0, but for the transducer layers for average power (transient and steady state):

$$Q_0 = \frac{P_{Avg}}{\pi W_0^2 \delta_p} e^{-\frac{r^2}{W_0^2}} \tag{3.15}$$

and for a single pulse (transient only):

$$Q_0 = \frac{P_{peak}}{\pi W_0^2 \delta_p} e^{-\frac{r^2}{W_0^2}} \frac{t e^{-\frac{t^2}{t_0^2}}}{t_0} \tag{3.16}$$

where P_{avg} and P_{peak} are the average and peak power absorbed by each layer respectively, W_0 the focal spot radius, t_0 the pulse width and δ_p the skin depth which in this case corresponds to the thickness of each layer given that all the layers are thinner than their corresponding skin depth, hence optical intensity inside of each absorbing layer is approximated to be constant for simplicity. The first exponential on both equations 3.15 and 3.16 represents the change in intensity as given by the laser spot and the second exponential in equation 3.16 represents the change in intensity over time given by a single pulse. The boundary conditions and geometry where set as axial symmetry for the inner boundaries and set temperature (T_{ref}=20^{o}C) for the surrounding ones.

Thermal properties			
Material	Thermal conductivity (W/mK)	Heat capacity(J/KgK)	Thermal expansion coefficient (K^-1)
Silica Glass	1.38	703	2203
Sapphire	35	730	0.55x10^{-6}
Gold	317	129	6.5x10^{-6}
ITO	10.2	700	14.2x10^{-6}
Water	0.6	4180	0.5x10^{-6}
Mechanical properties			
Material	Density (Kg/m^3)	Young modulus(GPa)	Poisson's ratio
Silica Glass	3965	73.1	0.17
Sapphire	19300	400	0.22
Gold	7140	70	0.44
ITO	998.3	150	0.25

Table 3.1: Properties of materials used in FE models.

The solution for the mechanical motion within the transducer can be simplified to a single dimension problem since the generated acoustic wave within the transducer can be considered a plane wave. This assumption is valid, according to Rayleigh criteria, if the distance from the generation point to the detection is less than the ratio of the the square of the spot size D to the acoustic wavelength λ_a (D^2/λ_a) which is this case is approximately 50μm.

The transient heat information was then used to calculate initial strain to solve the displacement of the layers induced by the laser pulses for a transducer submerged in air. The initial stress is thermal and is given by

$$\eta_0(z) = \beta(T_0(z) - T_{ref}) = \frac{\delta u_z}{\delta z}$$

where $T_0(z,t)$ is the initial temperature change occurring in the layers and β the thermal expansion coefficient. Solving for equations 2.3, 2.4, and 2.5, it was possible to evaluate the thickness of the ITO layer (H_{ITO}) by monitoring the displacement at the boundaries.

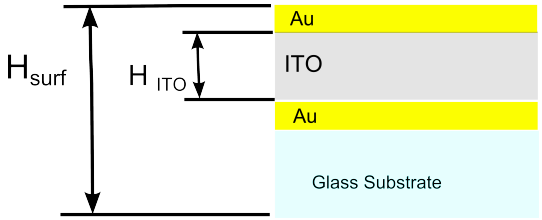

Figure 3.8: Surfaces monitored from FE simulations. The transducer is sensitive to the changes on H_{ITO} and the displacement from H_{surf} is related to the amplitude of the Brillouin scattering.

Figure 3.9 shows an example of the change of H_{ITO} and H_{surf} with respect to time (δH_{ITO} and δH_{surf} respectively, see figure 3.8). The traces are simulations of the effect induced by a laser pulse(λ_{pump}) into the transducer. The modelled generation transducer has 30-160-30 nm of gold ITO and gold with each layer absorbing $\sim$ 55%, 4% and 8% of pump energy respectively. The transducer is in air and attached to a glass substrate. Figure 3.9a corresponds to δH_{ITO} vs time while trace shown in figure 3.9c is represent the same but for δH_{surf}. From the traces it is possible to see the initial impulse resonating and quickly decaying. The Fourier transform shows a resonant frequency of approximately 8GHz.

The low frequency content seen in figure 3.9c from the motion of H_{surf} is the actual displacement that radiates waves into the specimen. This has contributions on a wide range of frequencies helping to detect Brillouin scattering even if the transducer resonance frequency is significantly different than the Brillouin frequency.

3.3.1 Frequency response of the transducer

The FE model was iterated for different gold and ITO thicknesses of the generation transducer keeping the same amount of pulse energy ($\sim$5pJ). The aim was to investigate the resonance frequency and amplitude of δH_{ITO} and δH_{surf} over time for the same range of thicknesses presented for the optical models. In this way, a full set of mechanical performance information is obtained for design purposes.

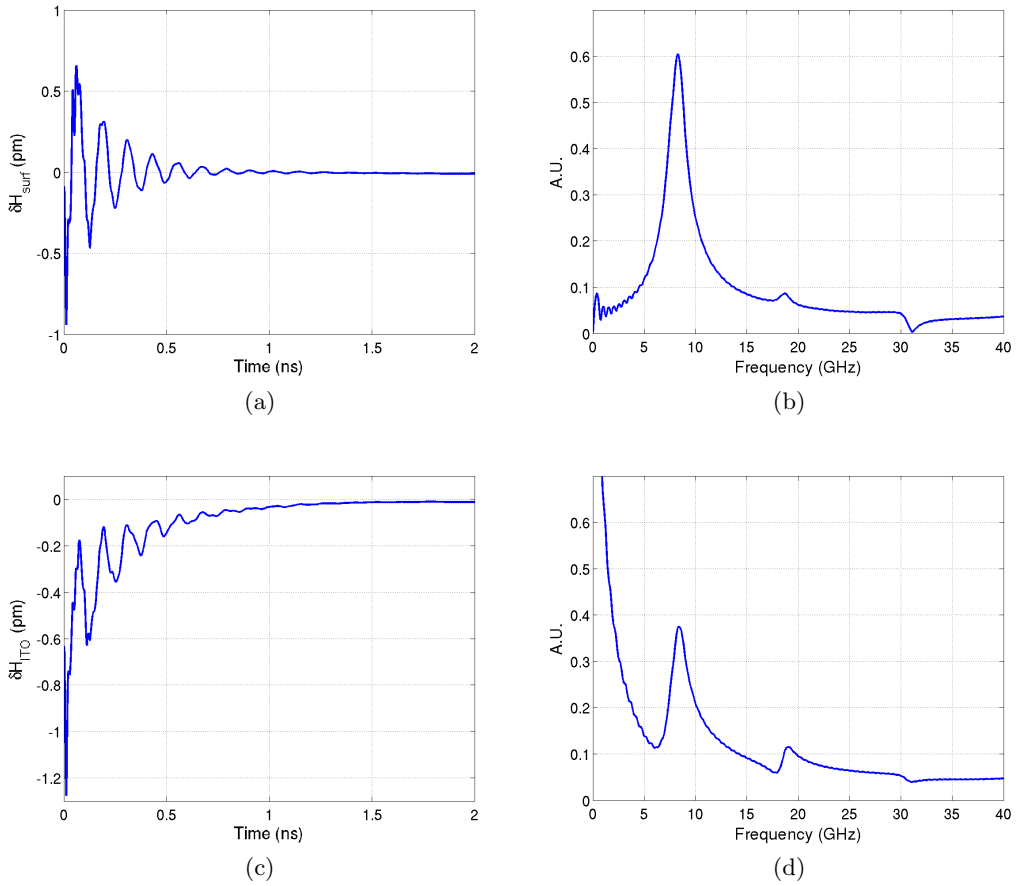

Figure 3.9: Simulation of the mechanical motion of a transducer with 30nm gold layers and 160nm ITO layer. (a) Modulation of H_{ITO} and its Fourier transform (b). (c) Motion of top layer with respect to origin H_{surf} and its Fourier transform (d).

Since the detection transducer is optically sensitive to δH_{ITO}, the resonance frequency will be also detected in a Brillouin oscillation experiment which could provide additional information. The top surface motion (δH_{surf}) is related to the radiated bandwidth which is important since we want to know how much energy is available for Brillouin detection.

Figure 3.10a shows the result of the calculations described above. Resonant frequencies are in the range of 5-20GHz. However, if we overlap the zones of high optical sensitivity from figure 3.5, then the range of observable resonances is from 6 to 16GHz.

In any case, there is opportunity for resonance frequency tuning. As for the amplitude (see figure 3.10b), the maximum increment of H_{ITO} grows for devices with thicker gold layers and stays fairly constant against ITO thickness. Maximum change of H_{ITO} is from 0.2pm to 1.6pm on the investigated range for a 5pJ pulse.

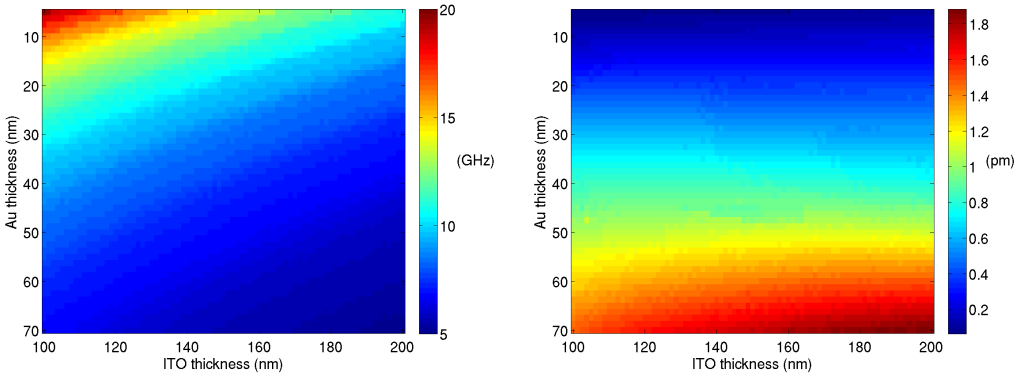

Figure 3.10: Resonance of generation transducers when excited by a pulse of light. (a) Frequency and (b) amplitude of the motion of the transducers for a range of thicknesses.

Amplitude at the Brillouin frequency

As part of the generation transducer design, optimization for Brillouin detection is relevant. By evaluating how much energy is available for Brillouin detection for each set of thicknesses or design point, we can determine if any particular design point is more suitable for the band we are interested in, and from there complement the design criteria.

A similar frequency analysis is performed calculating amplitude at 5.5GHz rather than at the resonance frequency. The full bandwidth obtained from the top layer (H_{surf}) motion will be also used, since it is related to the radiated bandwidth into the sample and, consequently, to the amplitude of the Brillouin peaks.

Figure 3.11b, shows the spectrum of the transducer response for devices with 20nm

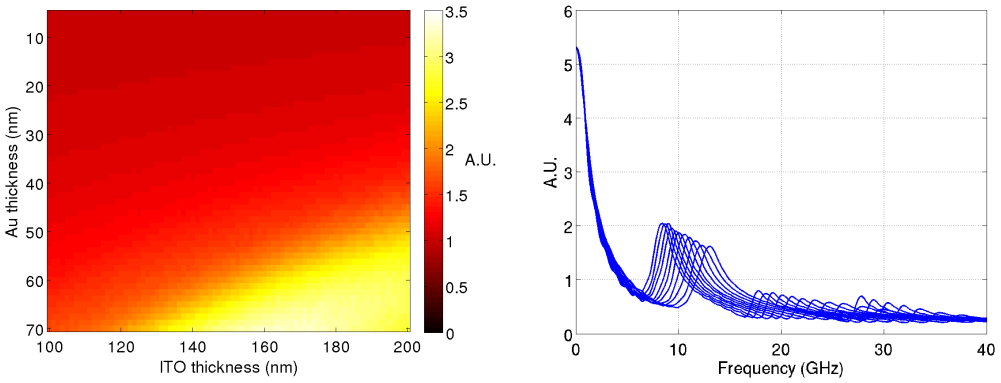

(a) (b)

Figure 3.11: Simulation of the amplitude of the motion of the transducer at 5.5 GHz. (a) Amplitude of the generated wave at 5.5GHz. (b) Example of the Fourier domain of the generated waves for fixed H_{ITO} and increasing gold layers. There is possible to see that the resonance peak shifts towards lower frequencies potentially providing an increase in the Brillouin signal detected in experiments.

of gold and 100 to 200nm of ITO. There are strong low frequency components related to the initial strain generated by the laser pulse which gives the opportunity to perform Brillouin detection. However, as the resonance shifts towards lower frequencies with thicker layers, the amplitude at 5.5GHz increases as well by a small amount.

Figure 3.11a shows an image of the amplitude at 5.5GHz for our range of design points. There is very little variation over the range except at the right bottom corner where the amplitude rises. This rise in amplitude is because the resonance frequency of the devices sits in the middle of the 5.5GHz. Unfortunately, we can not take advantage of this effect at the moment since the gold layers needed for this have a thickness such that it will be difficult to detect in transmission. Additionally, the sensitivity to the resonance may still be present and it might not be separable from the signal of interest by signal processing.

3.4 Defining design parameters

For Brillouin oscillations to be detected in cells, the cells have to be exposed to short laser pulses which can cause damage. For example, light absorbed by the cells can produce localised heat that eventually deteriorates the health of the cell. For longer wavelengths, the thresholds are fairly high ($\sim$1mW)[105], however for shorter wavelengths, the absorbed energy not only creates heat but also breaks molecular bonds which causes quick degradation of the health of a cell[106]. Finally, the heat produced by the light absorbed by the metallic substrate is also a mechanism for the cell to experience damage.

In order to prevent damage, its necessary to reduce the amount of light and heat energy absorbed by the cell. When detecting Brillouin oscillations, it is fundamental to have at least the probe beam travelling through the cell coaxially to the soundwave. In this section, we explore the practicalities of using the thin-film three layer transducers to reduce light exposure and improve detection.

3.4.1 Cell requirements and compatibility with PLU

Living cells require a highly controlled environment to remain healthy; constant flow of nutrients, management of waste, temperature control and CO_2 balance. If any of those conditions are not carefully controlled, then the cells health will deteriorate rapidly and the results of any experiment might be compromised. Ultrasound experiments based on the acoustic microscope in the low GHz range have been performed on living cells with no evidence of damage[27], so ultrasound can be dismissed as intrinsically harmful.

For the case of Brillouin detection via PLU on living cells, there are two main sources of damage. The first is the heat produced by the absorption of light in the transducers where normally the cell would grow (typically a single thin-film layer of titanium). Practically it is very difficult to measure changes in temperature in such a small area, however studies reported in Audoin *et al*[66] show very small temperature rise

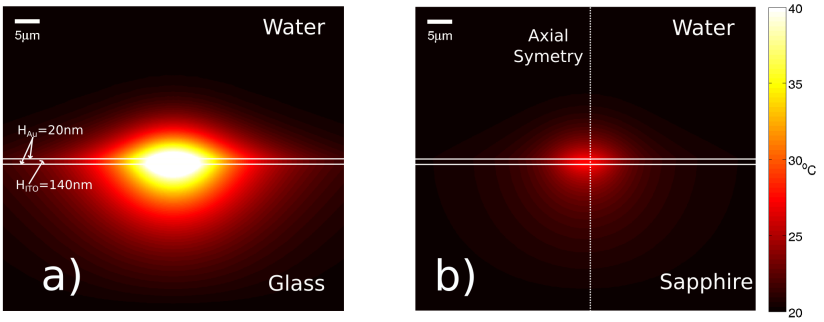

Figure 3.12: Steady state temperature distribution due to pump absorption. (a) Temperature distribution for a 1mW of average pump power using glass substrate. (b) Same using a sapphire substrate. A reduction of 20^oC at the cell/substrate interface is achieved by using a sapphire instead of a glass substrate. The geometry used for the FE model (gold layers shown as white lines) and boundary conditions are shown. This result is for a 20-140-20nm transducer which present absorption of 25%, 19% and 6% respectively.

and it is not considered as a problem if there is not cumulative effect on the temperature at a single examination point. However, those studies were performed on single point measurements. For the case of a two dimensional scan the situation might be different; it is unknown if the high number of measurements over a single cell on a short time scale has any additional impact compared to a single point measurement.

The steady state analysis, resulted from the FE model described in section 3.3, is shown in figure 3.12. It shows that for the same average input power (1mW, which is partially absorbed by the layers), there is a reduction of the temperature at the water/transducer interface of approximately 20^oC when changing the substrate material from glass to sapphire. At room temperature, the temperature distribution observed using sapphire is still safe for cells unlike the case when using glass.

The transient temperature profile is shown in figure 3.13. For the case of a single pulse (Fig. 3.13a), is possible to see that the temperature rise at the gold/cell interface (solid blue) is smaller than the one for the gold/substrate interface (solid red). However, as time goes on, temperature in both surfaces becomes the same which implies that thermally having the cell away from the main heat source (first gold layer) does not

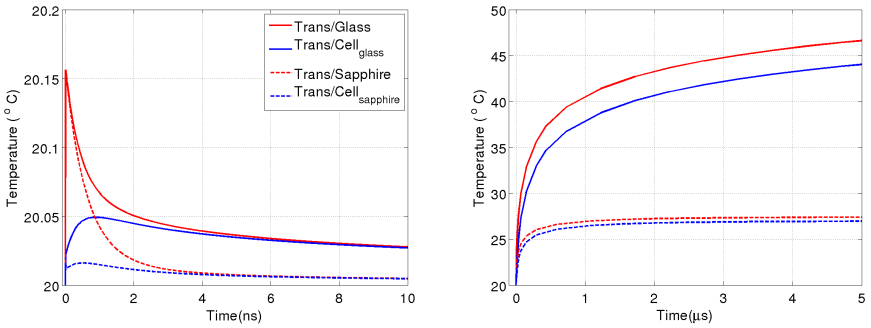

(a) (b)

Figure 3.13: Temperature rise due to pump absorption. Red lines represent the transducer/substrate interface and Blue lines the transducer/cell. Solid lines represent glass substrate while dotted represent sapphire. In both cases there is a reduction of the instantaneous temperature rise on the gold/transducer interface compared with the gold/substrate one. By the end of the measuring window (10ns), the temperature on both interfaces is the same. Sapphire however shows greater heat dissipation which may benefit viability for living cells

reduce heat exposure significantly. For the case of average power, (see figure 3.13b), the system reaches steady state after approximately 5μs of exposure. This means that the transient is too fast compared with the acquisition of a single trace (100μs) to contribute significantly to the temperature distribution calculated from the steady state calculation.

The accuracy of these models are difficult to validate, however they provide a good idea of how the change in substrates can produce a significantly different outcome.

The second source of damage is absorption of laser light. It is well known that the cells are sensitive to shorter wavelengths, specially in the ultraviolet region with intensities as low as 0.5 pJ/μm^2 [107]. For longer wavelengths, the allowed threshold is reported to be high ($\sim$1mW, near infrared NIR,150fs pulses [105]). These reported values for cell damage for UV and NIR give a reference for acceptable power levels to use. The actual power limit might be different for each sample but we looked to use the largest possible power levels that leaves no apparent damage. For a living cell, it is possible to confirm cell state by observation and use of fluorescent markers for living (calcein-AM)

or dead(propidium iodide, see section 5.4.4) cells.

3.4.2 Transducer optimised for Brillouin imaging of biological cells

Optimal Brillouin signals depend on the characteristics of the specimen and the transducers. Parameters like photo-elastic coefficient and acoustic impedance will vary with each material, affecting double the amount of transmitted acoustic energy to the specimen and the scattering efficiency. However, based on the models presented on this chapter, we can use the transducers characteristics to predict what the best design should be.

For the purposes of this work, the most important feature is to protect the specimen while keeping practical SNR. So the design trade offs are as follows:

- Thicker gold layers mean better protection but lower transmittance.
- Higher transmittance at thicker gold layers can be achieved with very narrow fabrication tolerances.
- Devices that resonate at lower frequency, can increase the energy on the Brillouin frequency but the resonance might be difficult to separate from the signal of interest.
- Higher absorption of pump light can increase acoustic amplitude but also increases temperature rise, which could damage the specimen.

Having these considerations in mind and based on the result of the optical and mechanical models, a range of layer thickness can be selected for optimal performance in the TI configuration. A 30-150-30 design will be very good protecting the cell (5% pump exposure) while giving approximately 0.3 transmitted light for good detection levels. It will resonate at around 10GHz which is spectrally far enough from the Brillouin signal of interest(5-6GHz) so it is easy to separate.

Unfortunately this device has tight fabrication tolerances, which in a system with a wide variation like the sputter coater used for this work, becomes challenging to make (not for better coaters). Instead, thinner gold layers of 20nm and ITO of 145 were selected; that gives less protection to pump laser (10% exposure) but the fabrication tolerance is much broader. The device will resonate at a higher frequency, making it easier to separate from the Brillouin signal. For example, devices with gold layers from 20 +/- 5nm and ITO of 145+/- 15nm will be useful to perform Brillouin detection in transmission on biological cells. It will have round 30-40% transmittance on λ_{probe} and round 10-15% on λ_{pump} and a resonance frequency from 12 to 14GHz. More importantly it will be easy to fabricate due to the lower tolerances.

3.5 Transducer fabrication

Cleaning of substrates

For the purposes of this work, transducers were fabricated as large plates. This allows the cells to grow on a smooth surface. Discussions on how to make them smaller in all dimensions can be found in[88]. Several glass types such as optical grade windows, microscope slices and coverslips were used as substrates. Before starting deposition, the substrates were cleaned. This process has four steps involving submersion of the substrates in a solvent inside an ultrasonic bath (Fisher SW3H). The solvents used were ethyl-lactate, acetone, methanol and isopropanol applied in that order and in 8 minutes cycles. The substrates were rinsed with the next solvent before being submerged in it. After the last cycle was finished, then they were dried with pressurised nitrogen.

Deposition of thin-film layers

Depositions of gold and ITO were performed with a sputter coater (Emitech K575X). The K575X has a crystal film thickness monitor which allows to control the amount

of material deposited. However, the poor accuracy of this method required, for convenience, an additional validation measurement (see section 3.5.1). This measurement allows the dimensions of the transducer to be measured with good accuracy which allows the prediction of their performance based in the optical and mechanical models.

Deposition of polystyrene layers

Polystyrene (PS) thin-films were some times used as insulation or spacing layers. To deposit them, spin coating method was used[108]. A toluene solution ranging from 7.5 to 15wt% PS was deposited on top of the substrate before spinning it. The substrate was accelerated to 2000 revolutions per minute for 30 seconds. To cure the coating, the substrate was heated to 100^o C for 60 minutes which produced layers of approximately 1μm.

3.5.1 Transducer layer characterisation

It is of great importance to know the dimensions of the devices with good accuracy to be able to compare between the theoretical and experimental performance. In our experience, the variations in deposition given by the sputter coater are outside our acceptable tolerance range. For that reason, a convenient post-fabrication layer thickness measurement method was implemented. The measurements are based on the transmission spectra of the device (gold-ITO-gold). By measuring the gold layers while fabricating the transducer, it is possible to fit double the measured transmittance spectrum curve of the fabricated transducer to a modelled one (from our optical model) by varying the thickness of the ITO layer.

Thickness measurement of the gold layers is based in their transmission spectra[109]. This is obtained with an ocean optics USB2000+ fibre coupled spectrometer and a conventional light source. Since the transmission of a gold layer changes significantly (70%) over the first 50nm, it is easy to determine the thickness of the layer by comparing

it with the theoretical model presented in section 3.2. The comparison is performed in matlab as explained below (see figure 3.14).

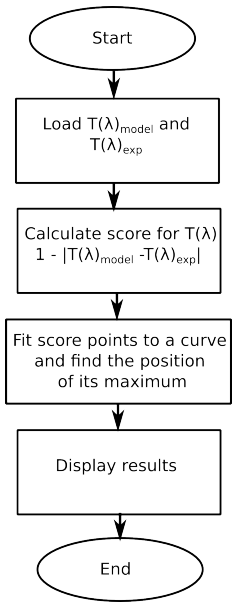

Figure 3.14: Flow diagram of algorithm to calculate H_{Au} based on transmission spectrum $T(\lambda)$ fitting.

Theoretical curves of the gold transmittance $T(\lambda)_{model}$ from 1 to 70nm in 1 nm steps were calculated and saved to a file. A script then loads the experimental trace $T(\lambda)_{exp}$ and fits a curve to compare it with all the theoretical curves (see figure 3.15 top). A score from 0 to 1 is calculated for each theoretical curve according to its similarity with the experimental one (score =1 - $|T(\lambda)_{model} - T(\lambda)_{exp}|$). All the scores are used to build a curve (H_{ITO} vs score), the location of the peak of that curve is then considered the thickness of the layer (see figure 3.15 bottom). Measurements of this process were compared with an external company (see appendix) measurement and with a profilometer measurement having a variation of +/- 2nm from both.

Based on this method, it was possible to measure the thickness of top and bottom gold layers while fabricating a transducer as follows: a number of clean substrates are placed inside of the sputterer chamber. After depositing the bottom gold layer, one

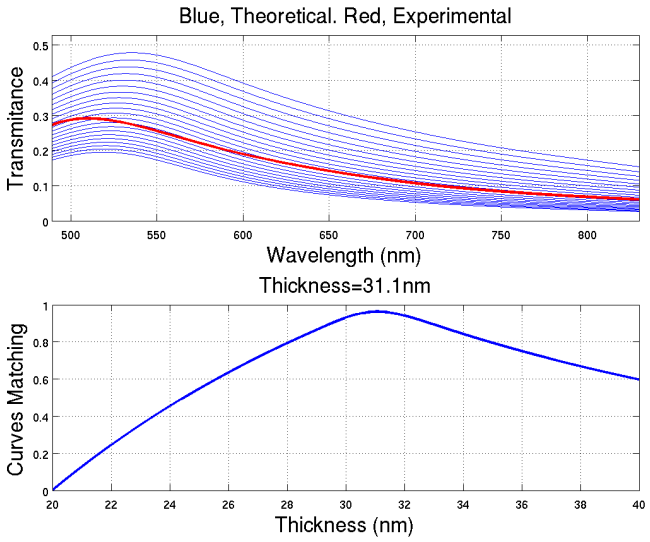

Figure 3.15: Example of the output of the script used to measure thickness of a gold layer. Top, model curves in blue and experimental traces in red. Bottom, comparison between the curves where curve matching equal to one if model and theory are identical. Here the thickness of the ITO layer for the measured device is the one at the peak of the matching curve.

substrate is taken out to perform a gold layer measurement (bottom gold layer). If the layer tolerance does not comply, then the process starts all over again otherwise the sample is returned to add the ITO layer. At this point we can add different ITO thicknesses to each substrate if required. After the ITO layers are deposited, all the devices (which have gold and ITO so far) are placed back into the sputterer including a clean substrate. The clean substrate is used to sample the last gold deposition(to measure its thickness). When the devices are complete (with gold-ITO-gold) and the gold layers measured, the evaluation of the ITO layer thickness is achieved by performing a fit.

Based on the measured thickness values of the top and bottom gold layer, the theoretical transmission curves are calculated (for a range of ITO thicknesses). In this case, the curves need to be calculated each time the matlab script runs because the gold layers thicknesses are slightly different for each deposition. As shown in figure 3.16, theoretical curves for several ITO thicknesses are used to calculate the scores to build a

curve where the maximum corresponds to the measured ITO thickness (using the same method as with the gold layers). At the end of this process, all of the deposited layers have been measured. These resultant thickness of the layers were also used to validate the measurements as the expected optical and mechanical behaviour matched well (see chapter 5).

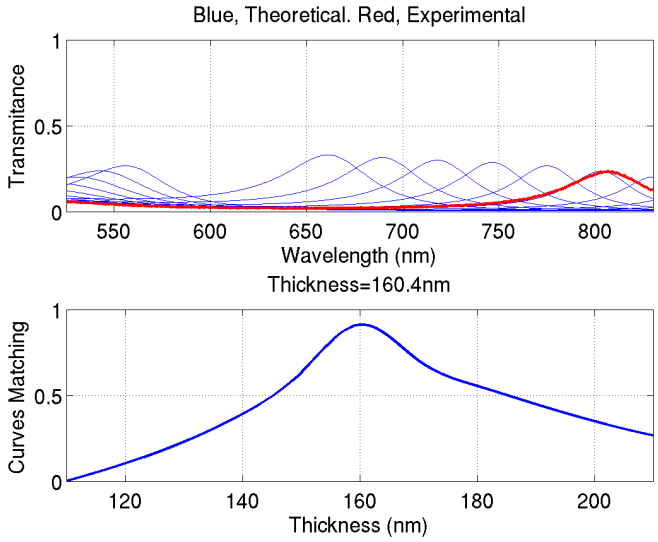

Figure 3.16: Example of the output of script used to measure thickness of ITO layer in a tree layer transducer. Top, model curves in blue at and experiment in red. Bottom, comparison between the curves where curve matching equal to one if model and theory are identical. Here the highest value is related to the thickness

3.6 Summary

The thin film transducer presented here is a three layer structure consisting of gold-ITO-gold. The structure forms an optical resonating cavity similar to a zero order Fabry Perot. When exposed to a short laser pulse, such transducer generates ultrasound by thermoelastic effect, and the generation bandwidth of the transducer has a resonance peak which depends of the layer thicknesses. When the thicknesses of the layers are selected correctly, the reflectivity and transmittance of the transducer is sensitive to

changes of its own height, making it a efficient detector. The transducer can also be used to detect Brillouin scattering when generation and detection occur in the same transducer.

The optical cavity formed by the metal-dielectric-metal configuration allows selection of layer thicknesses for high transmittance. High transmittance allows us to detect Brillouin signal in transmission. This configuration simplifies the detection path, increases SNR and allows to protect a delicate specimen such as biological cells.

Based on optical and mechanical models, transducers with gold layers of 20+/- 5nm and ITO one of 145 +/- 15nm will be optimal for this application.

Chapter 4

Methodologies

4.1 Introduction

In this chapter, the experimental set-up, sample preparation and the signal processing will be presented and explained. These methods are the basis for the experiments presented in chapter 5.

4.2 Experimental set-up

For the experimental se-tup, two 150 femtosecond pulsed lasers at 780nm in an ASOPS configuration (Menlo-system's two c-fibre 780nm, see section 4.3) were used. The probe laser (laser A on figure 4.1) is directed to the objective and the reflection from the transducer is recovered using a polarising beam splitter and a quarter waveplate. A rotable half waveplate is used to control the amount of power injected into the 50x objective (NA=0.55). The reflected light is divided using another polarising beam splitter and half wavelength retarder. Adjusting the retarder, the beam can be split or redirected into two channels. One channel goes straight to the detector and the other is magnified to monitor the focal spot on a camera (figure 4.1 CCD 1).

The pump laser (laser B), is doubled in frequency with a doubling crystal (BBO).

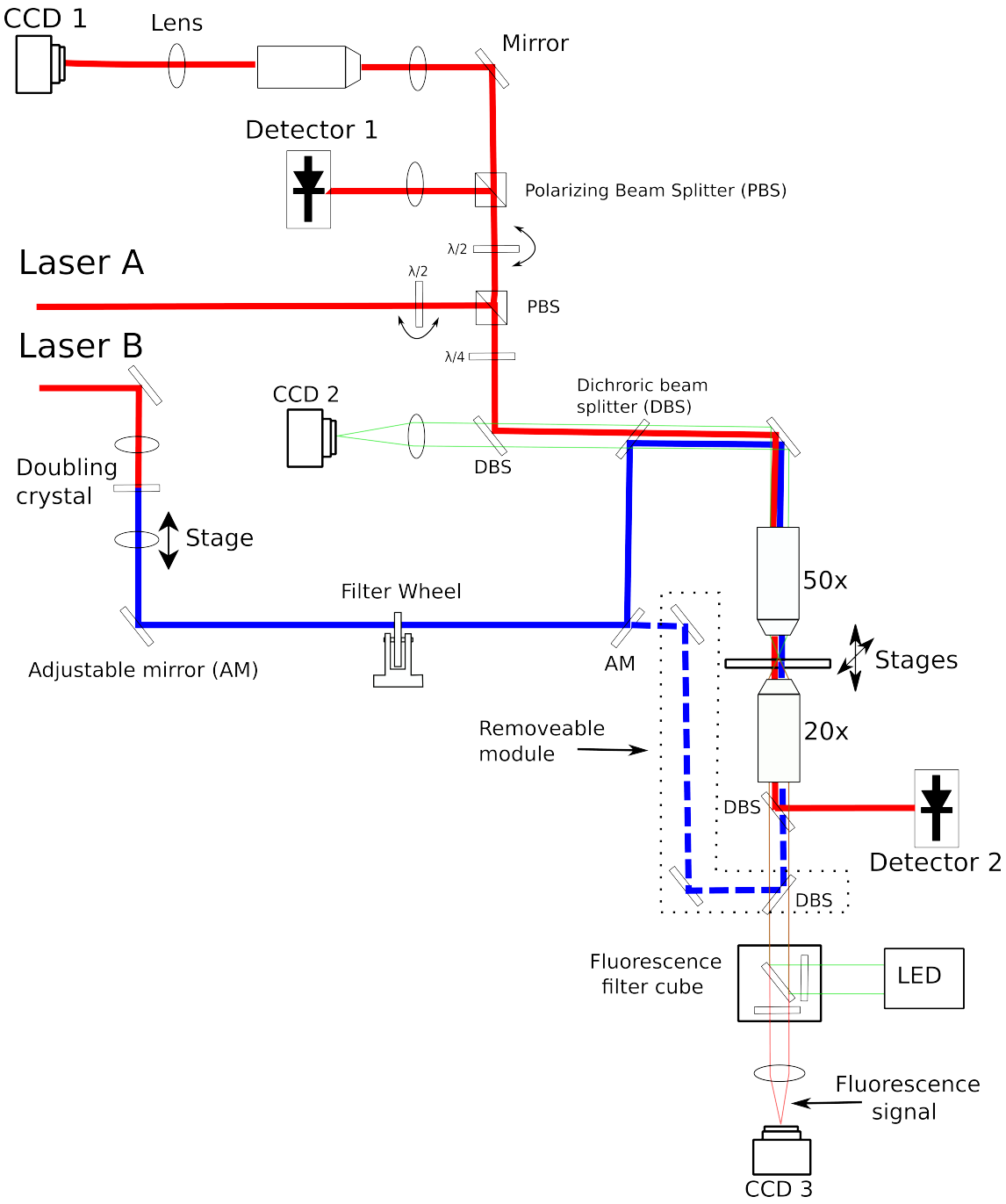

Figure 4.1: Experimental set-up. Two lasers electronically synchronized in an ASOPS configuration. The pump laser is doubled in frequency using a barim borate crystal then it iscombined by a dichroic beam splitter to be focused in to the sample. Alternative paths for pitch-catch detection is marked as doted line and a filter wheel allows to control intensity. The probe laser is combined by a dichroic mirror, focus to the sample through a 50x objective to then be collected (20x objective) and extracted by a dichroic beam splitter. The intensity of the inserted and returned beams are adjusted by the use of polirising beam splitters and waveplates. Optical imaging is performed in CCD2 and CCD3. CCD2 captures a brightfield image and CC3 detects fluorescence signal if applicable. CCD1 is used to monitor shape and quality of the laser spot.

A set of lenses is used to focus the pump beam into the crystal to then collimate it again. The second lens is mounted into a manual stage to allow overlapping of both beams in depth, while the adjustable mirrors allow overlapping in the lateral positions. The inserted pump power is regulated by the use of a filter wheel and neutral density filters. The pump and probe beams are combined using a dichroic mirror. The pump beam can be redirected to allow it to approach the sample through the 20x (NA=0.42) objective to perform pitch-catch measurements (see chapter 6).

The 20x long working distance objective captures the transmitted probe light passing through the sample. The transmitted beam is collected by detector 2 using a dichroic mirror to redirect the light (see figure 4.1). A LED light source is used to illuminate the sample for conventional brightfield imaging on CCD 2 while also serving as excitation light for fluorescence imaging. A filter-cube (optimised for a particular fluorescence label) is used to detect fluorescence signal on CCD 3 (see section1.3.1).

This system was designed specifically to allow the detection of Brillouin oscillations in transmission while performing fluorescence imaging. The wavelengths of the lasers allowed the use of gold for the generation of ultrasound while allowing a wide window for imaging. The characteristics of the dichroic beam splitters were carefully selected to allow this functionality.

4.3 Pump and probe and ASOPS systems

The interest in fast events such as spectroscopic decay has pushed the development of stroboscopic techniques to overcome the bandwidth limitations of photodetectors and electronics[110]. The pump and probe technique is a time resolved stroboscopic technique that addresses this problem and allows one to observe very fast events[72]. In figure 4.2a a simplified schematic of the technique is shown. A pulsed laser beam is split into two parts. A known delay in the path of one of the beams (probe) is introduced by

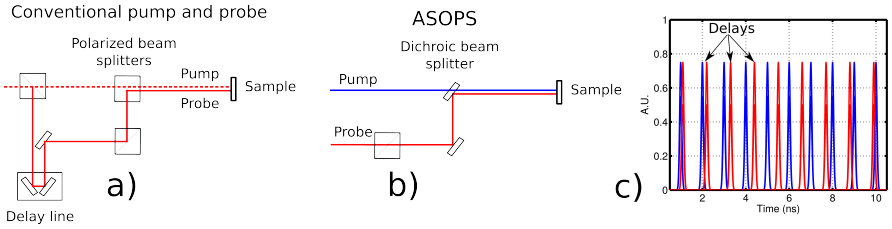

Figure 4.2: Simplified pump and probe set up. (a) Conventional pump probe configuration using a mechanical delay line. (b) ASOPS pump and probe with two pulse lasers instead a the mechanical delay line. (c) Sequence of pulses in time, here see possible to see that the temporal distributions of the pulses is the same for both configurations.

a mechanical delay line. The delay is increased in discrete steps until it reaches one period of the laser pulsing frequency (see figure 4.2c). After each pump pulse, the probe will measure the response at a different delay in time. The full time trace can be built afterwards from all the consecutive measurements. The pump and probe beams are separated using different polarisations, wavelengths or incidence angles to prevent overlapping of the incident and reflected beams.

The use of a mechanical delay line has a main limitation; it restricts the speed of the measurement because it needs to move for each delay position. It can also introduce environmental noise and measurement artefacts. Asynchronous optical sampling (ASOPS) is an alternative to the traditional mechanical delay line used in the pump and probe technique[67]. In such a system, instead of one laser, two pulsed lasers with slightly different repetition rates are used to provide the delay between the pulses (see figure 4.2b). The well controlled phase walk out between the pump and the probe has the same effect as varying the length of the mechanical delay line. The scanning window period is given by the pump laser repetition rate. The difference in frequency between both pulse trains sets the delay rate, which is the time it takes for the process to repeat itself when the cumulative delays equals the period of the pump pulse train.

Figure 4.1 shows a diagram of the pump and probe system used in this work. The arrangement, which is explained in detail in section 4.2, is based on two 780nm pulsed

lasers and control electronics. The lasers have a repetition rate of 100MHz with a delay rate that goes from -10kHz to 10kHz. At 10kHz delay rate, the 10ns measurement window is acquired in 100μs. That means that the signals will be 10000 times slower on the oscilloscope than they actually are. This facilitates detection since conventional photodetectors and amplifiers can be used. This system has the capability to acquire 10k traces in one second. In practice, the detection chain (see section 4.4.1) can only acquire signal produced by a fraction of the pulses. A trade off between acquisition speed, sampling rate and averaging is discussed later in section 4.4.

4.4 Acquisition speed and noise

Speed of acquisition is of relevance in our experiments because long experiments are impractical for living cells; cells move constantly blurring imaging efforts and the amount of time they can survive outside of the incubator in our system is limited. The ASOPS system allows fast acquisition as mentioned in section 4.3. This enables not just faster measurements but also an improvement in SNR; averaging reduces noise by the square root of the averages meaning that 10000 averages will give 100 less noise. However, excessive averaging increases acquisition time. In this section, noise and acquisition speed are evaluated to optimise SNR for practical acquisition times.

4.4.1 Detection chain

The detection chain converts light intensity into an electrical signal to be digitised and stored. The chain consists of two Thorlabs (DET35A) photodetectors with the gain set at 10dB, two minicircuits (ZFL-500LN-BNC) RF amplifiers and a four channel LeCroy oscilloscope (wave runner 104MXi-A) controlled by a PC through a local network (see figure 4.3). The signal from the detectors is split to detect both DC level and AC signal if desired. The AC path is amplified before going to the oscilloscope because of the very

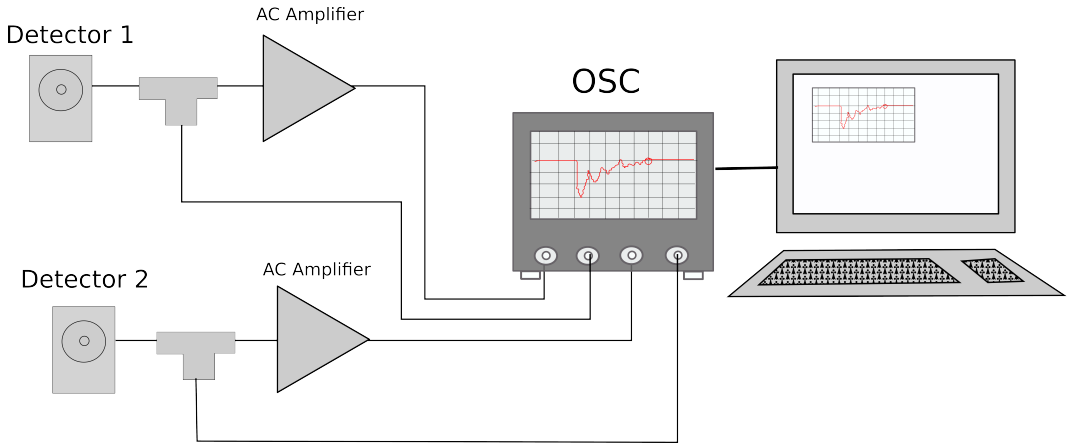

Figure 4.3: Detection chain. Two photodetectors and two amplifiers of the same model are used to sense the intensity of the transmitted and reflected beams. A oscilloscope is used to convert analogue to digital data and a PC controls synchronisation with scanning stages.

small modulation depth typically observed in picosecond ultrasound experiments[64]. The use of a PC allows synchronisation with the scanning stages (PI M-605) to build images through c-scan, a software courtesy of the applied optics group at the University of Nottingham (AOG).

The acquisition system (Lecroy oscilloscope) dismisses trigger signals making inefficient data acquisition. For instance, it processes the acquired data after every trigger signal causing a dead time. During dead time trigger signals are ignored but lasers keep pulsing and exposing the specimens to unnecessary harm. For this reason, the ideal configuration of the acquisition card is investigated in the next section.

4.4.2 Effects of averaging on noise and acquisition speed

Noise and averaging

Using the system described above, simple experiments detecting resonance signals from a transducer in transmission were performed to evaluate SNR against averaging. Figure 4.4a shows the configuration of the experiment. A pump laser is exposed to a transducer and the reflected probe laser is used to measure its resonance. The probe power levels at

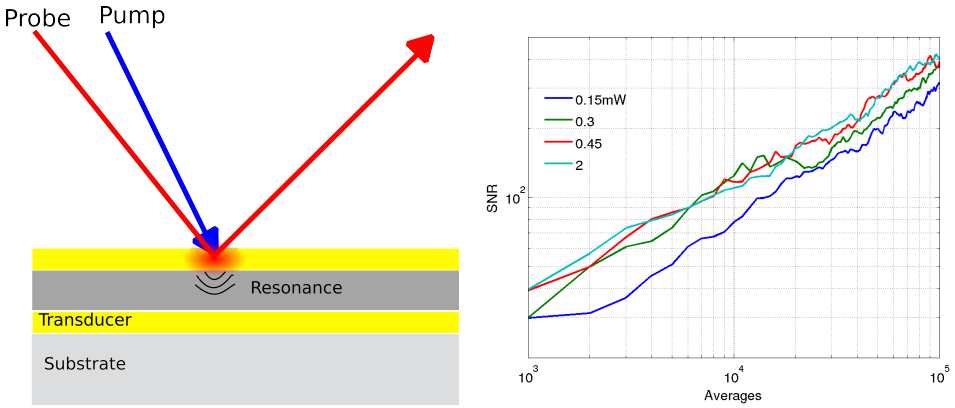

(a) (b)

Figure 4.4: Noise modulation depth (a) and SNR (b) against number of averages and applied power. The legend inside (a) applies for figure (b) as well.

sample were of 0.5mW, 1mW, 1.5mW, and 2.0mW. A hundred traces with 1k averages each were used with 50Ms/s sampling rate on half time window (50μs) and 20GHz bandwidth. Figure 4.5b shows the dependence of the signal to noise ratio (SNR) against number of averages for different probe power levels. As expected, the SNR increases with the square root of the number of averages. It is also possible to see that the obtained SNR for 10k averages is approximately 100. This value depends on many factors such as the pump power (0.4mW), detected power or decay rate of the signals. Some of these parameters depend on each specific transducer substrate (see chapter 3).

The number of averages can be increased for better SNR, however, excessive averaging might reduce acquisition speed. To understand how the acquisition speed is affected, acquisition times were measured, as it is presented in the following section.

Acquisition speed and averaging

In our experiments, fast acquisition speed is a desired feature since it can lead to the reduction in light exposure to a cell, or to increased SNR by averaging. To improve acquisition speed, segmented memory is used. Segmented memory is a built-in acquisi-

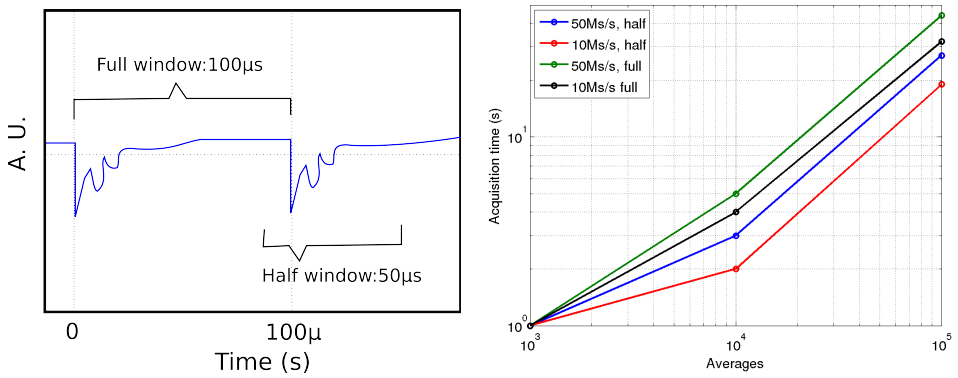

(a) (b)

Figure 4.5: Acquisition time versus number of averages. (a) Representation of full and half window acquisition. (b) Measured acquisition times for different number of averages. Half window (50μs) leaves no information left but increases acquisition speed by a approximately the double.

tion mode that is available in some oscilloscopes. Segmented memory allows to capture data from consecutive triggers in before internal processing takes place. In this mode, the oscilloscope process the information in large portions (number of segments) increasing acquisition speed. An experiment to measure the acquisition times using only the detection chain (see section 4.4.1) and a trigger signal was performed for different number of averages. The settings on the oscilloscope were: a 1000 segments, sampling rates of 10 and 50Ms/s (which correspond to approximately 50 and 250GHz acoustic bandwidth), measuring windows of 100μs (full window, trigger period) and 50μs (half window), and all resources were dedicated to a single channel.

Figure 4.5 shows the result of this experiment. It is possible to see that the acquisition time for a single point goes from a few seconds to nearly half a minute depending on the sampling rate and number of averages.

Based on the information provided in figures 4.4 and 4.5, is possible to establish a trade between noise reduction and acquisition time. This will depend on the number of points, SNR and, in the case of a living cells, the laser exposure levels. For example,

100k averages can give an SNR up to 200, however this would take a few minutes per measurement making imaging a highly time consuming process.

We expect to apply approximately 1mW of probe intensity at sample. At that power level, noise can be reduced significantly with 10k averages which will take approximately two seconds to acquire. For averaging around 10k, the difference in acquisition time between 10 and 50Ms/s is small. However, the larger sampling rate would provide better accuracy measuring the frequency of a given signal. For that reason, averages between 5 and 30k, half window and 50Ms/s were typically used in our experiments.

4.5 Signal processing

For experiments carried out in chapter 5, we have either a single or an array of time traces. Each time trace consists of a rapid drop of signal level (peak) followed by a slow stabilisation. On top of this, there are the signals of interest including: the resonance of the transducer (given by the transducer sensitivity), the Brillouin signal arising from the substrate and the Brillouin signal from the sample (see chapter 5). These three signals have the form of a decaying sinusoidal wave each one with different frequencies, amplitudes, phases and decay rates (see section 5.3).

Each trace is processed in the same manner using the following steps. The trace is truncated around the area of interest, then the thermal background is removed by subtracting a fitted function. After that, a fast Fourier transform is performed and peak frequencies are evaluated. In the case of two dimensional scans, the peak frequencies and amplitudes can be used to build images. Filtering in the time domain is performed for displaying purposes.

4.5.1 Thermal background removal

Absorption of a light pulse leads to rise in temperature in the sample. This change in temperature induces a change in the refractive index which locally affects the reflection and transmission of a given material (see equation 2.8). This leads to a slow change in light level observed in laser ultrasound experiments. We refer to this effect as thermal background.

Since the duration of the thermal background is long in comparison to the period of our acoustic signals, they will be overlapping in time. In order to separate them, the raw trace is cropped and fitted to a polynomial curve (third to sixth order). Then the fitted curve quality is verified by overlapping it with the source trace on a graph (see figure 4.6b). Once we have verified that the fitting follows correctly the source trace, the fitted curve is subtracted from the source one.

The thermal profile versus time at z=0 can be derived from the expression for a single layer as presented by Thomsen *et al*[73](see section 2.2.2). However, to use this expression to remove the thermal contributions from a multilayer structure is a complicated problem given the thickness of the layers and the contributions of the transducer since the beam is detected in transmission. In any case, it is of critical importance to remove all background in order to observe the signal of interest properly. For that reason, a polynomial fit is used instead of a rigorous modelling of this process.

Figure 4.6 shows an example of this process from a signal obtained experimentally. The signal is the resonance of transducer on a polystyrene film. In figure 4.6a, a graph of a raw trace is shown. Figure 4.6b shows the cropped raw trace with the fitted curve on top of it. Figure 4.6c displays the subtracted version where the thermal decay has been removed. Also, in figure 4.6d a filtered version of the thermal-free trace is shown.

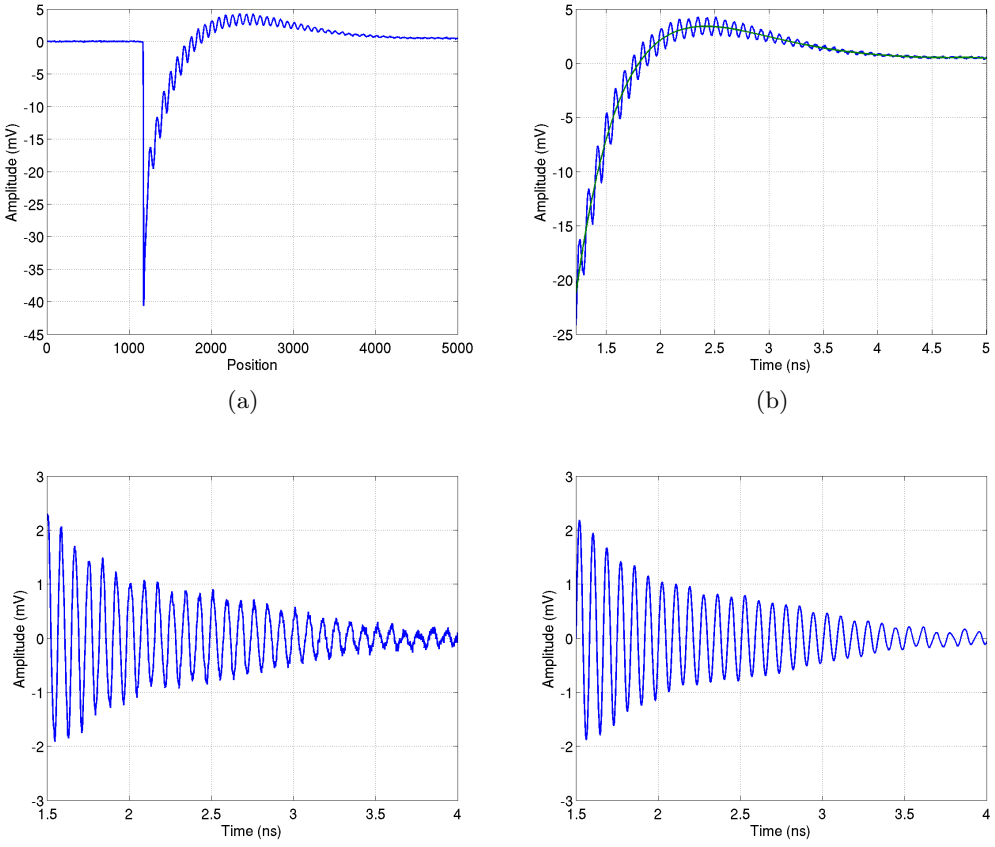

Figure 4.6: Example of thermal removal. (a) Raw data. (b) Data cropped(blue) and thermal fitted (green). (c) Fitted curve subtracted from data to remove thermal. (d) Filtered trace. If necessary, time trace can be shifted to match the pulse arrival.

4.5.2 Evaluation of peak frequencies

By calculating the Fourier transform of a given trace, it is possible to accurately evaluate the frequency of the signal components by observing its peaks. However, doing it many times to build a picture is a time consuming task that will introduce a human error.

To evaluate the frequency of a peak from a trace automatically, a range of expected frequency values and a threshold on the amplitude is set. This range prevents evaluating the wrong peak as (shown in section 5.3) there is more than one signal resulting from a measurement in transmission. Similarly, the threshold prevents evaluating the frequency of a noise peak. Then the maximum value in the desired range is found and correlated to its position in frequency. The Fourier transform of the trace shown on figure 4.6 is shown in figure 4.7. There, the red part of the trace indicates the range where the maximum is searched for and the black line represents the threshold. If the amplitude of the peak found is lower than that set by the threshold (black line), then the found frequency is discarded and the point is considered lost data.

This method being over-simplified, brings a great gain on processing speed. Accuracy on the other hand, will depend on the SNR and sharpness of the peaks. The lower and broader the frequency, the bigger the error because broader peaks are more suseptible to noise (see section 5.4.3).

4.5.3 Evaluation of time of flight

The time of flight, is the time that the Brillouin frequency stays constant before changing at the boundary of an object and its surrounding media. It is an important parameter that allows the calculation of the speed of sound, thickness, optical path and refractive index in certain circumstances as it will be explained in chapters 5 and 6. To be able to measure it, it is necessary to monitor the Brillouin frequency over time to watch for any changes. Two methods are explored to detect such transitions; time Fourier transform (STFT) and zero-crossing analysis (ZCA). The methods have their

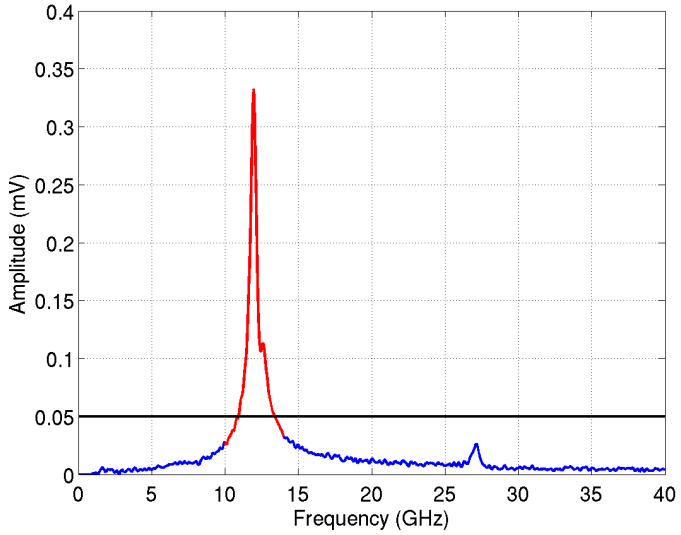

Figure 4.7: Example of peak finding. The blue trace is the original trace where the peak needs to be found. Red indicates range of frequencies to look at, this range is set by the user manually. Black line is the threshold to prevent looking at noise peaks, this value is also set by the user.

own advantages and disadvantages.

Zero-crossing analysis locates the moments in time where the amplitude of a given signal becomes zero. By doing this, it is effectively measuring half period of the signal which leads to the evaluation of its frequency. This method is an effective way to measure the frequency of a sinusoidal wave. It is simple and uses little computational resources. However, noise can affect significantly the estimation of the frequency making it difficult to resolve small changes when a single half period is considered in the measurement.

Short time Fourier transform uses the current peak finding method (presented in section 4.5.2) but performs it on a small section of the experimental trace (short time windows) instead of using the whole length of the signal. If the short time window is taken from different regions of the signal, it allows the determination of the frequency of the signal at different instances of time. This simple method is used to resolve

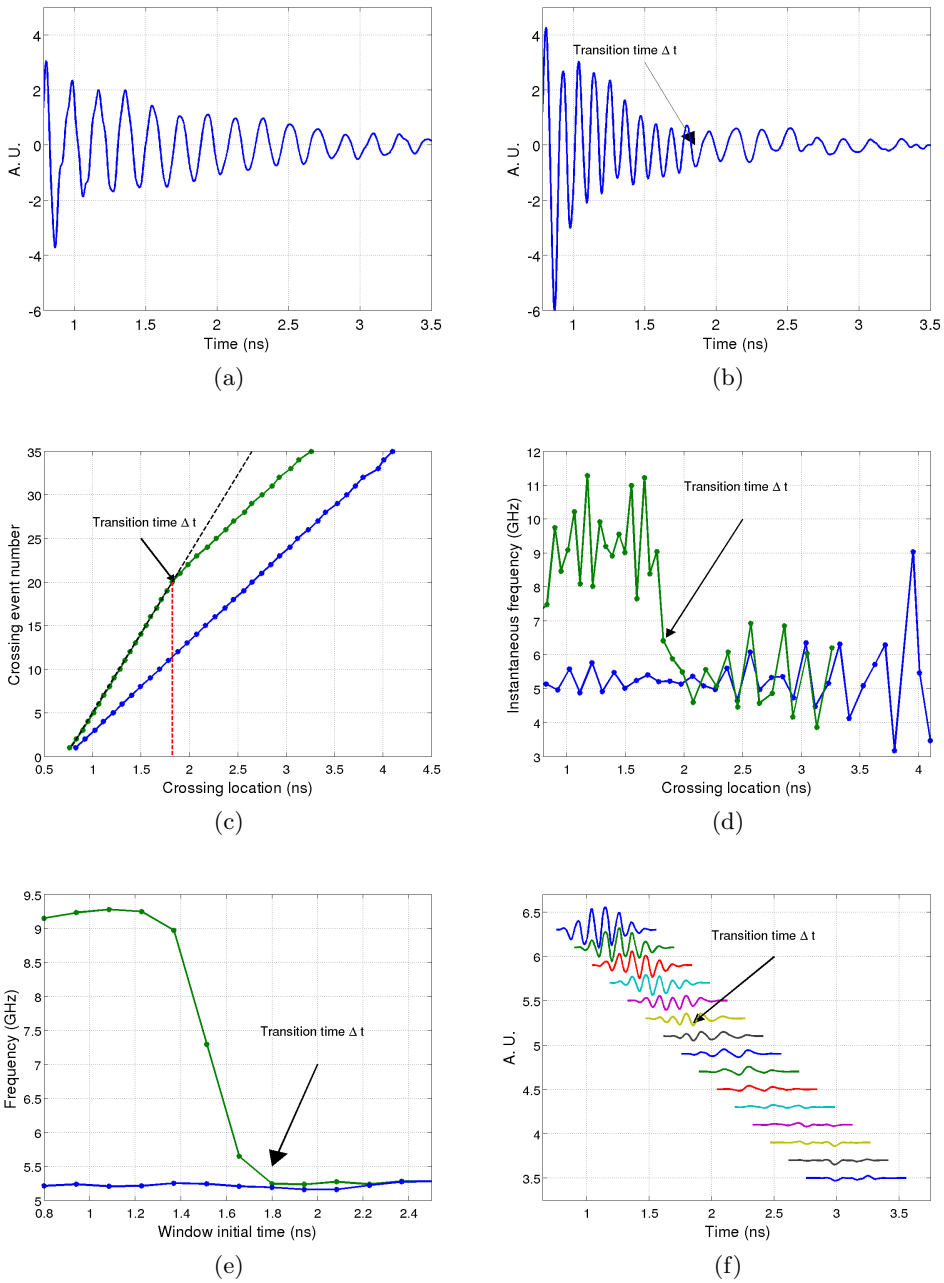

Figure 4.8: Example of signal processing used for time of flight evaluation. (a) Signal with no transition. (b) Signal with transition. (c) Zero crossing times for water (blue) and polystyrene (green). (d) Conversion of the zero crossing times into frequency. (e) Frequency calculated against time using short Fourier transform for water(blue) and polystyrene (green). (f) Traces used in (e) to calculate the peak frequency.

the Brillouin frequency on time and therefore in space. Compared with ZCA, this methods works well with noisy traces because it uses several cycles at a time. However STFT demands larger computational resources and has reduced temporal resolution. Figures 5.14a and 5.14b show two experimental traces, one were the Brillouin signal is composed only by one frequency and another trace where the Brillouin signal is composed by two frequencies occurring at different times (Brillouin scattering from a sound pulse travelling from one medium to another). There is a frequency transition which will be the base to demonstrate both STFT and ZCA.

In figures 5.14c and 5.14d an example of the zero crossing analysis is shown. Figure 5.14c shows the timings for each crossing event for two cases; a trace without transitions (blue curve, in material$_2$) and one with transitions (green, from material$_1$ to material$_2$). The zero crossing time interval remains the same when the frequency does not change producing a straight line. However, for the case where there is a transition (green) the curve is conformed by two straight segments. The ratio of one segment corresponds to material$_1$ (fitted by a black dashed line) and the other one to a material$_2$ (parallel to blue line). The point where the two green lines intersect is then the time of transition between one media and the other ($\sim$1.8ns), marking the time of flight of the acoustic wave inside material$_1$.

The zero crossing times correspond to half a cycle which is converted to frequency as seen on figure 5.14d, The conversion shows high sensitivity to noise which limits the change in frequency that can be detected using this method. For example, in this case the change in frequency is being measured every half cycle. However, if the difference in frequency from one material to another is below 2GHz, probably it will not be possible to be resolved.

For the case of STFT, figure 5.14f shows the short time windows which were derived from the original trace. Each window contains only a few cycles (integer greater than one) and they overlap each other. On figure 5.14e the resultant calculated frequency

against time is shown for a non transition (blue) and transition (green) traces. The frequency of the transition trace ($material_1$,∼9GHz) starts to shift towards ∼5GHz ($material_2$) and reaches this frequency at ∼1.8ns. This method becomes more accurate for smaller time windows, however becomes susceptible to noise.

In both cases, a threshold value is set to determine when the transition takes place which reduces accuracy. On the green traces on figures 5.14d and 5.14e, the measured frequency is compared with a threshold frequency (∼5GHz). When the interrogated value reaches the threshold, the correspondent time position is considered the time of flight. If the transition is reached in the first point, then no transition is considered. This is particularly important when imaging an object ($material_1$) surrounded by media ($material_2$) using Brillouin oscillations where the surrounding areas of the object will show no transition and the frequency of the media is known. There are many other methods to solve this problem such as wavelets or model fitting which might be explored in the future.

4.6 Cell preparation

4.6.1 Phantom cells

In order to optimise the signals and signal processing against an inert, unchanging sample, cellular-scale phantoms were designed and constructed. Phantoms are widely used for simulation and calibration, and they have many advantages over real samples. They are made of well characterised materials, they have a fixed shape and size and do not change or deteriorate like real cells or tissue. In our case, the phantoms serve as a test and calibration target to characterise the response of the system to a homogeneous material of known composition. That allows the comparison of the measured acoustic parameters with those from the literature. There are commercially available materials used specifically for soft tissue phantom fabrication with speeds of sound from 1460-

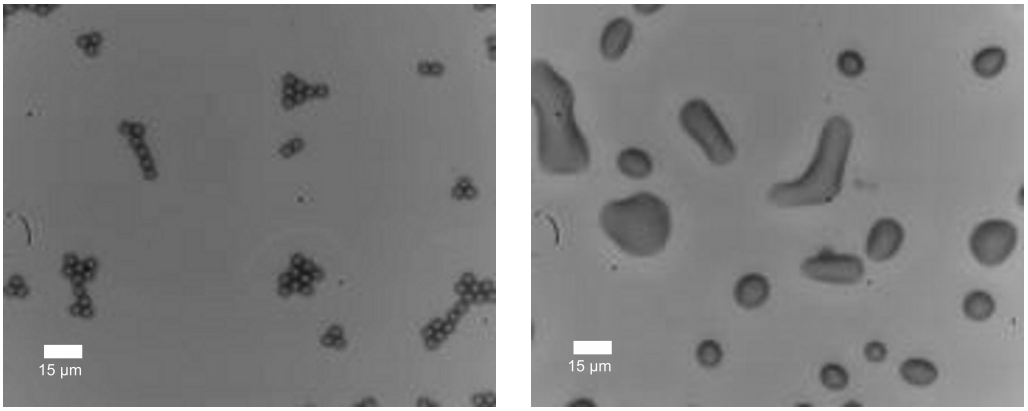

(a) (b)

Figure 4.9: Example of PS phantoms used to simulate the shape and scale of a cell. a), deposited polystyrene 5μ particles. b), particles melted together by heating them at 245^{o}C for 30 to 45 minutes.

1600m/s[111]. However, those are difficult to use in the scale required for the fabrication of phantom cells. Instead, fused polystyrene microspheres were used, with the main disadvantage of having significantly faster speed of sound than water.

The phantom cells were fabricated using 5μm polystyrene spherical particles dispersed across the surface of the transducer and then melting them in an oven at 245^{o}C for 30 to 45 minutes. Figure 4.9 shows an example of these objects before(a) and after(b) the melting process. The melting process helps to create good contact between phantom and transducer, which is essential for good acoustic transmission, as well as immobilising these structures for imaging.

4.6.2 Cultured cells

Cells used in our experiments were cultured in the Institute of Biophysics, Imaging and Optical Science (IBIOS) at the University of Nottingham. The protocol used can be simplified as follows. 3T3 fibroblast cells were obtained from Sigma-Aldrich (UK) and maintained in DMEM:F12 + 2mM glutamine + 10% foetal bovine serum (FBS) at 5% CO_2, 95% relative humidity and 37^{o}C until confluence. Once confluent, cells were

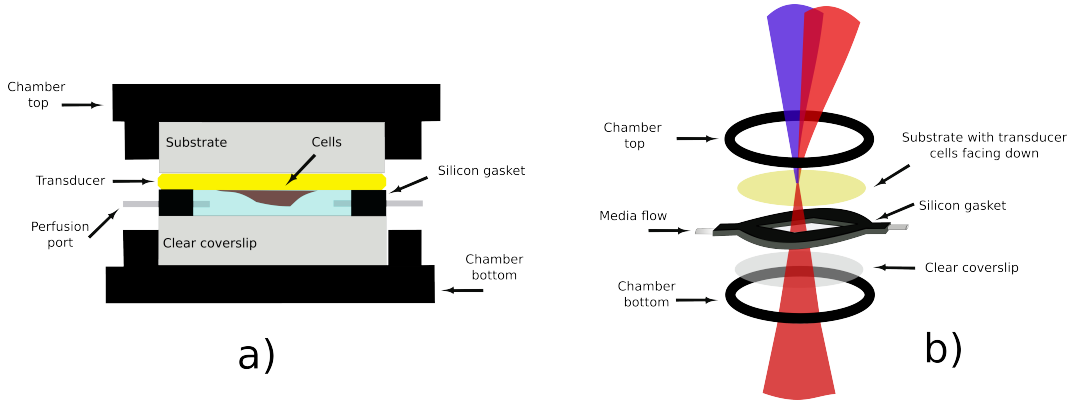

Figure 4.10: Chamber arrangement used to maintain cells under media while performing an experiment. (a) Transversal view. (b) Assembly order and parts.

detached from the flasks using 2.5% trypsin/EDTA. Then they were seeded on pre-treated coverslips with highserum-containing medium at a density of 1x10^{5}cells/mL. Finally they were incubated at 37°C, 5% CO_2, 100% humidity. Before seeding cells, the coverslips where coated with a transducer (gold, ITO and gold) for ultrasonic generation/detection and poly-L-lysin to allow normal attachment and spread of the cells. This layer is thin enough it doesn't affect the result of the measurements.

After 24 hours, or before cell density is too high to observe isolated individual cells, the cells were used to perform experiments while still alive or after being fixed. To fix the cells, they were washed with PBS and immersed in 4% paraformaldehyde for approximately 20 minutes at room temperature (22^{o}C).

A chamber arrangement was used to maintain the cells in media while having a clear aperture to perform the experiments. Figure 4.10 shows the assembly used. The two-coverslip chamber (from Live Cell Instruments Inc.) consists of three parts: top, bottom and gasket with diamond shaped perfusion channel. The top and bottom contain magnets that holds the assembly together and avoids leakage of cell media. The magnets also allow the chamber to be secured to a sample plate. Perfusion ports within the gasket allow the flow of media; in this case with a syringe pump. The gentle flow (5μl/min) of Hanks balanced salts solution (HBSS) supplemented with 4-

(2-hydroxyethyl)-1-piperazineethanesulfonic acid (HEPES, 25mM) as a buffer was used to maintain pH under ambient conditions to keep cells alive for over 5 hours. Having two clear windows, the probe beam can propagate unimpeded towards the capturing lens to be detected.

Chapter 5

Results

5.1 Introduction

A three layer thin-film transducer for the detection of Brillouin oscillations in transmission has been described. How such a configuration can be useful to examine biological cells and the criteria for the transducer design based on a gold-ITO-gold topology has been established. In this chapter, the theoretical and modelled results presented in chapter 3 will be compared with experimental data. A phantom cell is used as a test sample to show system performance and make comparisons, then measurements on fixed and living biological cells are presented. Finally, additional signal processing techniques will be explored to resolve the Brillouin frequency in time to reveal axial detail in the direction of propagation of the strains.

5.2 Model validation

The models introduced in chapter 3 have shown many important characteristics of the transducers for example: the optical transmittance, the reflectivity, the mechanical resonance frequency. Those characteristics are important for design purposes so it is fundamental to validate them against experimental measurements. In this sec-

tion, transducers are fabricated and characterised where their mechanical and optical characteristics are compared with those calculated in chapter 3.

5.2.1 Optical Model

Transmittance for λ_{pump} (780nm) and λ_{probe} (390nm) and sensitivity of λ_{probe} can be evaluated using the optical model presented in section 3.2. The transmittance of a generation transducer is particularly important because it predicts how effective the transducer is at protecting the specimen from exposure to the pump laser light. At the same time, the transmittance of the detection transducer dictates the signal level at the detector.

Transducers with approximately 20nm of gold and different ITO layer thicknesses were fabricated following the methods from chapter 4. The transmittance of the fabricated devices was measured for λ_{probe} and λ_{pump}. Figure 5.1 shows the result of those measurements. There is a good agreement between theoretical curves and experimental data. The transmittance is between 0.15 to 0.30 for λ_{probe} and is 0.05 to 0.1 for λ_{pump}.

The optical spectrum (in transmittance) of a single device, whose ITO layer thickness is unknown, was measured and compared with its modelled counterpart. Figure 5.2 shows the evaluated transmitted spectrum of a transducer with gold layers of 20nm and ITO layers of 110, 120... 160nm (blue curves) and a experimental measurement. The experimental trace fits well to 160nm thickness of the ITO layer. This value (see section 3.5.1) is used in the mechanical models to calculate the resonance frequency.

The optical models also predict the sensitivity of the devices (δR/δH, δR/δH for the reflectivity and transmittance cases respectively) which dictates the strength of the response (δR, δT) given a variation of H_{ITO} (δH). To obtain a modelled response it is necessary to integrate the optical and mechanical models since the sensitivity (δR/δH) and variation of H_{ITO} (δH) can not be measured directly (see section 5.2.3).

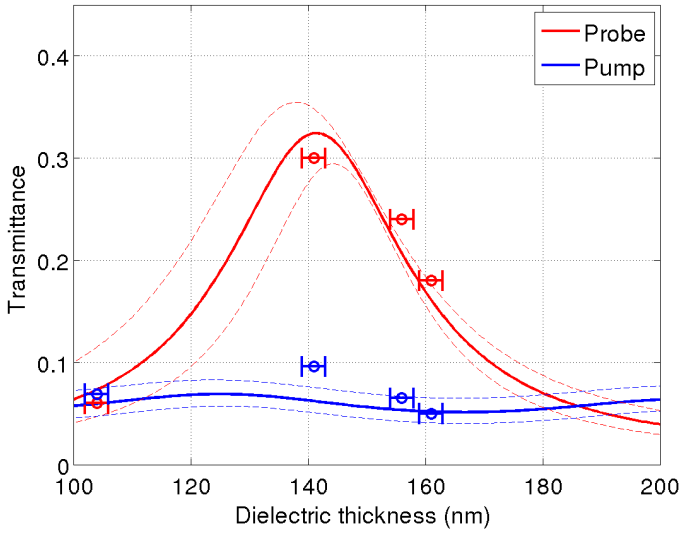

Figure 5.1: Transmission of light through the transducer at λ_{pump}(blue) and λ_{probe}(red) for devices with layer thickness of approximately 20nm of gold and 100-160nm of ITO. Solid lines represent theoretical calculations and dotted ones deviation for an expected error of -/+ 2nm on gold layer thickness evaluation. Circles represent experimental results taken from samples made by sputter-coating layers. The horizontal error bars represent thickness evaluation error on the ITO layer.

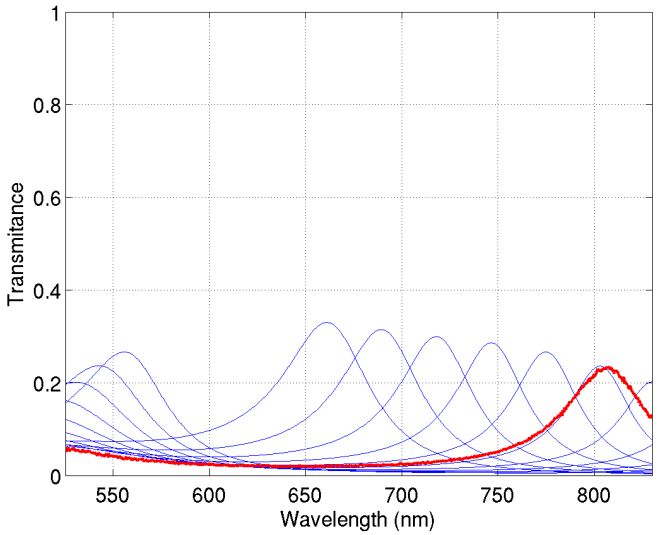

Figure 5.2: Example of transmittance comparison between model(blue) and experiment(red). The blue traces represent different ITO layers (110, 120 .. 160nm). The experimental trace fits well to a 160nm layer of ITO.

5.2.2 Mechanical Model

The mechanical model of the transducer presented in chapter 3 was applied to predict the resonance frequency of the transducers depending on their layer thickness. To validate those results, the experiments were performed in reflection rather than transmission for a practical reason; there is greater sensitivity to the resonance for the reflectivity case compared to the transmission case (see figure 3.5). Higher sensitivity means larger signals and increased SNR which facilitates measurement. Devices with ∼30nm thickness of the gold layer where fabricated aiming for high sensitivity on the reflectivity case. The devices had different ITO layer thicknesses (ITO=100,105,115,130,140,153,160,180nm).

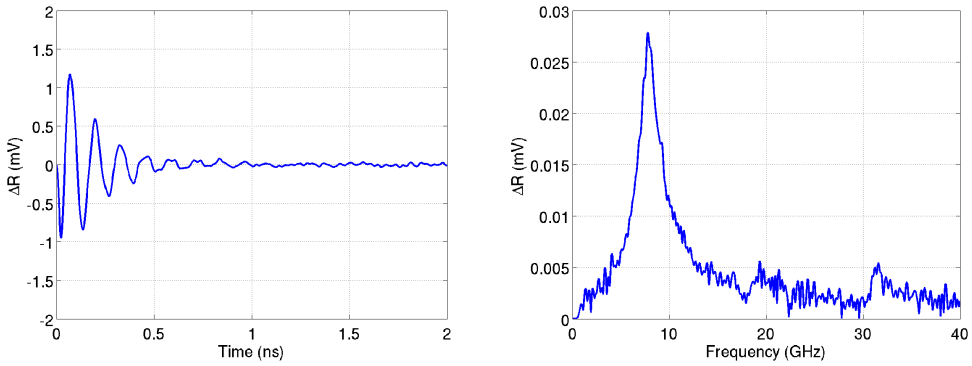

(a) (b)

Figure 5.3: Experimental trace of device with 30nm gold layers and 160nm ITO layer (a) and its Fourier transform (b).

An example of a simulation of δH_{ITO} was shown in figure 3.9. Using the experimental set-up shown in section 4.2, a measurement of the instantaneous reflectivity change induced by the soundwave created in the transducer was acquired for the ∼30-160-30nm device. The resultant experimental trace is shown in figure 5.3. The mechanical fundamental resonance frequency match well ot its simulated counterpart. However, the harmonics are harder to compare due noise (see figure 3.9). This is a validation of the mechanical model which shows that is possible to predict the resonance frequency

of a device based on the known dimension of its layers.

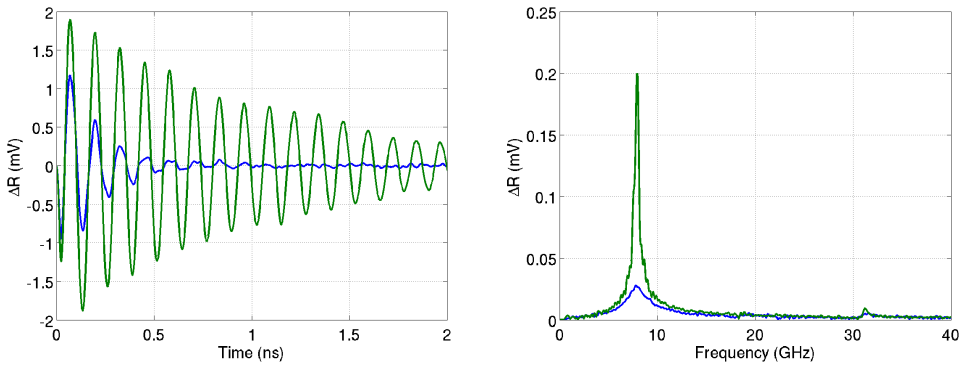

(a) (b)

Figure 5.4: Comparison between experimental traces of a 30-160-30nm device with (green) and without (blue) a polystyrene insulation layer (a). Fourier transforms of both traces (b).

Adding a polystyrene layer between the transducer and the glass substrate, mechanically insulates the transducer from the substrate allowing a much lower decay rate. The long lasting wave provides a more accurate way of measuring the resonance frequency due to the increased number of cycles. Figure 5.4 shows experimental traces the same transducer with and without the polystyrene layer. The amplitude and width of the Fourier peak is significantly improved.

The resonant frequency for devices with different ITO layer thickness ((ITO= 130,140,153,160nm) was measured. Figure 5.5 shows the expected resonance frequency calculated from the FEM model against ITO thickness(continuous line) and its experimental counterpart(circles). The match between the experimental and model results is good.

5.2.3 Integrated optical and mechanical models

The theoretical transmission of the devices can be directly validated using only optical measurements. Similarly, the modelled resonance frequency can be validated by ob-

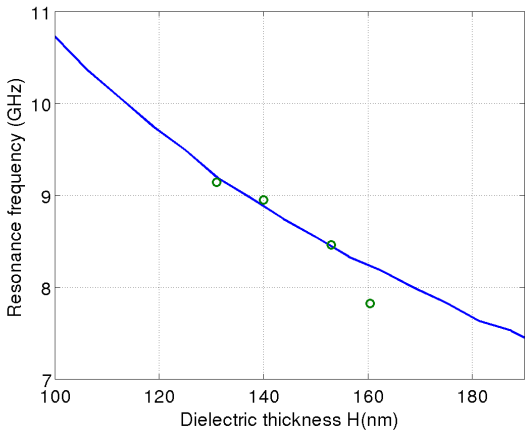

Figure 5.5: Comparison of the resonance frequency obtained for theoretical(line) and experimental (circles) results, for devices with ∼30nm of gold.

serving the variations in reflectivity of the transducer induced by the generated wave. For the case of the sensitivity (δR/δH, obtained from the optical model) and of the change in ITO thickness δH_{ITO} (obtained from the FE model), an approximated expected modelled response (ΔR) was obtained. That response for the reflection case can be calculated as:

$$\Delta R = \frac{\delta R}{\delta H} \delta H_{ITO} \tag{5.1}$$

If this response is normalised by the static reflectivity value (DC), it gives the opportunity to directly compare theoretical modulation depth (ΔR/R) with the experimental one (ΔV/V). Figure 5.6 shows an example of this comparison. There is a very good agreement between the modelled and measured variations in amplitude.

Similar experiments were performed for a series of devices with different ITO thicknesses (the devices used in section 5.2.2). According to their layer thicknesses, the devices are shown as dots in figure 5.7a. Each device was excited by a laser pulse with the same energy (roughly matched to the one used in the mechanical model) and their response was detected in reflection. This comparison assumes that the only parameter

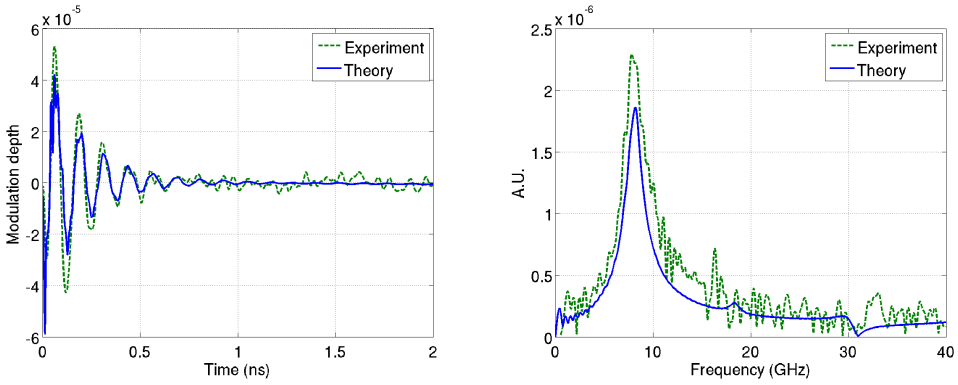

(a) (b)

Figure 5.6: Comparison between experimental(green, $\Delta V/V$) and simulated(blue, $\delta R_{model}/R_{model}$) modulation depth response of a 30-160-30nm transducer to a single pump pulse. (a) Temporal response. (b) Corresponding spectra.

changing in the experiment is the ITO thickness. The modelled modulation depth was obtained directly from the optical models. The results are shown in figure 5.7b and the match is good considering multiple source of error like variations in the gold layer thickness from different sputtering cycles, laser spot overlapping offset and changes in focus. This is another confirmation that the model provides the means to predict the devices performance before it is used.

5.2.4 Brillouin signal amplitude

Brillouin oscillations is the preferred detection mechanism and the frequencies expected for a cell are between 5 and 6 GHz (at λ_{probe}=780nm). The model presented in chapter 3 is used to roughly predict the relative change in amplitude of the Brillouin frequency (at 5.5 GHz, see figure 3.11) for the range of devices presented in this work (see section 3.3). It is expected that the Brillouin signal will be increased as the transducer generates greater amplitude at the Brillouin frequency. In other words, it is expected to boost the Brillouin signal amplitude when the Brillouin frequency and the resonance of the transducer coincide. It is difficult to validate this effect for the case of the de-

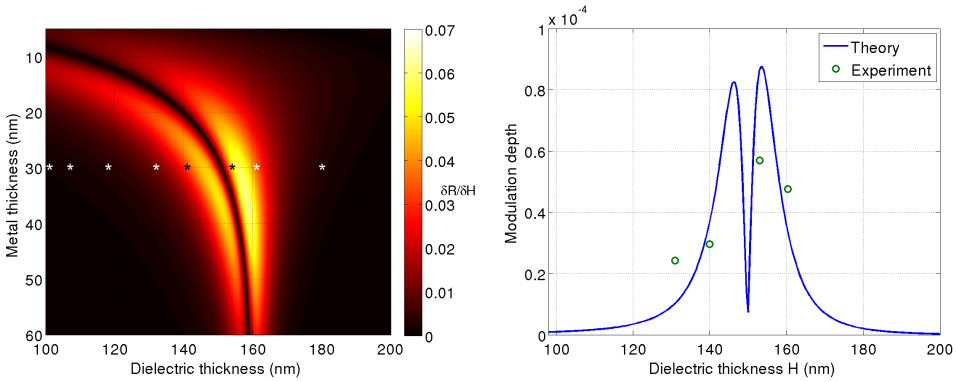

(a) (b)

Figure 5.7: Peak modulation depth $\Delta R/R$ comparison vs ITO thickness. Dimensions of devices shown as stars on top of the sensitivity graph (a). Amplitude of the normalised response of experimental devices (green) compared to model(ΔH=0.6pm) for gold layers of 30nm (blue) (b). Devices with lower sensitivity can not be characterised as their signals are not detectable.

tection transducers in water or cell media for a practical reason; when detecting in transmission, the levels at the detector change dramatically with gold layer thickness which makes difficult to reach 5.5GHz without blocking completely the probe light at the detector. Additionally, having to tune the resonance frequency at 5.5GHz is necessary to deposit the layers with very accurate thicknesses which is challenging using our current fabrication methods. Instead of using three layer transducers, a single gold film on glass was used to verify that the amplitude of the Brillouin signal increases when the generated amplitude at a particular acoustic frequency is incremented. Detecting in transmission and using single gold layer transducers, the variation of the reflectivity is very small as its thickness increases. This allows us to change the generated acoustic bandwidth and resonance frequency to be changed while keeping other parameters fixed.

Figure 5.8 shows the change in amplitude of the Brillouin signal measured on glass for gold layer thicknesses from ~40nm to 120nm. The amplitude (at 22GHz, Brillouin frequency on glass) increases when the resonance frequency of the device sweeps across

22GHz. The amplitudes are normalised to their maximums and their shapes match well.

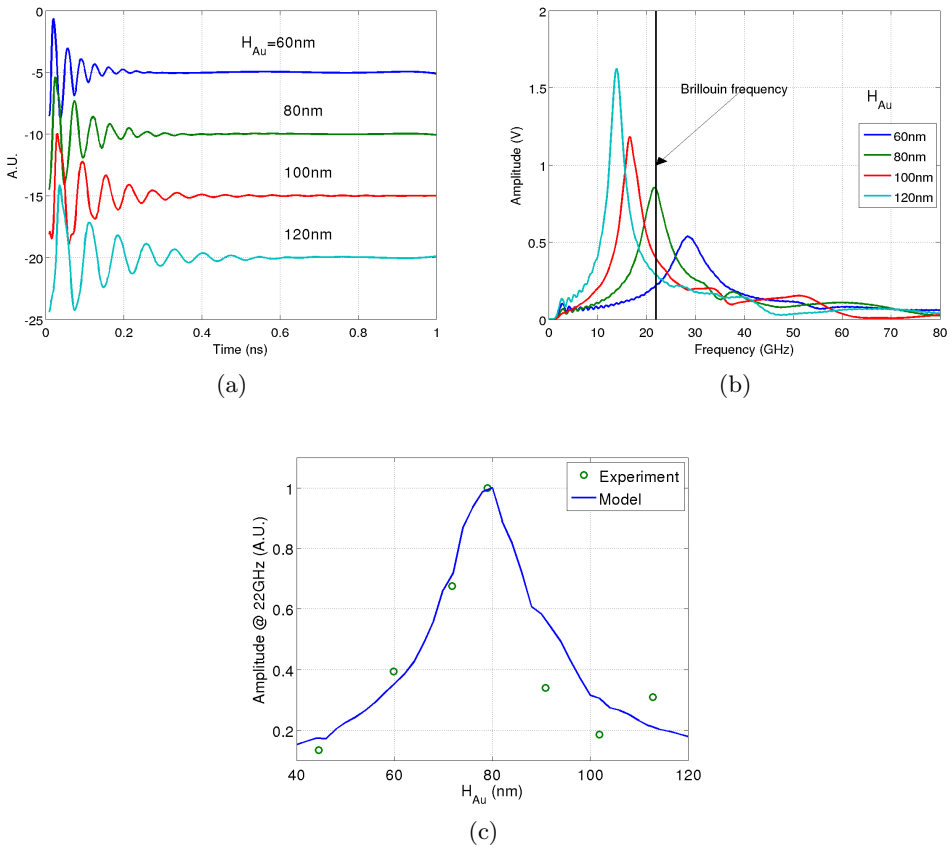

Figure 5.8: Amplitude variation comparison between FEM simulation against Brillouin amplitude of a single gold layer transducer for several thicknesses. (a) Simulated mechanical motion in z axis of the gold layer for different gold thicknesses. (b) Fourier transform of sample traces shown in (a). (c) Comparison of simulated peak amplitudes (blue lines) against measurements of the peak amplitude of the Brillouin signal (green circles). The amplitudes are normalised to allow comparison of the amplitude variation. The simulation match well the variation of the experimental results indicating the increase in amplitude due to the resonance.

These results suggest that the models predict accurately the resonance frequencies of the transducers (single or multilayer). In addition, they show that the amplitude of the Brillouin signal is not only influenced by the intensity of the pump pulse, but also by the resonance frequency of a given device.

5.3 Brillouin detection in transmission

In Chapter 3 detection of Brillouin oscillations in transmission was proposed. This mode of detection offers the opportunity to greatly reduce the exposure of laser light to the sample while keeping the setup simple and detection light levels high. In this arrangement, both lasers are focused to the sample through the same objective lens which facilitates laser spot overlapping and ensures good SNR. There are however some disadvantages to this approach: namely lower modulation depth compared to the conventional reflection detection case and the detection of a second Brillouin signal from the glass substrate.

Reducing laser exposure by detecting in transmission is fundamental for the goals of this work since it gives the opportunity to expand single point measurements into two dimensional scans on living cells. The conditions in which this approach is possible were analysed based on optical and mechanical models. chapter 3 concluded that devices with 20-140-20nm of gold-ITO-gold are ideal for this approach.

To test the approach, water was selected as a sample, due to its similarity in properties to the cell media. A water film was created between the substrate and a coverslip to prevent distortion of the laser beam at the water/air interface. The substrate with the transducer deposited on it was placed with the uncoated side facing both lasers. The sound wave travelling through the water film scatters light which interferes with the directly transmitted light (see figure 2.10).

Figure 5.9 shows a sample trace and its FFT acquired with the set-up presented in section 4.2. Three signals are present in the time trace: two long lived Brillouin signals seen as sharp peaks in the FFT, one from the glass substrate (∼22GHz), one from the water film (∼5GHz), and a third signal from the device resonance. The later decays considerably faster than the Brillouin signals, which leaves the option to crop the time trace and measure the Brillouin frequency from the remainder of the trace.

The SNR(∼60) seen in the sample trace indicates the approach is viable, measuring approximately 7μm into the water. However, to demonstrate contrast with the presence of an object with different mechanical properties a phantom cell will be measured.

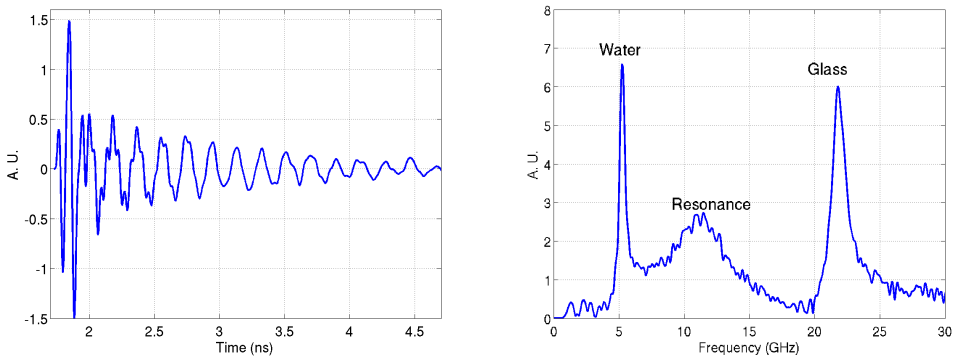

(a) (b)

Figure 5.9: Example of experimental trace of a picosecond ultrasound experiment in water using a 20-140-20 transducer in transmission. a) Shows the time trace itself and b) its Fourier transform where the three frequency components detected are clearly visible; the signal of interest (∼5GHz), the transducer resonance (∼11GHz) and the Brillouin oscillation from the glass substrate (∼22GHz)

5.4 Cell imaging

This section builds on all the results so far to apply the approach proposed in this work to image different samples, starting with phantoms, followed by fixed and finally living cells. Additionally, the obtained images are analysed using zero-crossing and short time Fourier transform processing methods to extract depth information along the axis of acoustic propagation.

5.4.1 Phantom Cells

In this case we will use a phantom cell as described in section 4.6.1. Phantoms are synthetic representations of real objects or tissue. The purposes of building a phantom vary according to the application[111]. Phantoms will be used here as test samples using

a well known material (polystyrene). By doing so, it will be possible to compare the speed of sound measurement obtained with our method against that from the literature as well to observe contrast with the surrounding media. Phantoms were fabricated on ∼20-140-20nm gold-ITO-gold transducers.

The presence of cell media is simulated by submerging the phantom in water. This also gives a background reference for contrast. The sample was mounted in a sealed chamber filled with water for transmission detection(see figure 2.10). Figure 5.10 shows a sample trace from a single point on the phantom. A transition of the Brillouin frequency at the phantom-water boundary is clearly observable. This transition is due to the different speed of sound and refractive index of the two materials. The measured Brillouin frequencies of the phantom and water at λ_{probe} are 9.0 and 5.2GHz respectively. The large difference in frequency makes the transition easy to see, however in the case of a real cell the frequency contrast is expected to be much smaller[65].

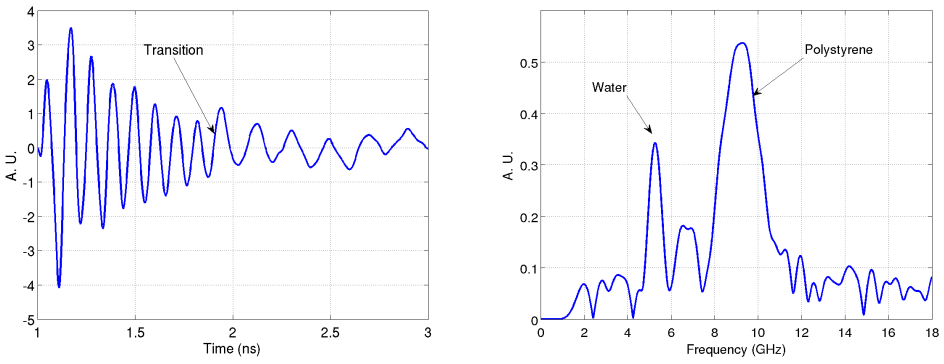

(a) (b)

Figure 5.10: Example of transition from polystyrene to water. When the soundwave leaves the polystyrene and enters the water there is a change of Brillouin frequency due to change in refractive index and speed of sound.

Figure 5.11 shows the result of a scan over a phantom cell. For each point on the scan, two time traces of the transmitted and reflected beams were acquired and processed to measure their Brillouin and transducer resonance frequencies (see section

4.5). The scan was a 30x30μm with 1μm steps. The 900 points were acquired in approximately four hours, taking 15000 averages per point. The need to detect multiple channels simultaneously has a considerable penalty to the acquisition speed since our current acquisition system optimizes its memory to acquire a single channel. If a second channel is acquiered, the memory usage is split affecting its hability to process information rapidly.

In figure 5.11a there is an optical picture of the scanned phantom. Here it is still possible to see the shape of the spherical particles used to build it. In 5.11b the Brillouin map obtained from that picture is shown. The correlation between the optical picture and the acoustic one is good. The contrast is high and the variation of the Brillouin frequency is small(+/- 7MHz), suggesting good homogeneity. The average SNR was $\sim$70 for the water and 57 for the phantom. In figure 5.11c there is a map of the refractive index assigned according to its Brillouin frequency; refractive index from water if the Brillouin frequency its $\sim$5GHz and of polystyrene if it is $\sim$9GHz.

If the refractive index of the phantom is constant, its Brillouin map is directly proportional to the speed of sound. Taking polystyrene refractive index as 1.58 at λ_{probe} [112], and applying equation 2.13, a speed of sound of 2221 +/- 2m/s was calculated (see figure 5.11d). These results are similar to the bulk speed of 2407m/s reported by Smith [113]. Refractive index in polystyrene has a strong dependence on film thickness so it can be expected for the phantoms to have a slightly different refractive index than the spherical particles used to make them [112]. Additionally, it is possible that there is a dependence of the speed of sound to the acoustic wavelength.

Simultaneously, the reflected beam was also acquired. Although the Brillouin and resonance signals are present on both the reflected and transmitted signals, their amplitudes are considerably different. The Brillouin signal is stronger in transmission and the resonance signal stronger in reflection. The measurement of the reflected signal gives the opportunity to monitor the resonance frequency of the transducer to observe

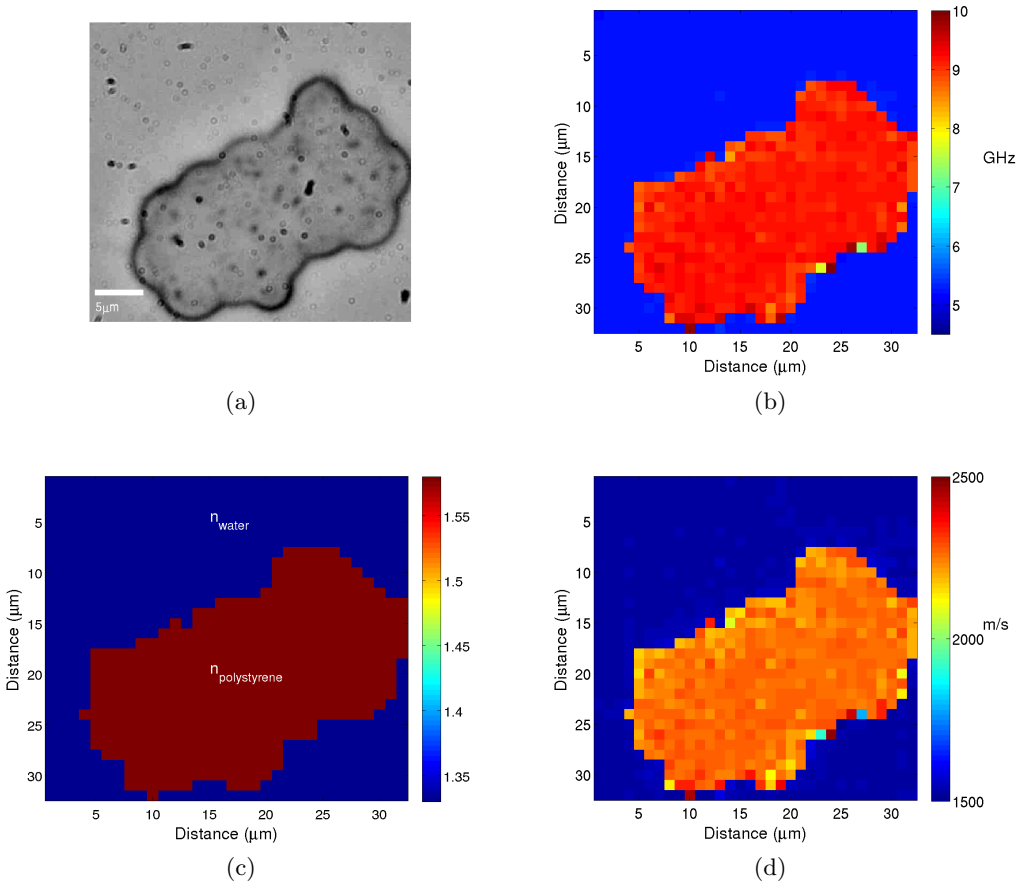

Figure 5.11: Scan over a phantom cell in water. a) Optical picture. b) Brillouin image of the phantom cell. c) Refractive index map of the scanned area. d) Speed of sound map of the scanned area.

the effect of the phantom on the transducer response. This measurement gives an idea of the acoustic characteristics at the transducer/phantom interface which are difficult to observe by monitoring the Brillouin frequency. Similar methods of detection have been used as mass sensors, as well as for protein[88] and cell imaging[99].

Figure 5.12 shows the resonance frequency measured from the reflected beam for the phantom cell presented in figure 5.11. The resonance frequency of the transducer changes clearly from outside the water to the phantom and excibits a SNR of ∼50. Inside the phantom it is possible to see changes in the resonance frequency which

correlate well with the polystyrene beads used to make the phantom (see figure 5.11a). These features are not visible on the Brillouin map of the same phantom (see figure 5.11) probably because those are constrained to the near vicinities of the transducer where the Brillouin frequency is difficult to evaluate. The origin of these frequency changes is possibly due to air trapped between beads when were fabricated. However, these frequency shifts are not well understood and need to be further investigated.

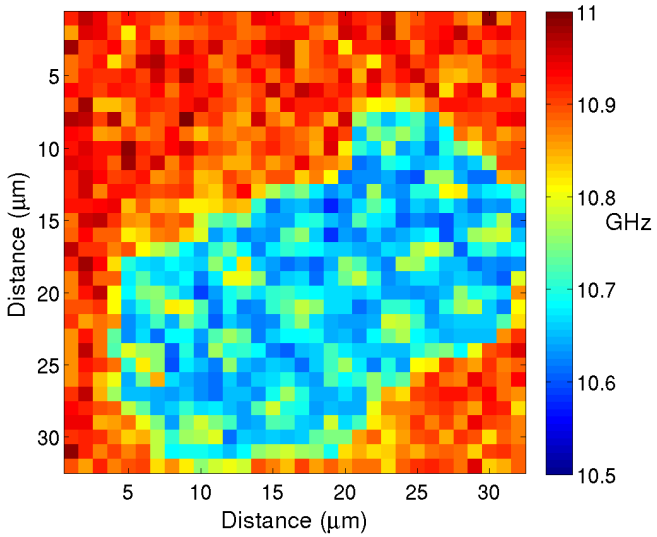

Figure 5.12: Resonance frequency of a transducer measured over a phantom cell in water. The constrast mechanism is related to the damping effect of the phantom over the transducer resonance.

When the soundwave is travelling from polystyrene to water, the Brillouin frequency we observe changes due to the different speed of sound and refractive index of each medium. If the surrounding media has known characteristics, a known reference Brillouin frequency will be available to determine the time of flight of the wave inside the phantom. If we know the refractive index of the specimen and the Brillouin frequency from the traces themselves, then the thickness of the object will be given by:

$$h = \frac{\delta t f_B \lambda_{probe}}{2n} \tag{5.2}$$

where δt is the transition time in the media, f_B is the Brillouin frequency, λ_{probe} is the laser wavelength and n the refractive index of the specimen. Figure 5.13a shows a b-scan of the phantom cell presented in figure 5.11. The different transition times for along the scan shows a rounded shape which is the expected profile of the phantom. From there we can observe a delay of approximately 2ns which leads to a calculation of the thickness of approximately of 4μm (equation 5.2). The time of flight for each point was calculated using zero crossing analysis presented in chapter 4. Applying this method, a map of the height of the phantom was calculated as shown in figure 5.13b. The background of the map is not zero due to limitations of our zero-crossing method. Where the initial part of the trace was cropped so only one frequency component was present.

However, the height of the phantom is measurable and the obtained result is ~20% under the 5μm nominal size of the polystyrene used to build the phantoms. Since the particles where partially melted using temperature close to the polystyrene melting point this result is reasonable. This measurement needs to be validated through other methods such as an atomic force microscope or a profilometer.

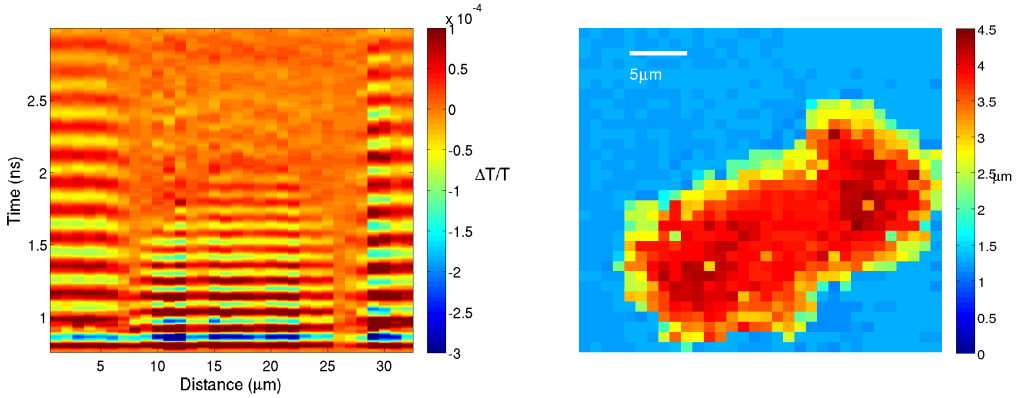

(a) (b)

Figure 5.13: Bscan and profile from phantom cell presented in figure 5.11.a) Bscan across the phantom where the profile of the phantom is visible from the difference in frequency of the signals. b) Profile of the same phantom obtained by zero-crossing analysis.

5.4.2 Depth resolution

In a Brillouin oscillation measurement, the sound propagates away from the generation point along the z-axis. As it does so, it scatters light from different spatial position in the material. If the refractive index is known, then it can be possible to convert the spatial axis into temporal axis. From equation 2.13 is possible to calculate the speed of sound if the refractive index is known:

$$\nu = \frac{\lambda_{probe} f_B}{2n} \tag{5.3}$$

allowing to convert temporal axis in spatial axis as:

$$z = t\nu \tag{5.4}$$

which allows the estimation not only of the thickness of the object but also of features along the z axis. Using zero crossing analysis it is possible to sample the frequency every half micron, However this is very sensitive to noise and can only work with large changes in Brillouin frequency. Since cells present contrast of the Brillouin frequency in the hundreds of mega hertz, short time Fourier transforms (STFT) are use instead.

Using STFT is possible to resolve the Brillouin frequency in z with resolution given by the acoustic wavelength. However, to have maximum resolution a single period of the Brillouin frequency is to be used. This means that measurements can be highly susceptible to noise.

To asses the axial resolution and the effect that noise has on STFT, a sample was fabricated to have a sharp edge. This edge will be used to measure the frequency transition of such edge obtained by using short Fourier transform windows. The edge was fabricated by coating a transducer with a 3μm layer of polystyrene which was immersed in water (detecting in transmission). The Brillouin frequencies from water (5.2GHz) and polystyrene (9.15GHz) provides a sharp change in frequency happening

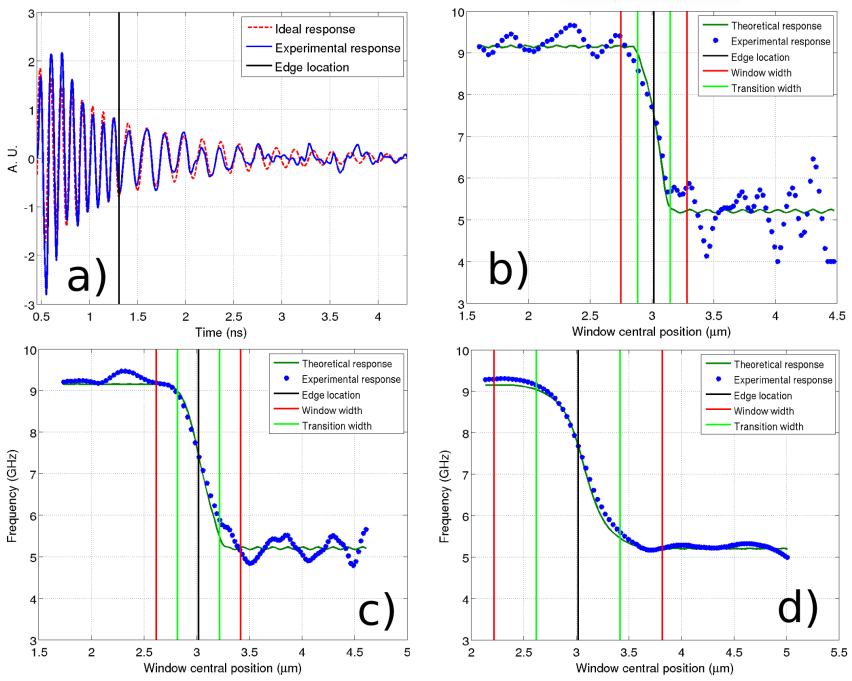

Figure 5.14: Example of signal processing used for sectioning where a transition in frequency marks the change between two materials. (a) Experimental and ideal traces with a sharp edge made out of polystyrene-water transition. (b) Processing of the data with two cycles window and one acoustic wavelength resolution (270nm). (c) Processing of the data with three cycles window and one and a half acoustic wavelength resolution (400nm). (d) Processing of the data with six cycles window and three acoustic wavelength resolution (800nm).

in a small volume.

Figure 5.14 shows an example of the response to a sharp edge from the time-resolved signals using short time Fourier transforms. Figure 5.14a shows the measured (blue) and ideal (red, dashed) traces from a sample with an edge between polystyrene (f_B=9.1GHz) and water (f_B=5.2GHz). The ideal trace ($S(t)$) is a noiseless representation of the experimental time-resolved signal with the form:

$$S(t) = A_1 sin(2\pi f_{B1} t) e^{-\alpha_{a1} t} \tag{5.5}$$

for $t = 0$ to $t = \Delta t$ and

$$S(t) = A_2 sin(2\pi f_{B2} t) e^{-\alpha_{a2} t} \tag{5.6}$$

from $t = \Delta t$ to $t = \infty$ where Δt is the edge location in time, A the amplitude of the wave, f the Brillouin frequency and α the acoustic attenuation coefficient for materials 1 (polystyrene) and 2 (water).

Figures 5.14b-d shows the determined frequency vs position in space for a real (blue stars), an ideal (continuous green) time resolved Brillouin signals and the position of the transition (black vertical line). Figure 5.14b shows the transition measured for a window lasting two acoustic cycles. The transition happens within half a window which in this case represents maximum resolution (λ_a=270nm in polystyrene). However, the Brillouin frequency before and after the transition presents large variations. Figure 5.14c, shows the resolution given by using a time window of three cycles where again the transition happens within half a window ($\sim 1.5\lambda_a$ $\sim$400nm). There is possible to observe that the transition takes more space but the frequency variation before the transition is reduced. Figure 5.14d, shows the resolution given by six cycles (resolution $\sim 3\lambda_a$ $\sim$800nm), it is possible to observe that the transition is wider but presents little variation. Also in this case both ideal and experimental responses are very similar which implies that at this depth resolution, the influence of noise is minimal. In all cases resolution is approximately half of the window size (for windows bigger than $2\lambda_a$) which lead us to estimate the depth resolution on experiments described below.

5.4.3 Fixed cells

Even though the results above show the viability of the transmission approach on cell phantoms, there are significant challenges when it come to a real cell. First, the damage thresholds are usually lower depending on the type of cell. The Brillouin shift at the cell-media boundary is significantly smaller reducing the contrast with the background, the thickness of a cell has a wide range: it can go from sub-micron at the edges to several microns at the centre. Additionally the cell is far from being a homogeneous material. All these points make a real cell a challenging subject. However, to understand better

the viability of this technique it is necessary to perform measurements on real cells. Before using live cells, fixed 3T3 mice fibroblast cells were used. Fixed cells have been preserved to prevent decay and putrefaction as closest to its natural state as possible. This not only to allow preservation of the cells but also to put them through invasive analysis that a living cell would not survive. Chemical fixation based on formaldehyde is by far the most common method, it creates bond between proteins and tissue, cross-linking macro-molecules and freezing the action in space and time.

Transducers were fabricated on 25mm round coverslips with layer dimensions approximately of 20nm of gold and 140nm of ITO. Then fibroblast cells were seeded on to the transducers and fixed 24hr later. Using a two-coverslip chamber (Live Cell Instruments Inc. chamilde CF-T), the fixed cells were kept in cell media during the experiment with gentle flow provided by a syringe pump. Scans were performed taking 15000 averages per point. The average power for λ_{probe} was 1mW and λ_{pump} was 0.5mW Each point took $\sim$4s to acquire (5ns, half window). The Brillouin frequency was built from the frequencies measured for each point of the scan.

Figure 5.15 shows a fixed 3T3 fibroblast cell and the result of a scan of its Brillouin and resonance frequency. The scan was 40x40 microns with one micron steps and the average SNR was $\sim$55. The Brillouin frequencies obtained from this experiment show good correlation with the optical image. The nucleus area in the cell clearly has a different Brillouin frequency, which to some extent, will be due to different speed of sound. Figure 5.15c shows a b-scan extracted from the middle of the cell and it shows the effect of the cell on the Brillouin oscillations phase. To try to apply any of the time of flight to this particular specimen is not possible since the ultrasound does not reach the cell/media transition. However, for a cell with thinner features, it would be possible to extract more information. 3T3 cells elaborate thin processes called filopodia when migrating across the substrate. These will be investigated further along.

Figure 5.16 shows the resultant acoustic imaging of over two fixed 3T3 cells. The

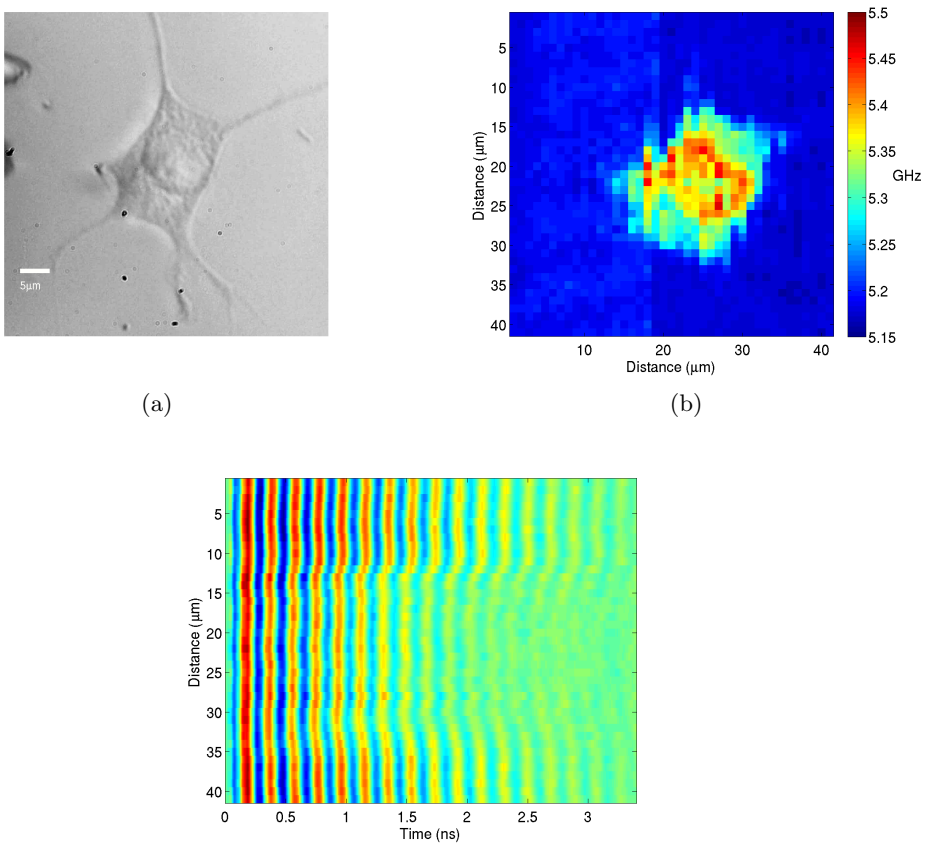

Figure 5.15: Brillouin oscillations of a fixed cell. (a)Optical image of a fixed 3T3 cell. (b) Brillouin map obtained using the transmittance approach. (c) b-scan of vertical line at 24μm

resonance frequency map (see figure 5.16c), extracted from the transmission signal, has lower SNR (∼40) than the Brillouin map (∼70). However the variation the standard deviation of the Brillouin frequency across the image is only 8MHz while the one for the resonance is 80MHz. This difference is due to the decay rates. As the resonances decays much quicker, the frequency is determined by only a few cycles making it more susceptible to noise. Anyway, the resonance frequency does show the footprint of the cell and not the filopodia (see figure 5.16a). And the filopodia are clearly visible in the Brillouin map (see figure 5.16b). Both results suggest a detachment of the filopodia from the substrate. From the two cells in figure 5.16b one has clearly higher Brillouin

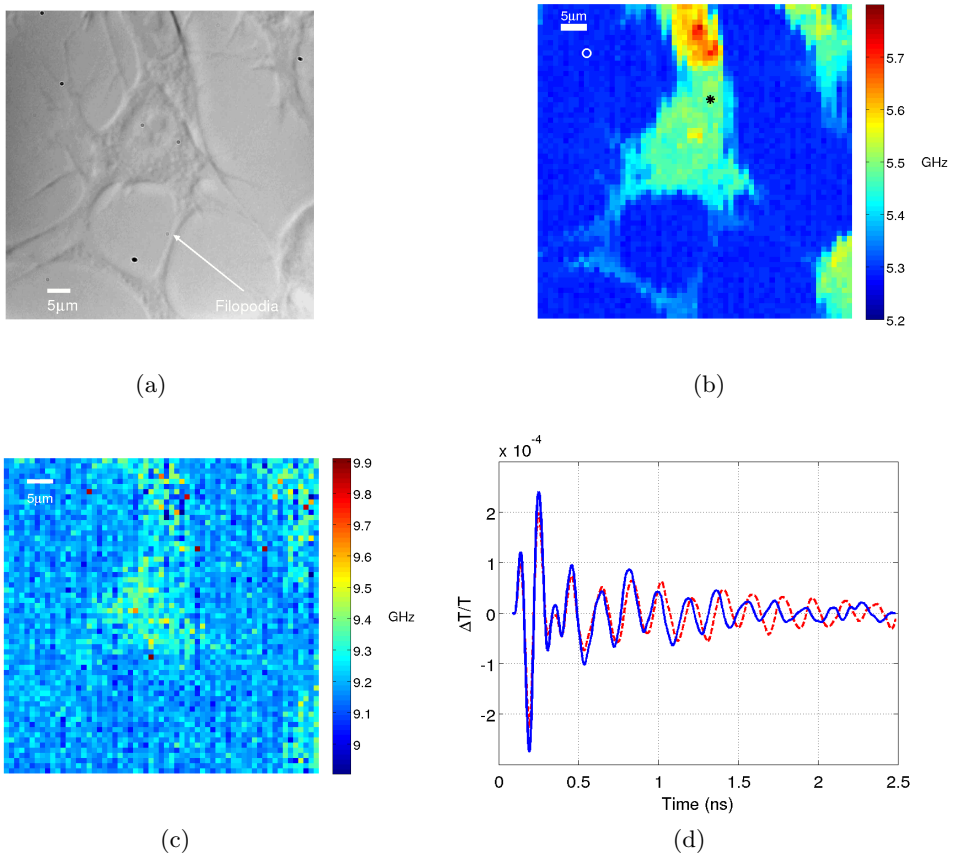

Figure 5.16: Acoustic imaging of a 3T3 fixed cell. (a) Optical picture showing filopodia, (b) Brillouin map obtained using the transmittance approach. (c) Resonance frequency map. (d) Sample traces from cell (*) and media (o).

frequency (above) than the other, this suggests that both cells might have different mechanical properties. This might indicate a different state of the cell cycle, as 3T3 are highly proliferative in culture. During cell division the DNA content of the nucleus is highly dynamic providing a possible explanation.

The short time Fourier transform was applied to the data presented in figure 5.16 instead of zero crossing, due to the STFT capacity to detect smaller Brillouin shifts. Figure 5.17 shows the result of this analysis. The time traces were divided in 9 short windows where each window lasts 4 acoustic cycles (1.2μm), with resolution of 600nm, and it is separated from each other by 130nm. There, the windows (a), (e) and (i)

are windows that are approximately separated by the resolution and hence can be considered true sections.

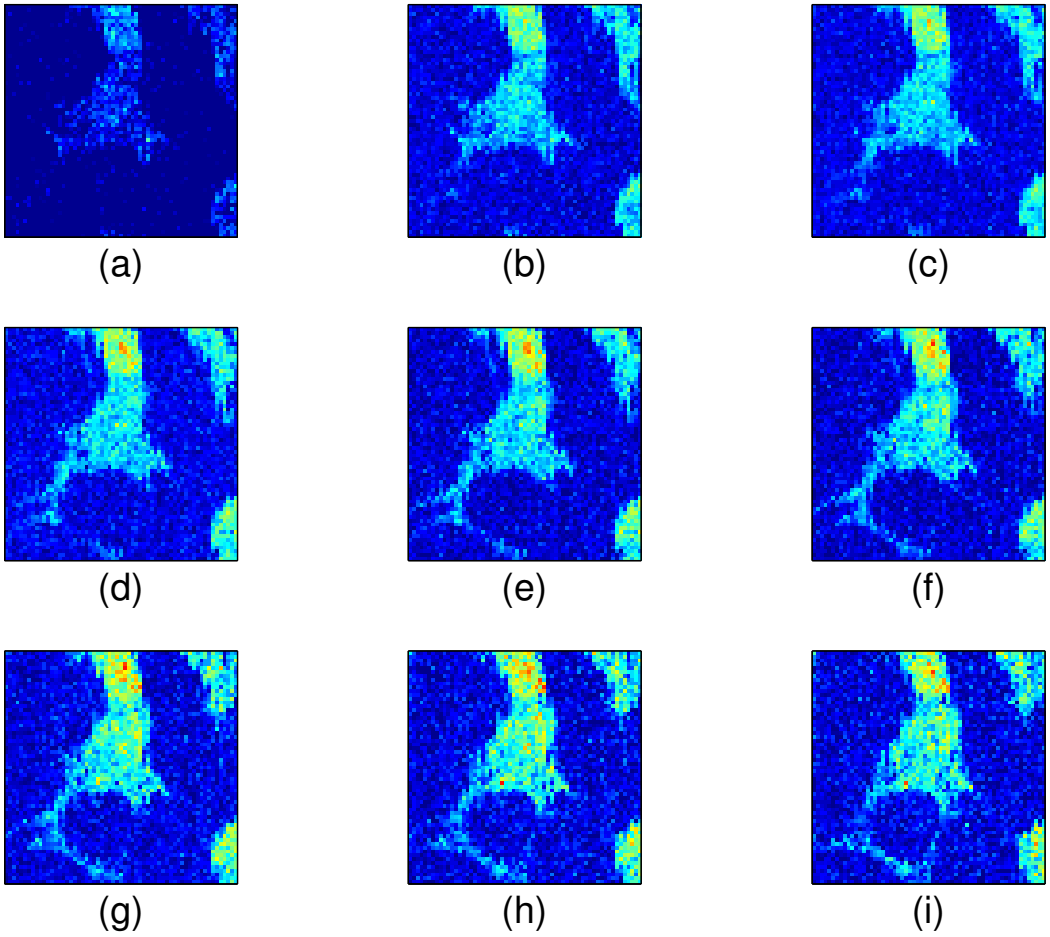

Figure 5.17: Short Fourier transform analysis of a 3T3 fixed cell. The Brillouin maps were obtained from 0.4ns windows shifter across 0.1ns. Windows (a), (e) and (i) are true sections.

Figure 5.17a shows no presence of the longer filopodia (below the nucleus of the cell) while the shorter ones (at both sides of the cell) are clearly visible. As time progresses, the short filopodia disappears while the long one becomes clearer. This means that some parts of the filopodia are not attached to the substrate. But as time goes on, it can be seen that different parts of the cell are on different planes, which allow us to estimate the thickness of the filopodia around 500nm.

Another important example of fixed cell imaging is that from a cardiac cell. This example is interesting because it shows the capability of the technique to observe complicated mechanical structures such as the contractile aparatus of muscle cells. For such a specimen, the resultant image has a level of contrast which is similar to that of the optical brightfield image. Figure 5.18 shows an example of cardiac cell acoustic imaging. For this picture, the step size for was reduced to 300nm in order to observe the very thin features. The structure of the cell exhibits very good contrast to the subcellular structure which allows muscle contraction. The transversal structure observed in the cell correspond to tubule which is attached to each other by fibres. When the cell contracts, the tubules come close together by the action of the fibres. This movement could produce stress that might alter the speed of sound of the cell and hence the measurement.

In figure 5.18c the resonance frequency of the transducer is shown. The lack of contrast on the right side of the image, suggests that the cell is not in contact with the transducer at that point. However this image is inconclusive since the background frequency observed on the left side on the picture differs from the right hand side and it is expected to be the same.

5.4.4 Living cells

Using the same chamber assembly but adding HEPES buffered media, it was possible to keep cells alive for more than 5 hours at room temperature (21^oC). The whole experiment was enclosed for temperature stability. The average powers for pump and probe at the transducer were 0.4 and 1mw respectively, meaning that the cell only sees 0.04 and 0.3 mW due to the transducer transmittance characteristics (see figure 3.5). Linear scans were attempted before performing full images due to the fragility of living cells.

Figure 5.19 shows the results of a line-scan over a living 3T3 cell with an optical

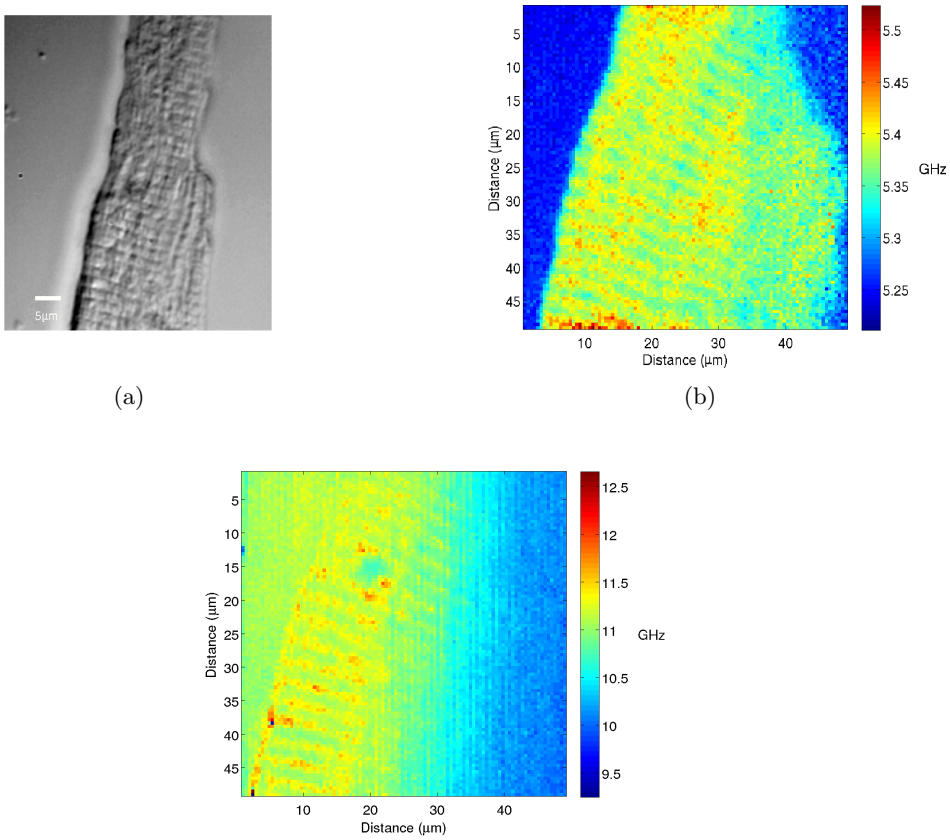

Figure 5.18: Brillouin oscillations on a cardiac cell. (a) Optical image of a cardiac fixed cell. (b) Brillouin map obtained using the transmittance approach. (c) Resonance frequency of the transducer.

picture of the scanned area before and after the scan. The scan was 40μm with 1μm steps. 15000 averages were acquired for each point requiring approximately 4min of scanning time and SNR was ∼60. The resultant Brillouin profile (figure 5.19d) shows good correlation with the optical picture (figure 5.19a). The b-scan (figure 5.19b) shows clearly the effect of the cell on the phase of the waves. Similar to the fixed cell case, the frequencies are higher in the centre of the cell than on the edges. Figure 5.19c shows the optical picture afterwards which shows no signs of obvious trauma, an indication that the cell have survived the experiment. Additionally, the cell was monitored for

15 minutes after the experiment ended showing dynamic activity, suggesting normal function.

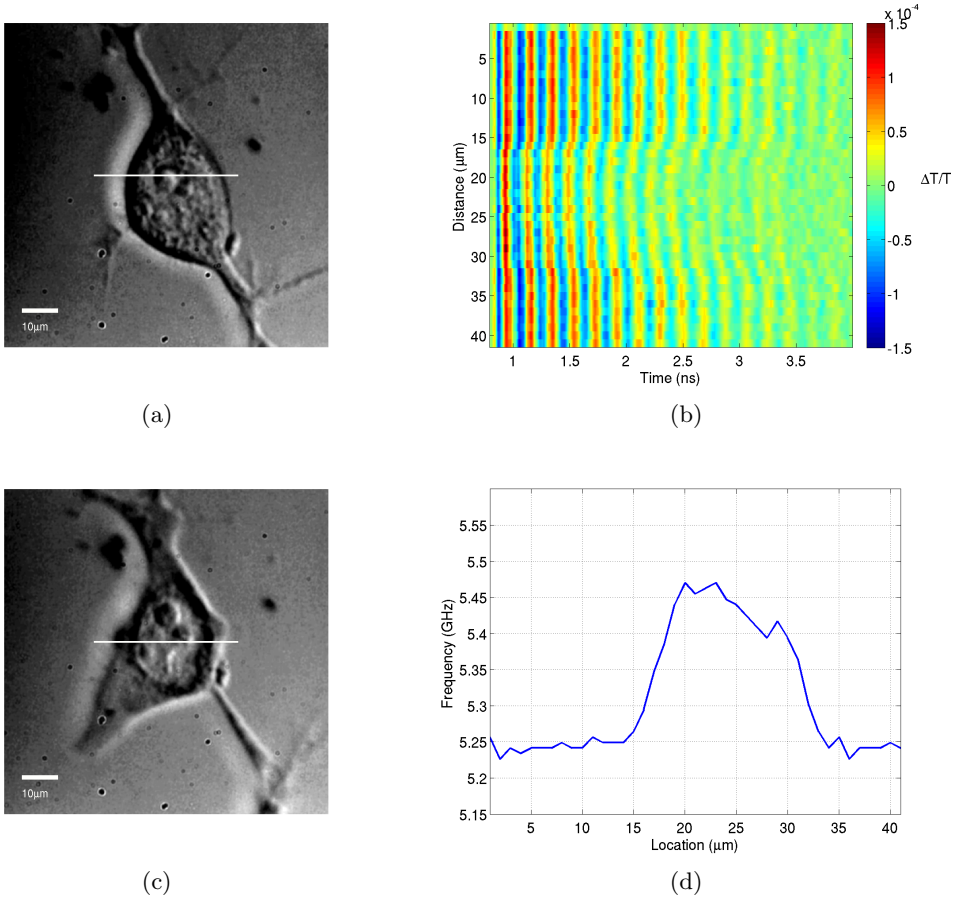

Figure 5.19: Brillouin line-scan over living 3T3 cell. Optical picture of the cell before(a) and after (c)the scan. c) Brillouin frequency obtained. d)Bscan of the 3T3 cell. The topology of the cell in (c) after the scan shows signs of good health which appear to have survived the scan.

A full scan then was performed on a similar 3T3 cell. Figure 5.20 shows results from a full scan on a living 3T3 cell with optical pictures of the scanned area before and after the scan. The scan was 40x40μm with 2μm steps taking 15000 averages for each point leading to approximately 27min of scanning time and SNR of ~70. Average power remained the same. The resulting Brillouin map (figure 5.20d) shows good correlation with the optical picture(figure 5.20a). The b-scan (figure 5.20b) shows clearly the

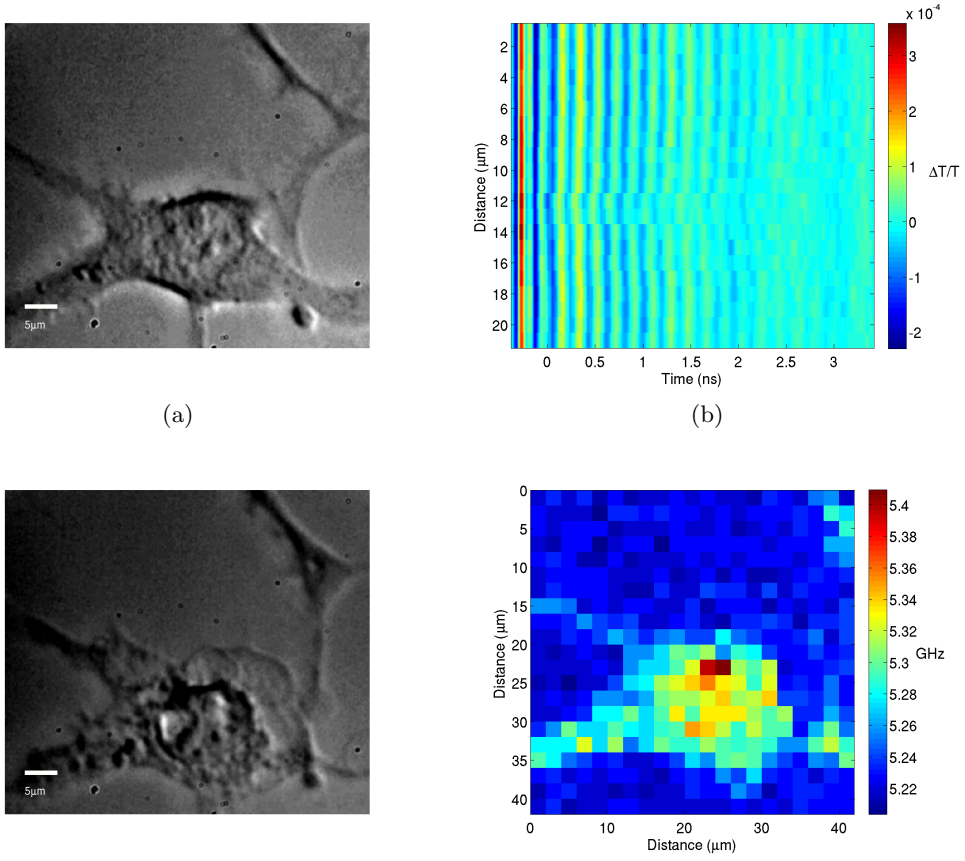

Figure 5.20: Scan of the Brillouin frequency over living 3T3 cell. Optical picture of the cell before(a) and after (c) the scan. Brillouin frequency obtained (d). Bscan of the 3T3 cell (b). The topology of the cell in (c) after the scan shows signs of physical damage.

effect of the cell on the phase of the waves. Some of the filopodia of this cell are also detected. Figure 5.20c shows an optical picture taken straight after the experiment was completed, where the cells morphology has changed significantly.

Comparing the optical images before and after the scan for the 2 dimensional scan case, we can see that the changes in cell morphology indicate a state of poor health; the membrane of the cell is blebbing, indicating physical damage. If the same comparison is done for the line-scan case, the cell looks in much better state and shows signs of activity 15 minutes before and after the experiment was performed. Even though the fully scanned cell showed signs of stress, it shows that the contrast observed in a living/non-fixed cell is similar to that of a fixed cell.

It is unclear how much the laser light, heat and sub-optimal(non-incubator) conditions were affecting the cells. The soundwave itself is unlikely to disturb the cell as it has been reported previously at 1.7GHz[27] and on the last experiment shown in figure 5.19, the mobility(recorded) and morphology of the cell on seen on figure 5.19c indicates of good health.

Assessing cell viability

To asses the health of the cell, cells were prepared with two fluorescent dyes; one that fluoresces when the cell is alive (calcein-AM) and another when it is dead(propidium iodide). Calcein-AM (acetomethyl ester) is a dye that does not fluorescent by itself. If the cell is alive, enzymes on the cell cut it making a fluorescent product that gets trapped inside the cell. If this fluorescence occurs then it is considered that the cell is alive and functioning. Propidium iodide is not fluorecent either unless it bounds with the DNA of the cell. However this dye is not permeable through the cell membrane and only can get through if the membrane is broken. Thus, if fluorescence of this dye occurs, it is considered that the cell is dead. In this way it is possible to assess in a more rigorous way the state of the cell. Such experiments were performed on etched

coverslips (with a numbered grid), which helped to find the same individual cells in different setups (this experiment and a fluorescent microscope).

The cells were prepared with stain and the chamber assembled. The assembly was taken to a fluoresce microscope where the cells were assessed before the experiment. Figure 5.21 shows the selected cells for scanning before the experiment; figure 5.21a shows a phase contrast image of the selected cells and figure 5.21b its fluorescence showing all cells are alive (green). Once the cells health had been verified and their position identified (within the grid), the assembly was translated to our setup to perform scans on cells A B and C marked in figure 5.21. The scans contained only 9 points using 0.3mW average pump power, covering 45μm in 5μm steps, taking less than a minute per scan and having a SNR of $\sim$40. The result of the scans are shown in figure 5.21c, (d) and (e). The measured Brillouin frequency shows similar behaviour to previous experiments. After the scans were performed the assembly was taken back to the fluorescence microscope to assess the cells again. Figure 5.21f shows that none of the cells had died after the experiment.

Having succeeded with short scans on living cells, longer scans were attempted with the aim to build images. Power and averages were reduced to increase the chances to see a cell surviving, however, experiments were not successful. The fluorescence imaging was performed on a different microscope than our experiments and this brings a number of complications. Cells need to survive under flow at room temperature and handling between facilities. This along with the increment of laser exposure made the preservation of cell viability challenging.

Figure 5.22 shows the result of two scans. On figures 5.22a, d and e correspond to a scan with 30% less averages and 25% less pump power compared to previous experiments. The quality of the Brillouin map is compromised (SNR $\sim$30), however the cell didn't survive (see figure 5.22e). Further reduction of pump power %50 and averages 60% compared to typical values made a stronger compromise on SNR ($\sim$15)

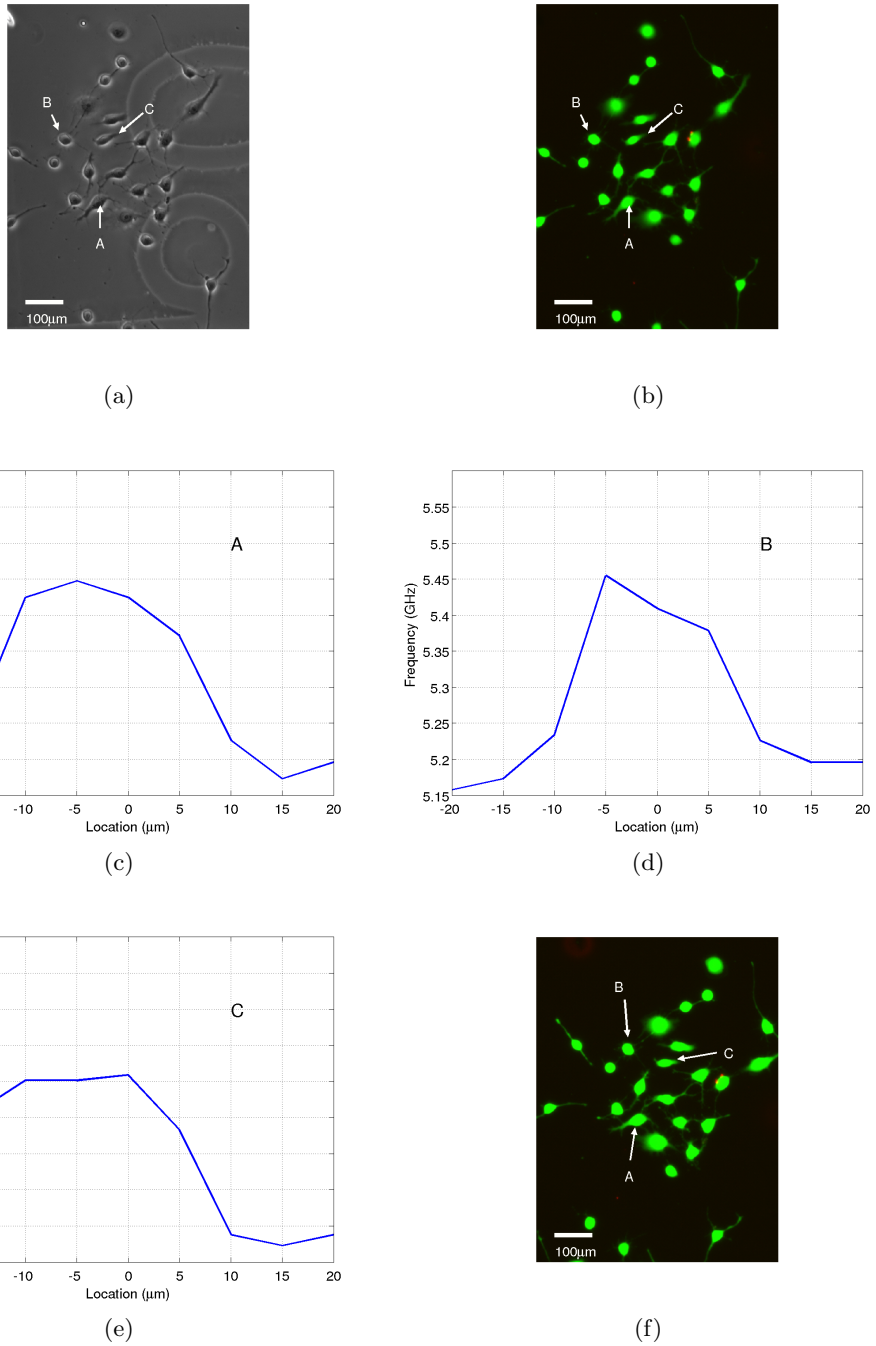

Figure 5.21: Non-destructive line-scan of the Brillouin frequency over living 3T3 cells. Phase contrast image of the cells before(a) the scan and fluorescence assessment (b). Brillouin frequency obtained for cells A.B and C (c-e). (f) Fluorescence assessment after the experiment shows that the cells are still alive (green).

without keeping the cell from dying(see figure 5.22f).

At this point it was not clear if handling, light absorption or heat (produced by the acoustic generation process) was the reason for the cells dying. From the literature, it has been reported that cells can stand up to 1mW of NIR laser light [105] (150fs pulses repeating every 10ns) and that UV-C (100-290nm) damage has been detected for exposures as small as 0.5Jm^{-2} over 5 minutes [107]. Assuming that the cell had 30μm*30μm area, the exposure of the cell would be 153pJ/s. With our approach, the pump exposure is below the NIR reported safe dose (0.4mW, for similar pulse characteristics). For the case of the UV(390nm), considering the shielding of the transducer, we expose the cell to 0.4pJ total energy per pulse which becomes 40μJ/s. We are exposing the cell to larger UV dose, however this is done in a small volume for very short time periods. It is not clear if light exposure is the main source of damage, while may also be due to heat accumulation (see section 3.4.1).

Live cell imaging using PLU

Changes in the material substrate and handling where made to reduce thermal and handling induced-stress. Fluorescence detection capabilities for propidium iodide were incorporated in our setup, (see section 4.2) avoiding the need for transportation and reducing the time out of the incubator. Finally, the glass substrate was substituted for sapphire, which has ∼30 times greater thermal conductivity. This kind of substrate has been used before for PLU experiments on cells [99], and our simulations showed significant reduction of the temperature rise in the cell/transducer interface when sapphire was used as a substrate (see figure 3.12).

In order to understand the extent of the effect of those changes, additional measurements on living cells using were performed. Three cells, marked A,B and C in figure 5.23 were scanned with the same exposure time per point and typical pump power (0.4mW, 2.4mJ/min). The scanned area also remained the same but the step

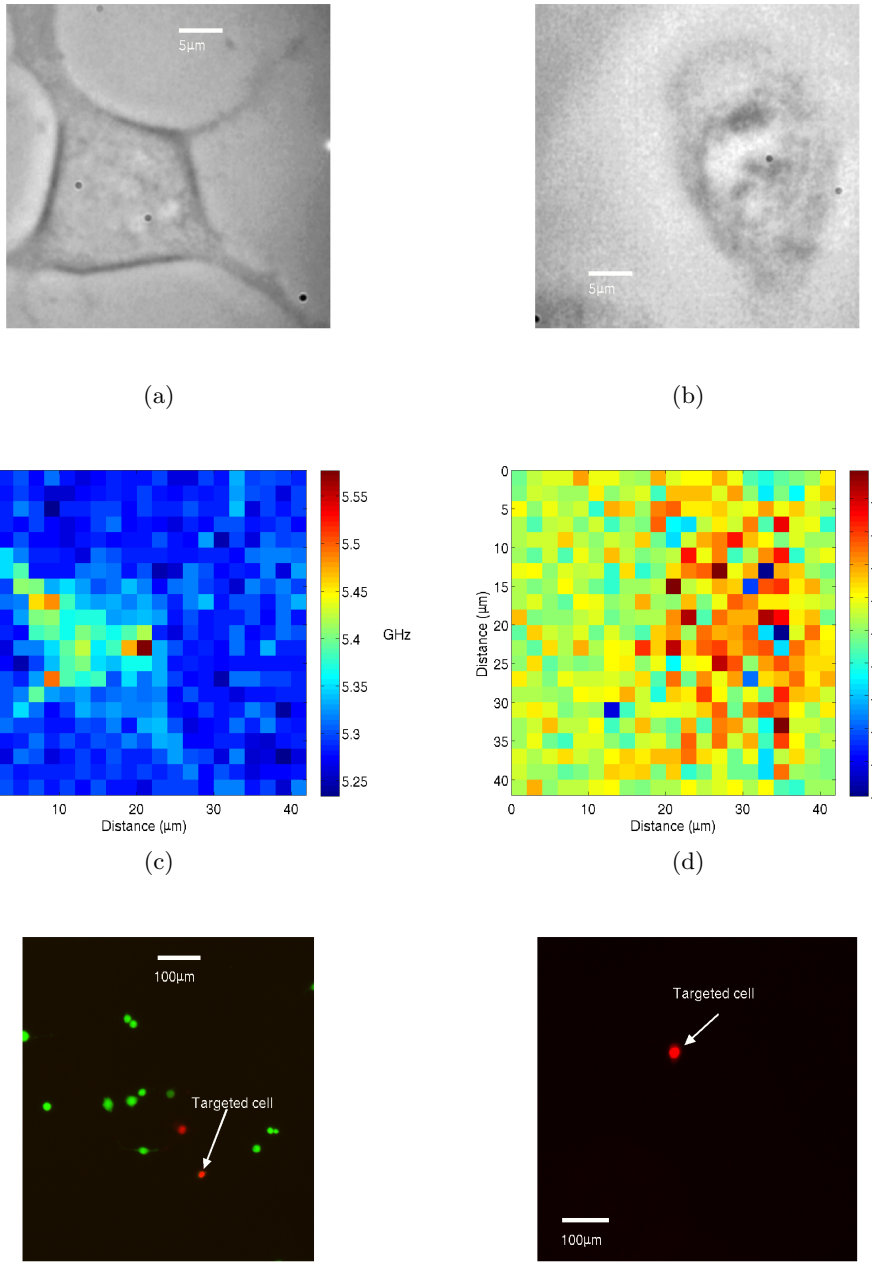

Figure 5.22: Scan of the Brillouin frequency over two living 3T3 cells. (a,b) Brightfield image of the cells before the scan. (c,d) Brillouin map of the scanned area. (e,f) Fluorescence assessment. Both scans were 40 by 40 μm with 2μm steps. Both experiments , (a,c,e) and (b,d,f), progressively less pump power and averages to reduce exposure(5K,3K averages and 0.3, 0.15mW respectively).

size changed, consequently changing the number of points. Cell A(figure 5.23a,b) contained only 100 points (0.17J total energy) lasting approximately seven minutes. Cell B contained 400 hundred points (0.73J total energy), having 30 minutes of scanning time . Cell C contained 1600 points (2.9J) and took approximately two hours to be completed. All experiments had an SNR of $\sim$40.

Cells A and B show good correlation with the optical picture but, more importantly, the fluorescence assay shows that they are still alive after the experiment was concluded(see figure 5.24). This is a demonstration that PLU on biological cells is possible. It is possible that the larger acoustic impedance of sapphire, which is better matched to that of gold, leaked more acoustic energy into the substrate reducing signal amplitude introduced to the cell. This could have reduced the penetration depth and hence inner cell structure is harder to detect. For the longer scan applied to cell C, there is a clear change in Brillouin frequency as the scan progresses (left to right) potentially coming from the fact that the cell is dying since the fluorescence assay shows the cell was dead by the end of the experiment.

If the change in Brillouin frequency observed in cell C is related to the changes in the cell physiology while dying (for instance, by apoptosis), that could explain why the measured Brillouin frequency of the cell is shifting. In apoptosis the cell swells before contracting and detaching. Those changes could be the cause of the Brillouin frequency change observed in cell C. It is also possible that by the end of the scan the cell is detaching, making the response of the Fourier transform peak to shift lower due to the presence of media under the cell. This is an example of the potential use of this technique to characterise cell processes with a mechanical contrast mechanism.

After the experiment was concluded, media was flowed to a solution of triton X-100 detergent as positive control to verify the cells were alive during the experiment. Figure 5.24 that the cells A and B only accumulated dye after the application of detergent, demonstrating the that the cells were alive during the experiment.

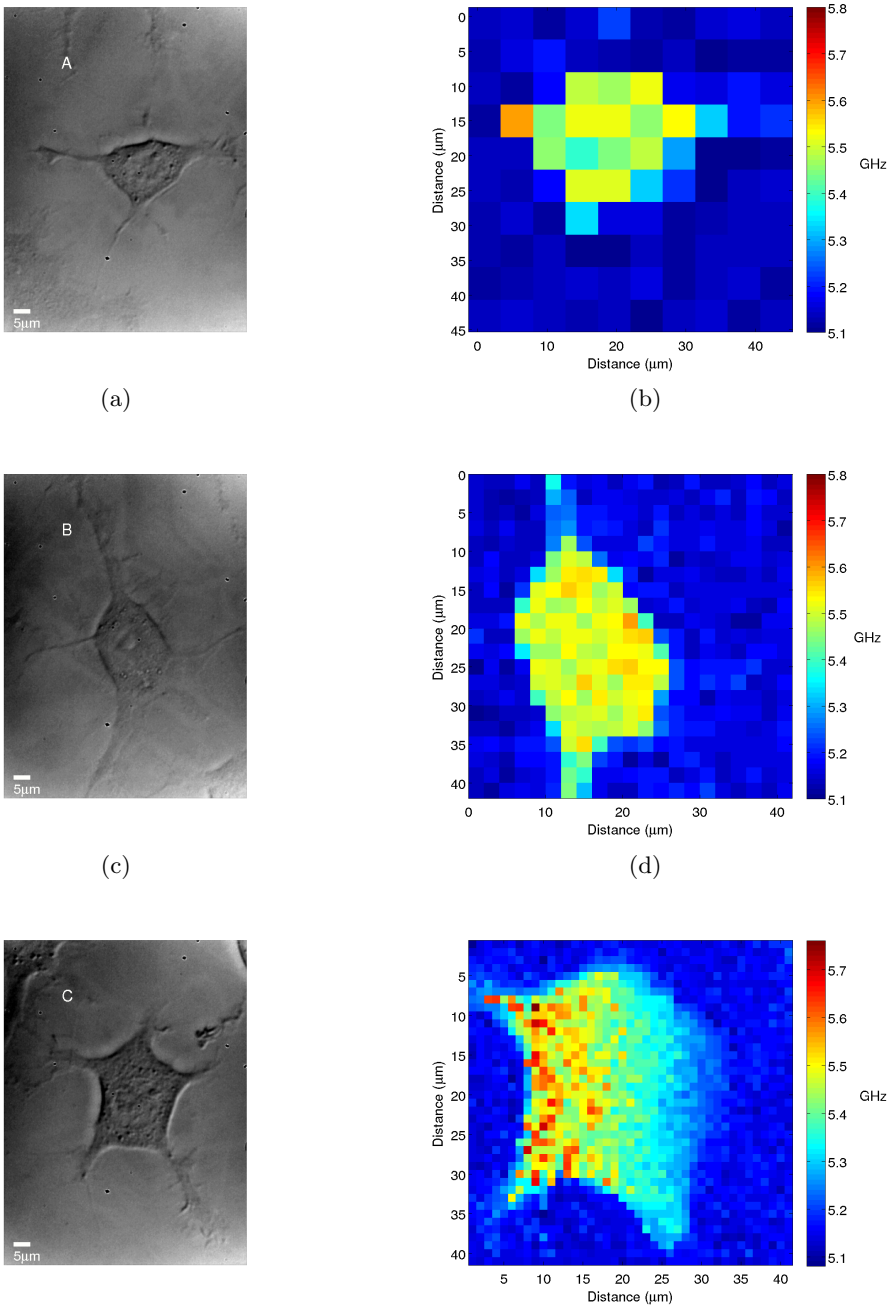

(a) (b) (c) (d) (e) (f)

Figure 5.23: Scan of the Brillouin frequency over living 3T3 cells A,B and C on sapphire coverslip. (a,c,e) Brightfield images of the cells before the scan. (b,d,f) Brillouin map of the scanned area. All scans used same amount of power and number of averages, the scans were 40 by 40 μm with 4(b), 2(d) and 1μm(f) steps.

5.5 Summary

Transducers for imaging Brillouin oscillations in cells proposed and modelled in chapter 3 were fabricated and tested with the methods of chapter 4. Based on these, the models were successfully validated with experimental results. Optical characteristics like transmittance and sensitivity and mechanical properties like resonance frequency showed good agreement with the experimental measurements.

Then the transducers were applied to the detection of Brillouin oscillations in transmission. First water films and then phantom cells were used to demonstrate the approach as well as the signal processing. Based on these, images of the Brillouin frequency of phantom and fixed cells were acquired and expanded to three dimensions. Finally, the first PLU images of living cells were successfully performed where the health of the cell was confirmed with fluorescence markers. The use of a sapphire substrate reduced thermal stress which allowed us, along with the novel approach presented here, to image living cells using PLU. Sapphire also provides different acoustic matching to the transducer compared to glass. This affects the amount acoustic energy going into the sample and the decay rate of the transducer resonance. Nevertheless these demonstrations can have a significant impact in cell research as this method could bring complementary information never acquired before.

The Brillouin frequencies measured on cultured cells were between 5.25 and 5.5GHz with 50 and 250MHz shift from the background. Assuming the refractive index of 1.36[114], the speed of sound would change from approximately 1548m/s to 1605m/s. Near the edges of the cell, the shift is harder to measure because the cell is thinner round those areas so the dominant frequency on the FFT becomes that of the media. However, those thin features can be reconstructed in three dimensions by time-resolving the Brillouin frequency. Living cells can also be imaged using our technique where the temperature rise is a major source of damage, as demonstrated by the positive effect

of changing the thermal characteristics of the substrate.

In all our experiments, the measured modulation depths are significantly higher with respect to previous PLU approaches. For instance, in a conventional reflection mode PLU measurement in vegetal cells[66], where the measured modulation depth is $\sim$2x10^{-6}, the cell is exposed to 0.05mW and 1.6mW of pump and probe (input and reflection) light respectively. In comparison, the system reported in this work achieves a modulation depth of 10^{-4} ($\sim$50x increase) with the cells exposed to the same pump power of 0.05mW and 0.4mW of probe. Part of this improvement comes from the shielding by the transducers, where the cell is exposed to only 0.05mW but the actual power used to generate the ultrasound is 0.5mW. Secondly, the transducer generates waves more efficiently by concentrating more energy in the bandwidth we are interested in. Further modelling and experimentation is required to fully understand the origin of the amplitude gain we observe. This will also help to continue developing these transducers towards live-cell imaging applications.

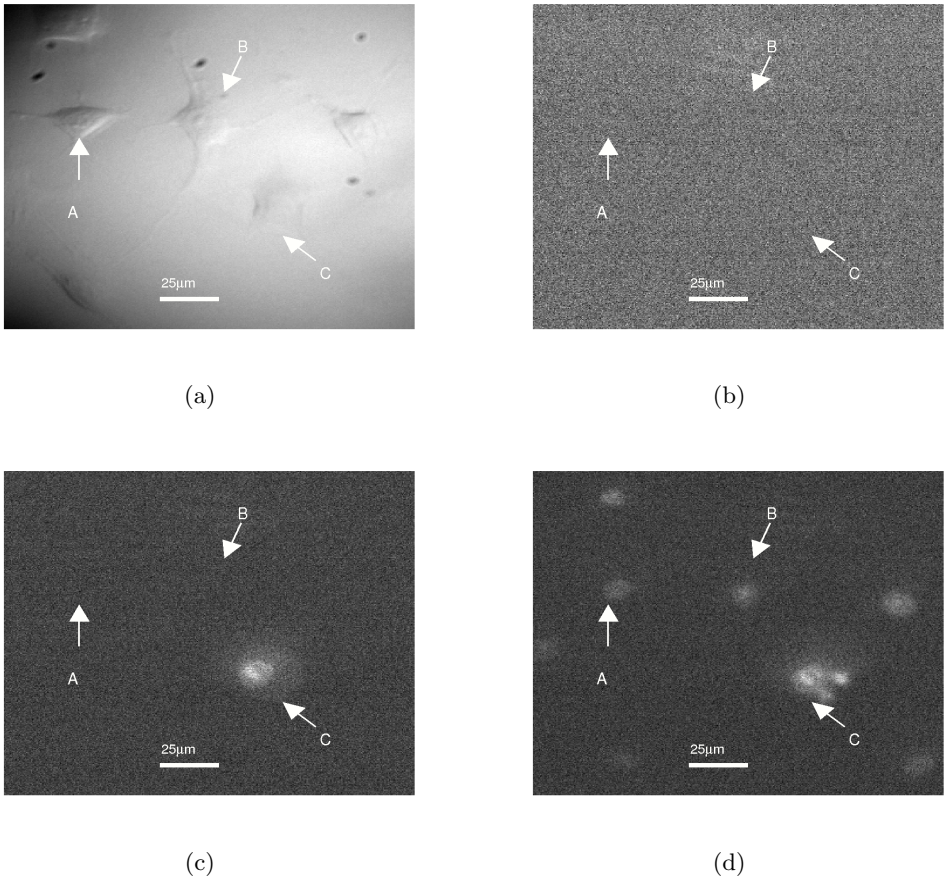

Figure 5.24: Fluorescence assay (propidium iodide) of living cell experiments on sapphire substrates shown in figure 5.23. (a) Optical image of the cells under scan. (a) Lack of emission wavelength before the scans were performed shows cells are alive. (c) Detection fluorescence after the experiments. Only cell C (see figure 5.23) shows accumulation of the dye which is denotes cell death. (d) Detection of propidium iodide emission after the cells were deliberately killed by adding Triton X-100 detergent into the solution. Cells A and B lit up demonstrating cell were alive during the experiments.

Chapter 6

Future work

6.1 Introduction

The technique presented and demonstrated here has many advantages over current approaches to picosecond laser ultrasound imaging of biological cells. Based on optical cavity transducers, it has the potential to image not just cultured cells but of other transparent micro-objects. However, there is still improvements to make to acquisition time, penetration depth, and signal-to-noise ratio(SNR). Additionally, the measurements are still not fully quantitative as they require knowledge of the refractive index of the sample. The transducer could be also used in different ways for different purposes. In this chapter future improvements and applications of the three layer thin-film transducers are discussed.

6.2 Transducers future improvements

Cavity finesse

If an alternative fabrication process to sputter coating is used to fabricate the transducers, it would be possible to deposit a highly transparent dielectric such as silicon

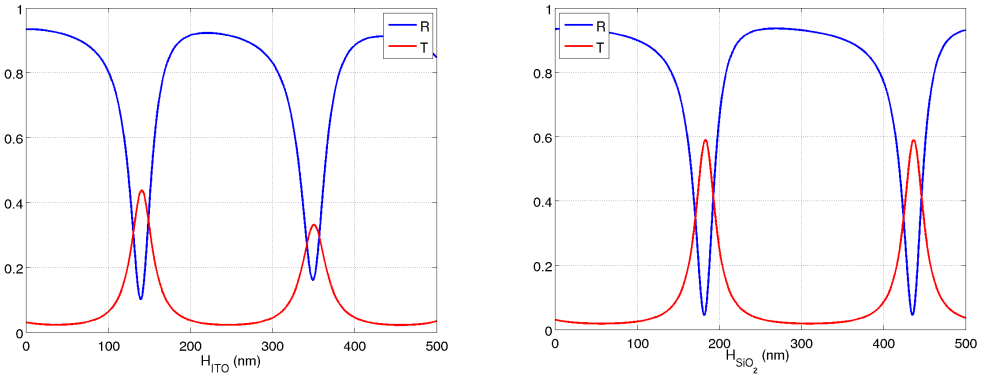

(a) (b)

Figure 6.1: Simulated transmittance(red) and reflection (blue) at λ_{probe} against dielectric thickness. (a) ITO. (b) SiO_2

dioxide(SiO_2), this would improve transmittance for λ_{probe} while reducing it for λ_{pump}. By doing this it would be possible to increase the thickness of the gold layers without compromising detection levels. Higher finesse will also increase sensitivity which will give greater resonance signals.

Figure 6.1 shows a comparison of transmittance and reflection against dielectric thickness for λ_{probe} with ITO and SiO_2. There it is possible to see that the maximum transmittance of the transducer is significantly increased for the SiO_2 case, especially when the dielectric thickness becomes thicker. There is a second resonance peak that shows little loss in amplitude compared with the first which leaves the option to build thicker transducers with higher finesse and efficiency.

Higher transmission means the use of thicker gold layers which can be used to increase pump light rejection while keeping the amount of transmitted light the same. It is also likely that a SiO_2-based transducer will have lower resonance frequency compared an ITO-based devices. Lower resonance frequency means higher acoustic amplitude as the resonance gets closer to the Brillouin frequency. If the second resonant peak is used instead, it is likely that the transducer will resonate at a frequency low enough that it will overlap the Brillouin frequency expected from a cell. This could provide higher

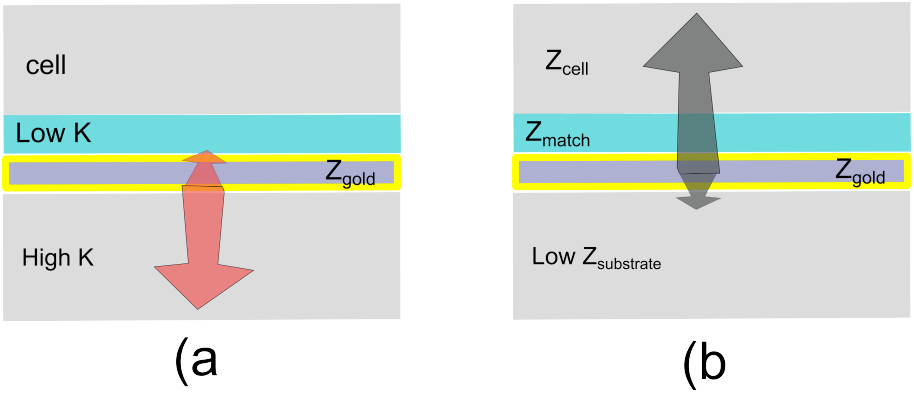

Figure 6.2: Improvements on thermal and acoustic management. Substrate and matching layer conditions for thermal(a) and acoustic management(b).

SNR with a trade-off of signal processing (since resonance and Brillouin frequencies might be very close together).

Thermal and acoustic management

We have seen that heat accumulation at the focal spot is an important source of damage for cells. For this reason, heat must be managed to avoid premature cell death. The way we have demonstrated that, through a high thermal-conductivity substrate, produces loss of acoustic energy. This loss is because the impedance matching between the gold/sapphire interface is better than the impedance match in the gold/glass boundary. To reduce this effect, a different substrate and the addition of an extra layer could be implemented (see figure 6.2).

A substrate material with an acoustic impedance significantly different than that of gold and high thermal conductivity would be ideal for this application, dissipating heat while preventing the loss of acoustic energy by providing an interface with high acoustic reflectivity.

Moreover, an extra layer between the cell and the transducer could be also useful to provide maximum thermal insulation while serving as an acoustic matching layer to improve acoustic transmission. This layer then should have an acoustic impedance

that matches that of gold with that of the cell ($z_{match} = \sqrt{Z_{cell}Z_{gold}}$). This layer will also delay the Brillouin signal of the cell into a temporal space which no longer overlaps with the transducer response and the coincidence peak. This could simplify the removal of the thermal decay allowing the resolution of the Brillouin frequency of the specimen completely. The downside is that the transducer resonance will no longer provide information on the transducer/cell boundary.

Further reduction of thermally induced damage to the cells could be achieved by changing the scanning pattern. For instance, by separating a scan into four smaller scans where each partial scan has longer steps. The longer steps will separate the hotspot produce by the laser further from the previous spot to reduce the thermal stress on the cell. This approach requires high stability of the mechanical stages to be able to reconstruct an image without introducing distortion.

6.3 Experimental arrangement improvements

Acquisition speed

Acquisition speed is one of the major limitations of picosecond laser ultrasound. Although the ASOPS system has improved it significantly compared to a mechanical delay line, this kind of system is still not exploited completely. In our particular setup, only approximately 30% of the pulses is captured by the acquisition system giving opportunity for improvement. However, even if the ASOPS system is working at maximum capacity (capturing all the pulses), it would still be relatively slow compared to conventional optical systems due to the need for raster scanning and averaging.

It is possible though to perform parallel acquisition by splitting a beam into a line of points and then detecting each point on an independently-digitised photodiode. This would allow an increase of the acquisition speed by a factor that equals the number of points in the arrangement. This has been successfully performed in the past by focusing

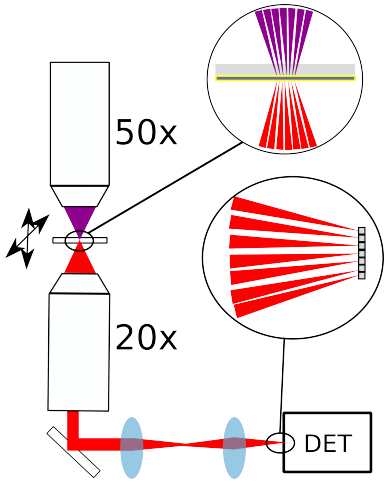

Figure 6.3: Simplified schematic of proposed parallel detection.

the lasers into a line rather than a point and then detecting with an array of detectors rather than a single photodiode[115]. This method promises to be a much faster way of doing GHz range ultrasound imaging.

There are technical challenges to address in order to apply this method. Overlapping the multiple pump/probe spots using the same objective might be difficult since the wavelengths are different. Each beam path should have its own diffraction element to create a pattern in the focal plane. Moreover, the detector array should have an output for each element which can go to a multichannel amplifier and acquisition system to keep true parallel detection. This kind of acquisition system is expensive. However, it would only be a fraction of the cost compared to a high power ASOPS laser system required to perform such a task.

Figure 6.3 shows a possible configuration to perform parallel detection, where a line of points is focused onto the sample. This kind of pattern can be achieved by commercially available diffraction elements. Two diffraction elements, one for each beam, should be used with their correspondent optics to produce the correct diffraction pattern in the back focal plane of the objective before combining the two laser beams.

The probe beam would be captured in transmission and focused to an array of detectors with a set of lenses to adjust magnification.

The separation of the points will depend on the magnification of the objective and it would be ideal to keep them separated by a noticeable distance to reduce photodamage. At the same time, the line can be rescanned at different positions to increase resolution.

Differential Detection

Differential detection is a well-known way of reducing coherent noise[116]. The concept is simple, if two coherent noise signals are subtracted they will cancel each other. Typically a beam is split into two, one of them is modified in a measurement process and then both are subtracted to cancel the common noise revealing the signal of interest. To have maximum effect, both signals should be as similar as possible. This in an optical system means that intensity and optical path should be well controlled.

In our case the signal is split in the transducer itself. The transmitted and reflected beams are then detected individually and subtracted in the postprocessing. As signals in the transmitted and reflected beams are out of phase, they will add to each other increasing signal amplitude with respect to the noise. Figure 6.4 shows an example of differential detection. The green trace corresponds to the transmitted beam, the red to the reflected beam and blue represents the subtraction of both. An improvement in the signal level is seen in the subtracted signal due to addition of signals from both channels. Noise though, remains similar due to the lack of temporal coherence.

Even though the reflection is larger than the transmission when the beam splits at the transducer, the losses on the reflected beam path make the intensity of the detected transmission beam larger. Temporal coherence is not critical since the SNR gain comes from adding signal contributions, however if the detected beams were temporally coherent, random noise could be reduced as well.

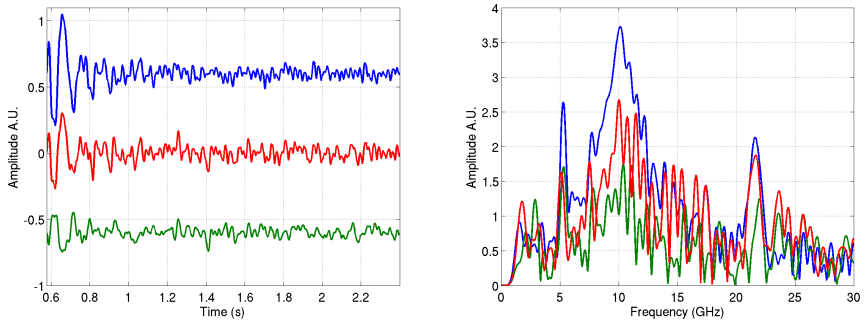

(a) (b)

Figure 6.4: Example of improvement of weak Brillouin signals using differential detection. (a) Time traces. (b) Fourier transforms. Green trace is transmittance, red one is reflectance and blue one is the subtraction of both

To perform differential detection in our setup, more acquisition channels are needed, reducing significantly the acquisition speed is significantly. However, the simultaneous detection of both channels is useful as the resonance frequency provides additional information.

6.4 Incorporation with other optical systems

The kind of measuring system presented here could be integrated with other useful imaging tools like fluorescence, phase contrast or two photon imaging for localisation of features and identification of cell processes whose mechanical behaviour is not known and might be of interest. In this work, the use of PLU on living cells is demonstrated. By increasing speed of acquisition, biocompatibility and SNR, it could be possible to incorporate this live cell mechanical imaging tool into other optical systems.

In chapter 5 the ability to incorporate our technique with fluorescence was demonstrated. Also we have used this system along with phase contrast imaging. For example, the resonance frequency map of a protein stamp presented in *Smith et al*[88] was taken with a phase contrast objective which allowed phase contrast imaging. Figure 6.5 shows

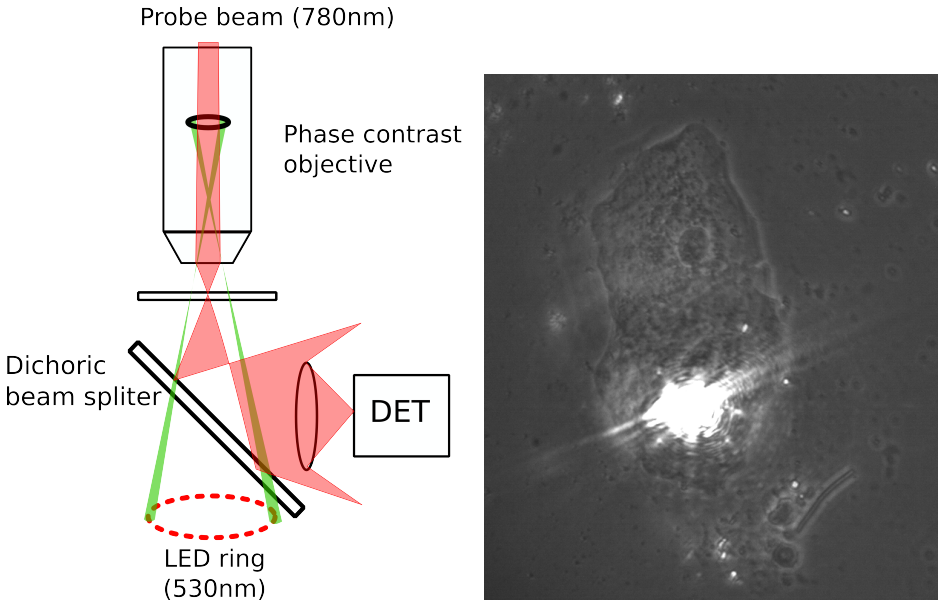

Figure 6.5: Example of implementation of phase contrast and PLU. (a) Schematic of detection. (b) Sample image of a cheek cell where probe laser is on.

an example of such implementation. An LED ring is used for illumination[117] and a dichroic mirror is used to separate the ring and probe lights. The selection of wavelength of the ring depends on the available transmission window. For the case or our transducers this wavelength can be between the pump and probe wavelengths. Green LED ring (530nm, approximately transmission peak of gold) has been used for this purpose with good results (see figure 6.5) which can be implemented when the detection is performed in reflection. For this case the detection is performed in transmission, the problem becomes more complicated as there are difficulties in separating the probe and illumination light. This has been done in the past but there is a significant loss in transmitted light. This loss comes from the constrains in the size of the rings which force to catch the probe beam after it has diverged significantly. However, more sophisticated system design to prevent losses could allocate phase constraint along with PLU in one system.

6.5 Data post-processing and modelling future developments

Three dimensional reconstructions

There is large amount of information captured in our experiments; Brillouin oscillations and the resonance of the transducer provides relevant information about the cell and its properties. However, to extract this information accurately is not an easy task. Noise and poor contrast requires these of more sophisticated methods than the ones presented in chapter 4.

As demonstrated in chapter 5, resolving in time the Brillouin frequency can lead to three dimensional reconstruction of the speed of sound of the sample if the refractive index is known. This method of imaging will also require strict validation by well recognised quantitative topography measuring methods such as AFM or profilometer. By resolving the Brillouin frequency in time, it could be possible not only to reconstruct phantoms, but also any complex micro-object comprised of different materials.

FEM modelling

Modelling is planned to be extended for different dielectric layer and substrate materials different of that of the currently modelled transducer design. To understand the sensitivity of the resonance of the transducer, a variation of the optical model is also required. Alternative dielectric materials such as SiO_2 will produce different mechanical responses compared to ITO, which is relevant design information. Similarly, for the case of the substrate material, sapphire will produce different response from that of SiO_2 which needs to be investigated.

The current model can be easily modified for new materials. However, to develop a model that helps understand relationships between sensitivity of the resonance frequency of the transducers to the properties of the imaged material, a more complete

model is required. That model needs to have an extra layer with properties such as, elasticity, thickness or density changing in a controlled way. These models will help understand the relationship between the parameter we measure against the properties of the damping material (specimen).

6.6 Alternative and extended applications

The transducers shown here could be used as narrowband generators and detectors of ultrasound, as transducers to perform detection of Brillouin oscillations or to map the acoustic conditions of a boundary. These transducers could also be applied in different ways for different purposes, In this section two alternative applications off the transducer will be presented.

Pitch-catch configuration

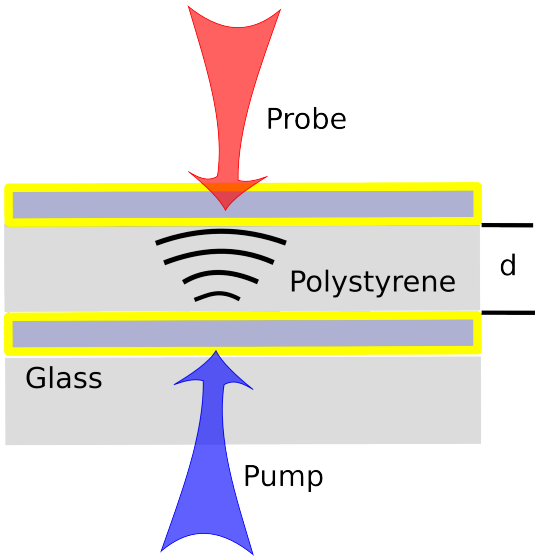

Figure 6.6: Simplified schematic of pitch-catch experiments using a polymer layer. Pump beam induces the generation of an acoustic wave in the pitch transducer while the probe transducer detects it on different transducer

The pitch catch configuration needs two transducers, one for generation and one

for detection. The arrival time will be related to the thickness and speed of sound of the gap between the transducers. Figure 6.6a shows an example of this configuration. One transducer is used to generate the sound by the absorption of the pump beam. The sound then propagates through media to be detected in a second transducer with similar layer dimensions (and resonance frequency). This configuration could avoid the need to know the refractive index to calculate the speed of sound as in the case of Brillouin detection. However, the measured speed of sound would be averaged over the gap between the transducers. Moreover for the case of a object smaller than the gap, would be necessary to know the thickness profile of the specimen.

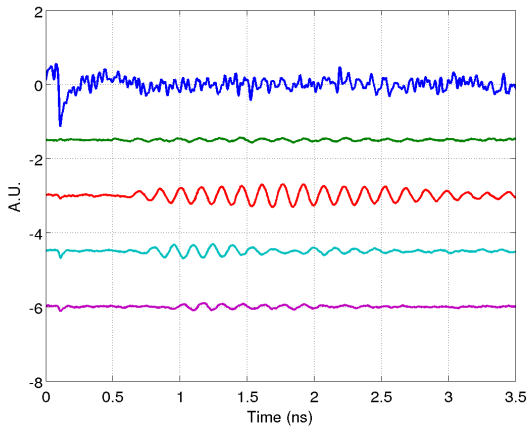

Figure 6.7: Pitch catch experimental results between a polystyrene layers. Blue trace indicates time of arrival of pump beam. The rest of the traces indicates detected signal on the catch transducer for different polystyrene concentrations of spin coated solution; green 7.5%, red 10%, blue 12.5% and purple 15%)

There are also technical challenges to be addressed. The distance between the transducers needs to be well known. This kind of separation ($\sim$10μm) requires a high level of surface flatness as well as high precision to assemble such device.

Preliminary experiments were performed with polymer thin films where the second transducer is deposited on top of the polymer layer. This avoids the need to set a microscopic gap. However, the thickness of the gap might bring uncertainty which at

this scale could lead to a significant error. Figure 6.7 shows a preliminary result of pitch-catch detection on polymer layers. The layers were fabricated by spin coating a solution with different concentrations to have as a result different thicknesses[108]. The coincidence peak on the blue trace represents the arrival time of the pump beam to the pitch transducer. The arrival time of the generated wave on the catch transducer is shown for a series of thicknesses in the green, red, blue and purple traces. There can be seen that the arrival time increases for as the polystyrene layer becomes thicker. This configuration could not only be used to measure mechanical properties, but also for imaging of the gap between the transducers.

Brillouin detection using optical fibres

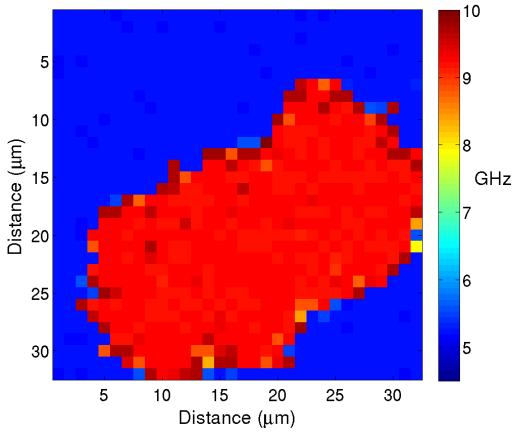

Figure 6.8: Brillouin map obtained in RI configuration. The SNR is not sufficient to obtain a profile of the specimen, but the Brillouin frequency is measurable.

As briefly mentioned in chapter 3, Brillouin detection can be performed in the inverted configuration in reflection (reflection path detection with sample in upside down position). That means that both generation and detection of the Brillouin oscillations can be performed from one side. If a transducer is placed on the cleaved face of a fibre, then the fibre becomes the substrate and Brillouin oscillations could be measured from

whatever is in the vicinity with the fibre tip.

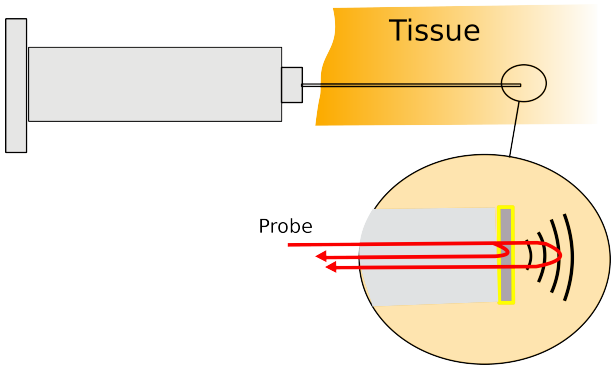

Figure 6.9: Brillouin detection through a optical fibre. inverted reflection configuration allows detection of the Brillouin frequency at the end of a fibre. If the fibre is at the end of a needle, then it could be possible to detect Brillouin oscillations from deep inside a tissue.

Figure 6.8 shows an example of the phantom cell presented in chapter 5 with detection performed in inverted in reflection mode (see chapter 3). Signal to noise ratio is lower than conventional in transmission but, given the configuration, it could be useful to measure the Brillouin frequency in vivo if the fibre is placed inside a needle. Figure 6.9 shows possible configuration for this application. The transducer is deposited on the top of a fibre and then the recaptured light gets to a detector.

It might be difficult to accommodate two distant wavelengths on a single-mode fibre. Also it is possible that the transducer will not attach properly to the fibre and that there is not enough light coupled back to the detector. However, the ability of this application to reach depth with ease could be useful for in-vivo experiments and signals from transducers on the tip of fibres have been successfully achieved by the advanced optics group within the University of Nottingham.

Characterisation of liquids by Brillouin detection

Brillouin scattering is an emerging technology for imaging and characterisation of biological cells. The cells, in most cases, will be surrounded by a liquid which serves

as a medium to keep the cell integrity but also, for imaging purposes, as reference for boundary detection as shown throughout this work. It is of great importance to know beforehand the speed of sound and refractive index of such media to be able to determine the boundaries of a given cell based on Brillouin oscillations. The bulk values of both parameters often differ from those measured using picosecond laser ultrasound or simply have not been reported.

Measuring Brillouin frequencies from a film that is thicker than the penetration depth of the acoustic signal means that it is not possible to calculate the refractive index and speed of sound directly. This means that an assumption has to be made for either parameter. To measure them simultaneously, the Brillouin frequency and its time of flight need to be measured. When the acoustic signal reaches the end of the liquid gap, a distinctive change in Brillouin frequency will indicate the time of flight of the acoustic wave through the gap. For a gap whose thickness is well known, the speed of sound and refractive index can be calculated[118].

To control the size of this gap is not a trivial problem, since the necessary thickness is very small, that requires highly flat surfaces. An opto-acoustic transducer (metallic thin film) also needs to be deposited in order to generate the ultrasound. If this well characterised gap is built based on glass etching and binding technology used commonly in microfluidic chips, then it would be possible to characterise liquids with a single (PLU) measurement (see figure 6.10).

Figure 6.10a shows the proposed microfluidic chip. Two glass wafers are thermally fused. One wafer (1mm thick) has multiple 5μm channels etched on top. A second thin wafer is thermally fused and etched in a central area to a thickness of approximately 5μm where a transducer will be deposited. If Brillouin detection is performed on this transducer (reflection or transmission), the signal will show high frequency (from glass) followed by a lower frequency from the liquid to finally go into high frequency again (see figure 6.10b). The period of time that the Brillouin frequency is lower than glass is then

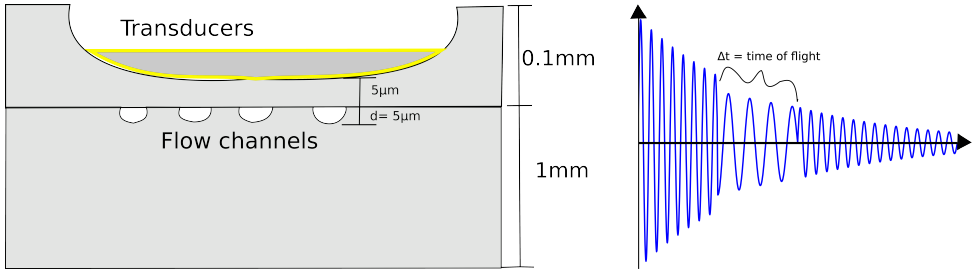

Figure 6.10: Brillouin detection for characterisation of liquids. (a) Transversal view of a proposed microfluidic chip. (b) Expected signal. If a thin(100μm) glass waver is etched down to an approximate 3-5μm in a central region, then the transducer can be deposited on top to have enough penetration depth to travel through the whole liquid gap from inside the flow channels.

the time of flight Δt inside the channel whose thickness d is well known (calibrated by a known liquid). So then the speed of sound becomes ν=$d/\Delta t$. By knowing the speed of sound, the refractive index can be calculated from equation 2.13. The accuracy and sensitivity of this method depends on the number of cycles observed, the signal-to-noise ratio and the error on the estimation of the thickness on the gap in a way that needs to be further investigated.

Spherical transducers

The same concept used to build the transducers can be applied to spherical transducers in the form of nano-shells[119]. Nano-shells consist of an inner dielectric core with a metallic coating with dimensions of the order of ∼50-300nm. The metallic shell serves as the parallel layers of our transducer giving a similar effect. If the shells can be fabricated accurately, it could be possible to optimise the diameter and thickness of the shell for optical detection or generation. The reduced size and spherical symmetry allows these particles to be inserted inside small objects. There is also a lower dependence to incidence angle compared to thin-film transducers.

The shells are challenging subjects since they are barely visible in our system, they

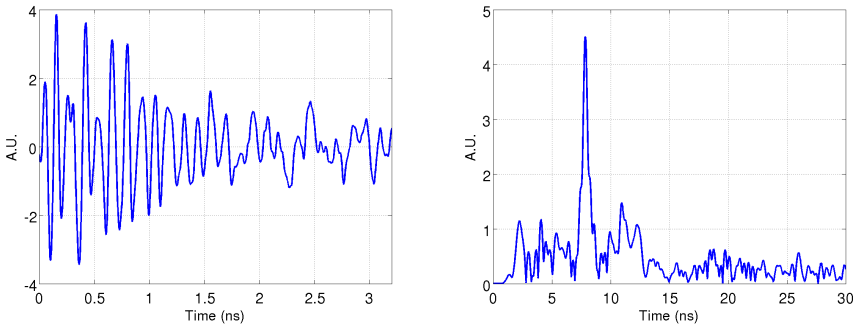

(a) (b)

Figure 6.11: Experimental trace obtained from spherical transducers.(a) Time trace, (b) Fourier transform.

tend to overheat and destroy themselves easily or to modify the matrix around them causing them to move out of the focal spot. Being smaller than the focal spot, signals produced by them are weaker compared to thin-film transducer. Also modelling of such small particles can not be done with a one dimensional Fresnel model.

Nano-shells fabricated in our group were tested as opto-acoustic transducers. Figure 6.11 shows an example trace obtained from 300nm core 20nm nano-shell, where there is a distinctive frequency detected on the particle. Despite their small size the signal-to-noise ratio is comparable to SNR achieved by other picosecond ultrasound measurements on flat surfaces.

Even though is possible to obtain measurements with those particles, there are challenges to be addressed. Repeatability of this kind of measurement is poor probably due to fabrication quality. The shells are difficult to target and seem to be affected rapidly by the lasers. A way of distribute and fix the nano-shells such that repeatable measurements are possible is necessary. This will allow an optimisation process to determine the viability of such structures.

6.7 Quantitative simultaneous measurements of the speed of sound and refractive index

The Brillouin frequency is a combination of optical and mechanical properties. To extract one property, the other must be measured in some other fashion. Assuming constant the refractive index or speed of sound (in x and y) might roughly approximate reality at the scale we are working. Quantitative information of the speed of sound or refractive index with another method can also be measured. Optical extraction of the refractive could be achieved by interferometry [120], however the thickness of the object must be known. Ellipsometry [121] could be used as well but the angles and complex structure of the transducer makes it difficult to implement. To integrate any of those or other methods into our setup means major changes and a challenge just to correlate the information obtained by the Brillouin signals and the alternative method.

Ideally, both parameters should be measured on a single system making it practical. Such goal can be obtained by an alternative way of detection. If the object observed is thin enough so that the Brillouin signal can get through it, two parameters are obtained from such measurement; time of flight and Brillouin frequency. Considering the refractive index $n = \lambda f_B/2\nu$ from equation 2.13 and the speed of sound:

$$\nu = \frac{d}{\Delta t} \tag{6.1}$$

where Δt is the time of flight and d the thickness of the object. Then the refractive index becomes;

$$n = \frac{\lambda f_B}{2\nu} = \frac{\lambda f_B d}{2\Delta t} \tag{6.2}$$

There are still no pure measurements of the refractive index as the thickness of the object is not known. It is possible to untangle the refractive index and speed of

sound from the Brillouin frequency if the thickness of the specimen is measured by another method such as AFM[25] or scanning ion conductive microscope[122]. However, those techniques are not compatible with the optical arrangement proposed here since they require a mechanical approach meaning that the whole characterisation can not be achieved in a single instrument.

An all-opto-acoustic way to measure the thickness of the object can by a kind of the pitch-catch configuration as shown in figure 6.12a. If the speed of sound ν_{media} of the media is known (by, for example, measuring it as proposed in this chapter), then the distance from one transducer to the cell (d_{gap}) and to the substrate (d_{glass}) can be calculated using equation 6.1. The distance from the transducer to the substrate, where the cell is attached, will serve as reference to estimate the thickness of the cell $d_{cell} = d_{glass} - d_{gap}$. This will allow to calculate the refractive index and speed of sound (in x and y) from equations 6.2 and 6.1.

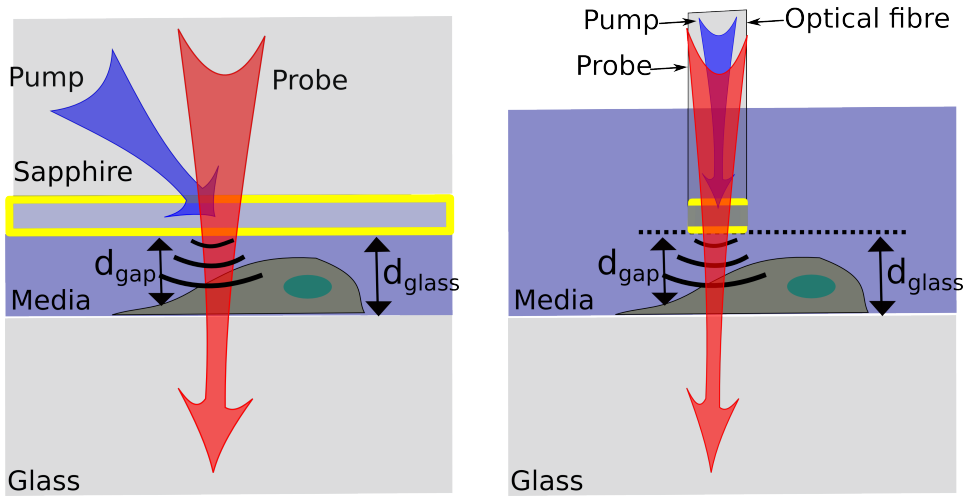

(a) (b)

Figure 6.12: Experimental configuration to calculate thickness, speed of sound and refractive index based on Brillouin detection in transmission. The thickness profile of the object can be calculated by subtracting d_{object} to d_{glass}. (a) Cell between two glass substrates where the sample is scanned. (b) Optical fibre approach where the optical fibre probe is scanned.

Figure 6.12a shows an example of this configuration. The cells are grown on a

regular coverslip and the transducer is approached to the cell vicinity. By resolving in time the changes on transmittance induced by the substrate, media and cell, it should be possible to measure the time of flight and Brillouin frequency from the transducer to the cell (Δt_{gap}), from the transducer from the substrate (Δt_{glass}) and within the cell (Δt_{cell}, see figure 6.13). This will provide with all the information needed to calculate the speed of sound, refractive index and thickness of the cell.

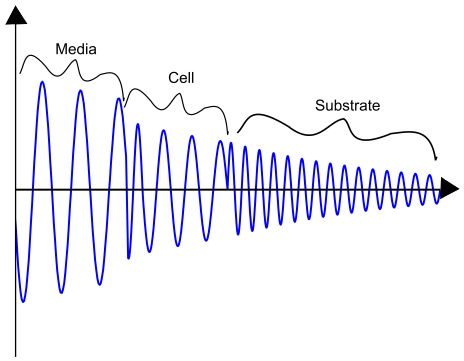

Figure 6.13: Representation of a signal obtained using fibre-based detection. Two of the three Brillouin signatures are known (media and substrate). The third Brillouin signature and time of flight it comes from the cell.

Since the Brillouin frequency can be resolved within the cell, it would be also possible to create three dimensional (3D) maps of the speed of sound and the refractive index by monitoring the Brillouin frequency over time as shown in chapter 5. The accuracy of those 3D measurements depends on the averaged ν values obtained from the time of flight measurements. In any case, if any of the proposed experiments here are successful, then it will be an important achievement.

There are conditions as well as challenges to be addressed for this type of experiment to be successful. The acoustic wave should be strong enough to reach all the way to the glass substrate. The substrate, where the transducer is deposited, needs to be of a different material to the one where the cell is. This allows to differentiate the Brillouin signals from both materials. It will also be difficult to approach the cell with a large flat transducer(like a round coverslip) to form a gap small enough as it is required for

this approach.

It might be possible to replace the objective and free space optics with optical fibres where just the tip of a fibre, with the transducer deposited on it, could be approached by a nano-manipulator. Detection should remain in transmission and in this case the fibre could be scanned rather than the sample (see figure 6.12b). This could be used to measure the profile of larger objects by adding the distance moved by the manipulator to the distance of the gap calculated by measuring the time of flight.

If the time of flight is not known, for example when the cell is too thick, using the thickness measurements (d_{cell}) it could be possible to obtain quantitative measurements of the refractive index and the speed of sound. Instead of measuring the speed of sound based on time of flight, the refractive index could be measured based on phase and thickness measurements. There is a lot of efforts to quantify the phase delay or the refractive index of biological tissue in many forms of phase microscopy [123;124;125;126;127;128] and possibly some of them could be incorporated in our system.

6.8 Summary

There are improvements of the current application that could lead to quantitative simultaneous measurements of the thickness, speed of sound and refractive index maps of biological cells which are of great interest.

Alternative applications of thin-film transducers will make them a versatile device. Some of those applications represent significant challenges. However, those are worth investigating due to the potential they offer. This is an important point since it will allow the potential to unwrap the refractive index and speed of sound from Brillouin measurements, thus creating a true 3D mechanical imaging method.

Chapter 7

Conclusions

In this work it has been demonstrated that picosecond laser ultrasound is compatible for live cell imaging. This offers an alternative to optical fluorescence for live cell imaging in three dimensions. The resultant images have sub-optical in depth resolution and optical lateral resolution offer not only mechanical contrast but information related to the sound velocity.

The study of cell is an important matter, cell research have produced important breakthroughs in the fields of medicine and biology. This has inspired an enormous amount of research. The optical microscope, as the main tool to study cells, has progressed each time with greater capabilities which have lead to new insights into cell biology. However, cells are very challenging objects for study, their microscopic size, little optical contrast, vulnerability and complex nature makes cell research a difficult task.

Alternative imaging and characterisation techniques have been developed for this endeavour. Techniques based on chemical, electrical or mechanical measurements have been reported where each provides additional information to that provided by the optical microscope. Great advancements have been reported in mechanical imaging and characterisation. The mechanical properties of cells are largely unknown and if used as a contrast mechanism it could provide information not obtained before. Techniques like

acoustic, Brillouin or atomic force microscopies are the most important. However those techniques face some limitations. The acoustic microscope can not image cells with sub-optical acoustic wavelengths mainly due to limitations on piezo-electric transducers. Brillouin microscopy has, in principle, optical resolution but is challenging to achieve due to the spontaneous nature of Brillouin scattering. And the atomic force microscope which has reached very high lateral resolution, is still limited to measurements at the surface of the specimens.

Acoustic imaging is a possible path for high-resolution non-destructive imaging of cells. Short wavelength acoustic waves, shorter from that of light, can be radiated into cells without the damaging effects of sub-optical radiation. Picosecond laser based Brillouin oscillations measurements can overcome some of the limitations of the current techniques. As it is an optical technique, it can probe in depth with acoustic resolution and laterally with optical. By using light pulses to produce the acoustic waves, it can generate sound in a very broad bandwidth. Since this acoustic field is coherent, the scattering efficiency is significantly increased. Moreover, the technique is also time-resolved which allows to section in depth with the acoustical wavelength being typically sub-optical. However, images of the Brillouin oscillation frequency on cells had not been reported before this work due to a few reasons. Cell damage induced by the lasers and slow acquisition times limits this technique to single or few measurements on fixed dehydrated specimens.

7.1 Summary of Thesis

Transducer development

To address the problems related to possible Brillouin oscillations measurements on cells, a three layer thin-film transducer in an alternative measuring configuration was proposed. The transducer was set to protect the cell against laser damage while keeping signal amplitudes larger. Based on theoretical and finite elements calculations. A set

of thickness of the layers of 20nm for gold and 140nm for ITO was determined to be the best trade between laser exposure protection (90% for the λ_{pump} and 70% for λ_{probe}), detection levels (30% of input probe power) and fabrication tolerances(+/- 5nm). The transducer in the transmission configuration also offered, acording to models, thermal disipation up to 60% reduction of peak instantaneous temperature and in the case of a sapphire substrate, the long term temperature rise was reduced up to ∼80%.

Experimental setup development

To validate the models, an experimental arrangement based on a ASOPS configuration was used to increase acquisition speed. By having two pulsed laers with 100MHz(pump) and 100.01MHz(probe), it is possible to acquire a trace every 100μs with a 10ns measuring window. This means that it could be possible to aquire up to 10k averages in one second. However, due to limitations in the acquisition system it was possible only to reach about 30% of the maximum capacity having approximately 15k averages in four seconds by capturing half a window (5ns). The system was also flexible enough to allow simultaneous optical, Brightfield, fluorescence and mechanical imaging. It was also designed to reconfigure the path of the pump beam to perform pitch-cath measurements. The imaging was produced by raster scanning the sample with a minimum step size of 100nm. The mechanical stages responsible for this movement were syncronized to the measurement system to allow fully automated image acquisition. The focus and signal quality were stable due to the measurement configuration; the pump beam never saw any defects of highly scattered section as it went always focus into the transducer through the substrate. A special two-coverslip chamber was used to allow light to pass through for detection while allowing the flow of cell media to keep living cells. The flow of the media as controlled by a syringe pump to prevent loss of focus. The signal to noise ratio obtained with this system depends on the amount of pump power applied to the sample and the power level applied at the detector but tipically the measurements

had a SNR of 60-100 giving us the chance to measure signals with modulation depth up to 10^{-4}.

Transducer fabrication and sample preparation

The transducers were fabricated by sputtering and their layers characterised using a custom spectrometric measuring system and model. The calculated thickness of the layers gave a good match to the values obtained by an external company (+/- 2nm). The transducers were deposited on glass or sapphire substrates and were precoated to aid normal cell development. Cells where cultured on the transducers and imaged before confluent to allow the observation of single cells. Based on polystyrene microspheres, own-fabricated cell phantoms where used to perform imaging of the Brillouin oscillations. Such phantoms showed the capabilities of the system and allowed to compare the obtained speed of sound measurements with reported values.

Experimental results

The obtained optical and mechanical measurements from the fabricated transducers matched the models well. Once the models were validated, the approach proposed here was applied to measure Brillouin oscillations from water films. The signals obtained from the films showed good SNR($\sim$60) and modulation depth(10^{-4}). Customised signal processing scripts were used to obtain the Brillouin frequency from the data set obtained on the experiments. The scripts also allowed sectioning of the measured volume by techniques such as short time Fourier transform (STFT) and zero-crossing analysis (ZCA) with resolution varying from one half acoustic wavelength using ZCA on phantom cells to two acoustic wavelengths using STFT on fixed cells.

Cell phantoms

Cell phantoms where used to perform imaging of the Brillouin oscillations. The resultant images showed the Brillouin on polystyrene ($\sim$9GHz) frequency were converted

into speed of sound maps (∼2200m/s). Using also a phantom, capabilities of our method such as depth sectioning, profiling based on zero-cross analysis and the alternative use of the transducer resonance to image the transducer/phantom interface were demonstrated. The height of the phantom was calculated to be approximately 4μm.

Fixed cells

After phantoms, fixed cells where measured. The fixed cells demonstrated the capabilities of the technique to image low contrast Brillouin frequency of an object such as a cell(∼200-500Mhz shift). The measured Brillouin maps showed good correlation with the optical picture where different Brillouin frequencies for different cells were observed. Based also on fixed cells, the sectioning capabilities based on short time Fourier transform analysis to estimate the in-depth location and thickness of thin features was demonstrated. It was found that filopodia was not attached to the transducer and that it thickness was approximately 500nm. This particular result demonstrated that this technique is viable for three dimensional imaging.

Living cells

After fixed cells, measurements were performed on living cells. Living cells imaged using transducers on glass substrates survived only for a few measurements(10) impeding imaging. However, by switching the substrate material from glass to sapphire, cells survived up to 400 measurements in order to produce images. This is a demonstration that picosecond laser ultrasound is biocompatible for live-cell imaging and it is of great importance given the difficulty to increase the resolution of mechanical imaging in the life sciences.

A cell was also being measured as it died (1600 measurements) resulting in a reduction of the Brillouin frequency over time not observed on living cells(from 5.6 to 5.3GHz). This change in frequency is probably originated because the cell was experiencing apoptosis. This results is the first of its kind and it is a good demonstration of

the potential of this technique.

The contrast obtained for living cells (that did not survived) on a glass substrate were similar to those obtained on a fixed cell. However, switching the substrate to sapphire showed less cell inner detail. This difference could be due to the different substrate leaking more acoustic energy or due to the unaffected cell state. With the use of sapphire substrate, it is demonstrated that along with light exposure, heat is also a strong damaging factor of cells undergoing PLU measurements.

7.2 Closing remarks

The importance of this work resides in the demonstration that picosecond laser ultrasound is viable for living cell imaging. And since PLU offers advantages over other mechanical imaging techniques in terms of speed, signal amplitude, penetration depth and resolution. The approach presented here has the potential to provide new insights in cell biology.

The work presented here has been reviewed by institutions like the Acoustical Society of America[88] and the Optical Society of america[129]. Moreover, it has been presented in multiple conferences(LU2013 and 2015, AFPAC2013 and 2015, SPIE 8923) and there are more manuscripts in preparation.

Appendix

A.1 Acoustics and ultrasound

Acoustics is the science of mechanical wave motion in gases, liquids and solids. The mechanical wave motion is the transmission of energy through a material. An input of energy in the form of a rapid change on the pressure in a material launches a wave that we know as sound. The acoustic spectrum is very broad having 4 main regions; infrasound (<20Hz), sound (20Hz-20kHz), ultrasound (20kHz - ∼40GHz) and phonons (> ∼40GHz). The first three (up to low GHz region) can be treated as classical mechanics which is the scope of this work. Is not clear at which frequency classical modelling does not follow the experimental observations but as seen above, at f ∼5-14GHz a good match is observed.

When pressure is applied in the surface of a material, the energy is transmitted by one molecule exerting pressure to the adjacent one and so on. These waves are called compression waves since the particle movement is parallel to travel direction (longitudinal waves). Fluid can only support this kind of waves since it is possible to compress a fluid but not pull it. Since molecules in a solid have strong bonds, a solid can support compression and also shear waves. On a shear wave the particles move perpendicular to the direction of propagation (transverse waves). Sound waves can resonate to create a tone or can be transmitted, reflected or diffracted in a similar way to any other wave.

Sound attenuation in a fluid (air for example) is very high for ultrasound. So this range is normally used in solid materials or tissue. Ultrasound is commonly used as a tool for non-destructive imaging, characterization and measurement of materials. The capacity of ultrasound to propagate on opaque materials and the relationship of the speed of sound to the mechanical properties of the medium of propagation makes ultrasound a very versatile tool with many applications. Is the interest of this section to describe some of the concepts related to sound . The speed of sound ν is defined as speed at which the displacement of the particles propagates through medium and this depends on materials properties. For longitudinal waves can be expressed as:

$$\nu = \sqrt{\frac{K}{\rho}}$$

where K is the bulk modulus (a measure of a material stiffness) and ρ the density of the material. Greater bulk modulus means higher speed of sound.

In solids sound can propagate longitudinally (compression wave) but transversally as well(shear waves, among other types of waves not mentioned here). If the lateral area of the medium where the sound propagates is large in comparison with the acoustical wavelength, then only transversal waves are considered in a one dimensional case and the sound speed is expressed as:

$$\nu = \sqrt{\frac{\mathfrak{E}}{\rho}}$$

where $\mathfrak{E}$ is the Young's modulus (a measure of the elasticity of a material) and ρ the density. When a pressure p is applied to a surface, the particle involved in propagating the sound moves to certain velocity $\mathfrak{v}$ called the particle velocity, the relation of these parameters is called (for the one dimension case) the characteristic acoustic impedance

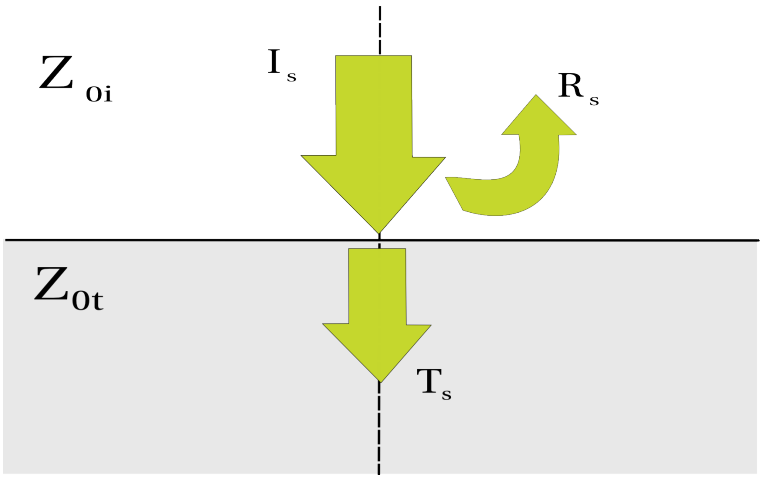

Figure A.1: Reflection and transmission of compression waves on a material interface. The amplitude of the reflected and transmitted waves depend on the characteristic impedance of both materials materials

and it is given by:

$$Z_0 = \frac{p}{\mathfrak{v}}$$

which is related to the bulk modulus and the speed of sound as:

$$Z_0 = \rho\nu = \sqrt{K\rho}$$

and to sound intensity as:

$$I_s = p\mathfrak{v} = \mathfrak{v}^2 Z_0$$

Acoustic impedance provides also a measure of the acoustic transmitted T_s and reflected R_s amplitudes of waves travelling normally through an interface as (see figure

A.1):

$$R_s = (\frac{Z_{01} - Z_{02}}{Z_{01} + Z_{02}})^2$$

and

$$T_s = \frac{4Z_{01}Z_{02}}{(Z_{01} + Z_{02})^2}$$

If $Z_{01} = Z_{02}$, then the transmission of sound is maximum while reflection minimum. If Z_{01} and Z_{02} are different, a reflection occurs and less energy is transmitted. For this reason impedance matching or mismatching materials are used to minimize reflections (coupling gel for example) or to increase them (as insulators). For the common case where sound needs to be transmitted to a load with different impedance, the coupling media should have a impedance given by:

$$Z_{0m} = \sqrt{Z_{01}Z_{02}}$$

Which will provide maximum transmission of sound given impedances Z_{01} and $Z_0 2$ [130]. Similar to the optical case, sound also gets attenuated as it propagates though media. This loss of power is expressed as:

$$I_s(x) = I_{0s}e^{\alpha_s x}$$

where x is the propagation distance and α_s is the attenuation coefficient which is a material property that strongly depends on frequency.

Ultrasound is used in many different ways, for imaging, non destructive testing or simply to 'shake' solutions (see chapter 2). The main technology to generate and detect ultrasound it is based on the piezoelectric effect. Which is the generation of a electric voltage due to a change in pressure. The effect works in the inverse way; where a voltage change induces a change in material size which if in contact with another

material launches an acoustic wave.

A.2 Diffraction

Diffraction is the interaction of waves and obstructions. The geometrical theory of light states that light travels in straight lines, however light leaves a small shadow made up of bright and dark regions that is not expected from geometrical optics but it is a common wave phenomena. This distribution of energy is commonly referred as the diffraction pattern.

So every obstruction or abrupt change in propagation media like opacity or refractive index will cause diffraction. There is no physical distinction of diffraction and interference since both are base on the superposition principle. However it has become customary to distinct interference from diffraction in the basis that diffraction handles normally a large number of waves in cases were light is obstructed.

Diffraction from a circular aperture is of great relevance in optical instrumentation because every image point on a microscope, telescope or camera, will generate a diffraction pattern on the screen rather than a perfect image of the object. For a camera taking a portrait picture, this pattern is really neglectable. However, if the magnification is increased for example in a microscope or telescope, the diffraction patter will be magnified as well meaning that the size of the image of a small object is limited by the diffraction pattern created while travelling though the optical instrumentation. Then in the case of two small objects close together, we can only resolve them as individual objects if their airy discs are far enough apart.

The Rayleigh criterion for maximum resolution is an arbitrary but useful criterion since states that two point objects (i.e. remote stars on a telescope) are resolved when the centres are separated by the radius central region of the diffraction pattern (normally known as Airy disc). In this criterion , the maximum of the pattern of one

object falls into the minimum of the other.

The first minimum of the diffraction pattern of a circular aperture is given by the Bessel function when $\gamma = 3.832 = \frac{kDsin\theta}{2}$ and for small angles can be written as:

$$\theta_{min} = 3.832\frac{2}{kD} \cong 1.22\frac{\lambda}{D}$$

giving an expression for the angular resolution of optical instrumentation where D is the diameter of the objective aperture and λ the optical wavelength. In a typical infinity corrected optical microscope, the objects are placed in the focal plane of the microscope objective, therefore using small angle approximations the spatial resolution is given by:

$$\boxed{x_{min} \cong 1.22\frac{\lambda}{D}f_{objective}}$$

Defining the numerical aperture of a lens as $NA = nsin\theta \cong n\frac{D}{2f_{objective}}$ the resolution of a microscope immersed in air can be rewritten as:

$$\boxed{x_{min} \cong 1.22\frac{\lambda}{2NA} \cong 0.61\frac{\lambda}{NA}}$$

Similarly, this equation can be used to approximately calculate a laser spot diameter if the aperture is completely filled, so the laser spot diameter is approximately given by:

$$\boxed{D_{spot} \cong 1.22\frac{\lambda}{NA}}$$

A.3 Optical attenuation and skin depth

Waves travelling in any type of material experience attenuation due to absorption or scattering. Absorption happens when the energy of a wave is transferred to the media and most of the time attenuated as thermal energy. Scattering in the other hand only

changes the direction of travel of propagation of the media splitting it from the main beam. Attenuation can be very small like in the case of dielectrics or very high like in the case of metals. To include this effect in the propagation of a wave, the propagation constant is defined as complex $k = k_R + k_I$. Inserting this in the expression for the one dimension harmonic plane wave we have:

$$\mathbf{E} = E_0 e^{i(k_R x + k_I x - wt)} = E_0 e^{-k_I x} e^{k_R x - wt}$$

calculating the irradiance then we obtain:

$$I(x) = I e^{-\alpha x}$$

where $\alpha = 2k_I$ and is called the absorption coefficient of the medium which, like the refractive index, it needs to be measured or in some cases deducted theoretically. The exponential factor will reduce the irradiance of the wave as it travels along x. If the propagation constant is complex, then the refractive index it is complex as well:

$$n = n_R + n_I$$

where n_R is the usual refractive index and n_I is called the extinction coefficient and is related to the attenuation coefficient α as:

$$\alpha = 2k_I = 2k_0 n_I = \frac{4\pi n_I}{\lambda_0}$$

where k_0 is the propagation constant of vacuum. When the wave has travelled $x = 1/k_I$ means that the amplitude of the wave has been attenuated by a factor of $e^{-1} = 0.36$ and the irradiance with a factor of $e^{-2} = 0.13$ of its value at the surface. This distance

is called skin depth and its given by:

$$\boxed{\delta_p = \frac{2}{\alpha} = \frac{\lambda_0}{2\pi n_I}}$$

The skin depth is a useful parameter to estimate how deep the light travels within a highly absorbent materials such as metals. This is particularly useful to estimate the thickness necessary to absorb a light pulse to generate ultrasound.

References

[1] Stephen L. Wolfe. *Introduction to cell biology*. Wadsworth Publishing Company, 1983. 1

[2] Robert Hooke. *Micrographia*. Dover Phoenix editions, 2003. 3

[3] Richard Creese. The Leeuwenhoek Legacy, October 1992. 3

[4] Jeffrey C. Pommerville. *Fundamentals of Microbiology*. Jones & Bartlett Publishers, 2013. 3

[5] G. G. Rose. Phase contrast observations of the endoplasmic reticulum in living tissue cultures. *The Journal of Cell Biology*, 8(2):423–430, October 1960. 4

[6] Armen R Kherlopian, Ting Song, Qi Duan, Mathew A Neimark, Ming J Po, John K Gohagan, and Andrew F Laine. A review of imaging techniques for systems biology. *BMC systems biology*, 2(1):74, January 2008. 5

[7] F. Zernike. Phase contrast, a new method for the microscopic observation of transparent objects. *Physica*, 9(7):686–698, July 1942. 5

[8] M. Abercrombie and E.J. Ambrose. Interference microscope studies of cell contacts in tissue culture. *Experimental Cell Research*, 15(2):332–345, October 1958. 5

[9] David M. Shotton. Confocal scanning optical microscopy and its applications for biological specimens. *J. Cell Sci.*, 94(2):175–206, October 1989. 5

[10] Jeff W Lichtman and José-Angel Conchello. Fluorescence microscopy. *Nature methods*, 2(12):910–9, December 2005. 5

[11] Graeme Ball, Richard M Parton, Russell S Hamilton, and Ilan Davis. *A cell biologist's guide to high resolution imaging.*, volume 504. Elsevier Inc., 1 edition, January 2012. 5, 7

[12] M Chalfie, Y Tu, G Euskirchen, W. Ward, and D. Prasher. Green fluorescent protein as a marker for gene expression. *Science*, 263(5148):802–805, February 1994. 5

[13] Luc S. De Clerck, Chris H. Bridts, Annemie M. Mertens, Marleen M. Moens, and Wim J. Stevens. Use of fluorescent dyes in the determination of adherence of human leucocytes to endothelial cells and the effect of fluorochromes on cellular function. *Journal of Immunological Methods*, 172(1):115–124, June 1994. 6

[14] Ram Dixit and Richard Cyr. Cell damage and reactive oxygen species production induced by fluorescence microscopy: effect on mitosis and guidelines for non-invasive fluorescence microscopy. *The Plant Journal*, 36(2):280–290, October 2003. 6

[15] Ludwig Reimer and Helmut Kohl. *Transmission Electron Microscopy: Physics of Image Formation*. Springer Science & Business Media, 2008. 6

[16] Richard McIntosh, Daniela Nicastro, and David Mastronarde. New views of cells in 3D: an introduction to electron tomography. *Trends in cell biology*, 15(1):43–51, January 2005. 6

[17] Birka Hein, Katrin I Willig, and Stefan W Hell. Stimulated emission depletion (STED) nanoscopy of a fluorescent protein-labeled organelle inside a living cell. *Proceedings of the National Academy*

of Sciences of the United States of America, 105(38):14271–6, September 2008. 7, 8

[18] Michael J Rust, Mark Bates, and Xiaowei Zhuang. Sub-diffraction-limit imaging by stochastic optical reconstruction microscopy (STORM). *Nature methods*, 3(10):793–5, October 2006. 7, 8

[19] U Valentin Nägerl, Katrin I Willig, Birka Hein, Stefan W Hell, and Tobias Bonhoeffer. Live-cell imaging of dendritic spines by STED microscopy. *Proceedings of the National Academy of Sciences of the United States of America*, 105(48):18982–7, December 2008. 8

[20] Teresa Klein, Anna Löschberger, Sven Proppert, Steve Wolter, Sebastian van de Linde, and Markus Sauer. Live-cell dSTORM with SNAP-tag fusion proteins. *Nature methods*, 8(1):7–9, January 2011. 8

[21] Bo Huang, Wenqin Wang, Mark Bates, and Xiaowei Zhuang. Three-dimensional super-resolution imaging by stochastic optical reconstruction microscopy. *Science (New York, N.Y.)*, 319(5864):810–3, February 2008. 8, 9

[22] U. Dammer, O. Popescu, P. Wagner, D. Anselmetti, H. Guntherodt, and G. Misevic. Binding strength between cell adhesion proteoglycans measured by atomic force microscopy. *Science*, 267(5201):1173–1175, February 1995. 9, 11

[23] Tatyana G Kuznetsova, Maria N Starodubtseva, Nicolai I Yegorenkov, Sergey A Chizhik, and Renat I Zhdanov. Atomic force microscopy probing of cell elasticity. *Micron (Oxford, England : 1993)*, 38(8):824–33, January 2007. 9, 11

[24] R M Hochmuth. Micropipette aspiration of living cells. *Journal of biomechanics*, 33(1):15–22, January 2000. 9, 10

[25] Manfred Radmacher. *Atomic Force Microscopy in Cell Biology*, volume 68 of *Methods in Cell Biology*. Elsevier, 2002. 9, 16, 154

[26] Hu Zhang and Kuo-Kang Liu. Optical tweezers for single cells. *Journal of the Royal Society, Interface / the Royal Society*, 5(24):671–90, July 2008. 9, 11

[27] J A Hildebrand, D Rugar, R N Johnston, and C F Quate. Acoustic microscopy of living cells. *Proceedings of the National Academy of Sciences of the United States of America*, 78(3):1656–60, March 1981. 9, 12, 13, 71, 127

[28] Giuliano Scarcelli, Sabine Kling, Elena Quijano, Roberto Pineda, Susana Marcos, and Seok Hyun Yun. Brillouin microscopy of collagen crosslinking: noncontact depth-dependent analysis of corneal elastic modulus. *Investigative ophthalmology & visual science*, 54(2):1418–25, February 2013. 9

[29] D. P. Theret. Application of the Micropipette Technique to the Measurement of Cultured Porcine Aortic Endothelial Cell Viscoelastic Properties. *Journal of Biomechanical Engineering*, 112(3):263, March 2008. 10

[30] D. Karabacak, T. Kouh, C. C. Huang, and K. L. Ekinci. Optical knife-edge technique for nanomechanical displacement detection. *Applied Physics Letters*, 88(19):193122, May 2006. 11, 22

[31] M. Lekka, J. Lekki, M. Marszaek, P. Golonka, Z. Stachura, B. Cleff, and A.Z. Hrynkiewicz. Local elastic properties of cells studied by SFM. *Applied Surface Science*, 141(3-4):345–349, March 1999. 11

[32] Hong Xing You, Joan M. Lau, Shengwen Zhang, and Lei Yu. Atomic force microscopy imaging of living cells: a preliminary study of the disruptive effect of the cantilever tip on cell morphology. *Ultramicroscopy*, 82(1-4):297–305, February 2000. 11, 17

[33] A. Ashkin. Acceleration and Trapping of Particles by Radiation Pressure. *Physical Review Letters*, 24(4):156–159, January 1970. 11

[34] J Sleep, D Wilson, R Simmons, and W Gratzer. Elasticity of the red cell membrane and its

relation to hemolytic disorders: an optical tweezers study. *Biophysical journal*, 77(6):3085–95, December 1999. 11

[35] S Hénon, G Lenormand, A Richert, and F Gallet. A new determination of the shear modulus of the human erythrocyte membrane using optical tweezers. *Biophysical journal*, 76(2):1145–51, February 1999. 11

[36] Schanila Nawaz, Paula Sánchez, Kai Bodensiek, Sai Li, Mikael Simons, and Iwan A T Schaap. Cell visco-elasticity measured with AFM and optical trapping at sub-micrometer deformations. *PloS one*, 7(9):e45297, January 2012. 11

[37] Ernst-Ludwig Florin, Arnd Pralle, J.K. Heinrich Hörber, and Ernst H.K. Stelzer. Photonic Force Microscope Based on Optical Tweezers and Two-Photon Excitation for Biological Applications. *Journal of Structural Biology*, 119(2):202–211, July 1997. 11

[38] Erik Fällman, Staffan Schedin, Jana Jass, Magnus Andersson, Bernt Eric Uhlin, and Ove Axner. Optical tweezers based force measurement system for quantitating binding interactions: system design and application for the study of bacterial adhesion. *Biosensors and Bioelectronics*, 19(11):1429–1437, June 2004. 11

[39] Timo A Nieminen, Vincent L Y Loke, Alexander B Stilgoe, Gregor Knöner, Agata M Braczyk, Norman R Heckenberg, and Halina Rubinsztein-Dunlop. Optical tweezers computational toolbox. *Journal of Optics A: Pure and Applied Optics*, 9(8):S196–S203, August 2007. 11

[40] Carol B. Benson, Peter H. Arger, and Edward I. Bluth. *Ultrasound in Obstetrics and Gynecology: A Practical Approach*. Thieme, 2000. 12

[41] R. J. Dewhurst, C. Edwards, A. D. W. McKie, and S. B. Palmer. Estimation of the thickness of thin metal sheet using laser generated ultrasound. *Applied Physics Letters*, 51(14):1066, October 1987. 12

[42] Jens Becker, Laurence J. Jacobs, and Jianmin Qu. Characterization of Cement-Based Materials Using Diffuse Ultrasound. *Journal of Engineering Mechanics*, November 2003. 12

[43] T. Kundu, J. Bereiter-Hahn, and K. Hillmann. Measuring elastic properties of cells by evaluation of scanning acoustic microscopy V(Z) values using simplex algorithm. *Biophysical Journal*, 59(6):1194–1207, June 1991. 13

[44] T Kundu, J Bereiter-Hahn, and I Karl. Cell property determination from the acoustic microscope generated voltage versus frequency curves. *Biophysical journal*, 78(5):2270–9, May 2000. 13

[45] Eike Weiss, Pavlos Anastasiadis, Gotz Pilarczyk, Robert Lemor, and Pavel Zinin. Mechanical Properties of Single Cells by High-Frequency Time-Resolved Acoustic Microscopy. *IEEE Transactions on Ultrasonics, Ferroelectrics and Frequency Control*, 54(11):2257–2271, November 2007. 13

[46] B. Hadimioglu. Water acoustic microscopy at suboptical wavelengths. *Applied Physics Letters*, 43(11):1006, December 1983. 13

[47] M. S. Muha, A. A. Moulthrop, G. C. Kozlowski, and B. Hadimioglu. Acoustic microscopy at 15.3 GHz in pressurized superfluid helium. *Applied Physics Letters*, 56(11):1019, 1990. 13

[48] J. Heiserman. Cryogenic acoustic microscopy. *The Journal of the Acoustical Society of America*, 67(5):1629, May 1980. 13

[49] Giuliano Scarcelli and Seok Hyun Yun. Confocal Brillouin microscopy for three-dimensional mechanical imaging. *Nature photonics*, 2(1):39–43, December 2007. 13, 14

[50] R Sanctuary, Ravi Bactavatchalou, Ulrich Müller, W Possart, P Alnot, and J K Krüger. Acoustic profilometry within polymers as performed by Brillouin microscopy. *Journal of Physics D: Applied Physics*, 36(21):2738–2742, November 2003. 14

[51] U Müller, R Bactavatchalou, J Baller, M Philipp, R Sanctuary, B Zielinski, P Alnot, W Possart,

and J K Krüger. Acoustic profilometry of interphases in epoxy due to segregation and diffusion using Brillouin microscopy. *New Journal of Physics*, 10(2):023031, February 2008. 14

[52] Rainer G. Ulbrich and Claude Weisbuch. Resonant Brillouin Scattering of Excitonic Polaritons in Gallium Arsenide. *Physical Review Letters*, 38(15):865–868, April 1977. 14

[53] R. HARLEY, D. JAMES, A. MILLER, and J. W. WHITE. Phonons and the elastic moduli of collagen and muscle. *Nature*, 267(5608):285–287, May 1977. 14

[54] Masanori Sakamoto, Masahiko Kawabe, Mami Matsukawa, Noriko Koizumi, and Norikazu Ohtori. Measurement of Wave Velocity in Bovine Bone Tissue by Micro-Brillouin Scattering. *Japanese Journal of Applied Physics*, 47(5):4205–4208, May 2008. 14

[55] Stephan Reiß, Gerolf Burau, Oliver Stachs, Rudolf Guthoff, and Heinrich Stolz. Spatially resolved Brillouin spectroscopy to determine the rheological properties of the eye lens. *Biomedical optics express*, 2(8):2144–59, August 2011. 14

[56] Giuliano Scarcelli, Pilhan Kim, and Seok Hyun Yun. In vivo measurement of age-related stiffening in the crystalline lens by Brillouin optical microscopy. *Biophysical journal*, 101(6):1539–45, September 2011. 14

[57] F Palombo, M Madami, N Stone, and D Fioretto. Mechanical mapping with chemical specificity by confocal Brillouin and Raman microscopy. *The Analyst*, 139(4):729–33, February 2014. 14, 15

[58] Pierre Parot, Yves F Dufrêne, Peter Hinterdorfer, Christian Le Grimellec, Daniel Navajas, Jean-Luc Pellequer, and Simon Scheuring. Past, present and future of atomic force microscopy in life sciences and medicine. *Journal of molecular recognition : JMR*, 20(6):418–31, January 2007. 16

[59] F A Schabert, C Henn, and A Engel. Native Escherichia coli OmpF porin surfaces probed by atomic force microscopy. *Science (New York, N.Y.)*, 268(5207):92–4, April 1995. 16

[60] W Han, J Mou, J Sheng, J Yang, and Z Shao. Cryo atomic force microscopy: a new approach for biological imaging at high resolution. *Biochemistry*, 34(26):8215–20, July 1995. 16

[61] M. Rief. Reversible Unfolding of Individual Titin Immunoglobulin Domains by AFM. *Science*, 276(5315):1109–1112, May 1997. 16

[62] Z Shao, J Yang, and A P Somlyo. Biological atomic force microscopy: from microns to nanometers and beyond. *Annual review of cell and developmental biology*, 11:241–65, January 1995. 16

[63] C. Thomsen, H.T. Grahn, H.J. Maris, and J. Tauc. Picosecond interferometric technique for study of phonons in the brillouin frequency range. *Optics Communications*, 60(1):55–58, 1986. 17, 28

[64] C. Thomsen, J. Strait, Z. Vardeny, H. Maris, J. Tauc, and J. Hauser. Coherent Phonon Generation and Detection by Picosecond Light Pulses. *Physical Review Letters*, 53(10):989–992, September 1984. 17, 22, 28, 29, 34, 86

[65] C. Rossignol, N. Chigarev, M. Ducousso, B. Audoin, G. Forget, F. Guillemot, and M. C. Durrieu. In Vitro picosecond ultrasonics in a single cell. *Applied Physics Letters*, 93(12):123901, September 2008. 17, 34, 38, 39, 46, 111

[66] B. Audoin, C. Rossignol, N. Chigarev, M. Ducousso, G. Forget, F. Guillemot, and M.C. Durrieu. Picosecond acoustics in vegetal cells: Non-invasive in vitro measurements at a sub-cell scale. *Ultrasonics*, 50(2):202–207, 2010. 18, 39, 71, 135

[67] Paul A Elzinga, Fred E. Lytle, Yanan Jian, Galen B. King, and Normand M. Laurendeau. Pump/Probe Spectroscopy by Asynchronous Optical Sampling. *Appl. Spectrosc.*, 41(1):2–4, 1987. 19, 84

[68] A A Maznev, Kara J Manke, Kung-Hsuan Lin, Keith A Nelson, Chi-Kuang Sun, and Jen-Inn Chyi. Broadband terahertz ultrasonic transducer based on a laser-driven piezoelectric semiconductor superlattice. *Ultrasonics*, 52(1):1–4, January 2012. 22

[69] S D Sharples, R A Light, S O Achamfuo-Yeboah, M Clark, and M G Somekh. The SKED: speckle knife edge detector. *Journal of Physics: Conference Series*, 520(1):012004, June 2014. 22, 31

[70] J.-P. Monchalin. Optical detection of ultrasound. *IEEE Transactions on Ultrasonics*, pages 485–499, 1986. 22

[71] T Stratoudaki, J A Hernandez, M Clark, and M G Somekh. Cheap optical transducers (CHOTs) for narrowband ultrasonic applications. *Measurement Science and Technology*, 18(3):843–851, March 2007. 22, 27, 28, 34

[72] F. E. Lytle, R. M. Parrish, and W. T. Barnes. An Introduction to Time-Resolved Pump/Probe Spectroscopy. *Appl. Spectrosc.*, 39(3):444–451, 1985. 23, 83

[73] C. Thomsen, H. Grahn, H. Maris, and J. Tauc. Surface generation and detection of phonons by picosecond light pulses. *Physical Review B*, 34(6):4129–4138, September 1986. 26, 34, 90

[74] Osamu Matsuda, Maria Cristina Larciprete, Roberto Li Voti, and Oliver B Wright. Fundamentals of picosecond laser ultrasonics. *Ultrasonics*, 56:3–20, February 2015. 26

[75] O. Matsuda and O. B. Wright. Reflection and transmission of light in multilayers perturbed by picosecond strain pulse propagation. *Journal of the Optical Society of America B*, 19(12):3028, December 2002. 27

[76] P. Babilotte, P. Ruello, D. Mounier, T. Pezeril, G. Vaudel, M. Edely, J-M. Breteau, V. Gusev, and K. Blary. Femtosecond laser generation and detection of high-frequency acoustic phonons in GaAs semiconductors. *Physical Review B*, 81(24):245207, June 2010. 28, 38

[77] C. Rossignol. Nondestructive evaluation of micrometric diamond films with an interferometric picosecond ultrasonics technique. *Journal of Applied Physics*, 95(8):4157, March 2004. 28, 38

[78] C.B Scruby and L.E Drain. *Laser Ultrasonics Techniques and Applications*. CRC Press, 1990. 28

[79] Serguei Stepanov and Fernando Pérez Cota. Transient two-wave mixing in a linear configuration of an adaptive interferometer based on Er-doped fiber with saturable absorption. *Optics Letters*, 32(17):2532, 2007. 30

[80] R. K. Ing and J.-P. Monchalin. Broadband optical detection of ultrasound by two-wave mixing in a photorefractive crystal. *Applied Physics Letters*, 59(25):3233, December 1991. 30

[81] Jean-Pierre Monchalin. Optical detection of ultrasound at a distance using a confocal FabryPerot interferometer. *Applied Physics Letters*, 47(1):14, July 1985. 30

[82] Julien Higuet, Tony Valier-Brasier, Thomas Dehoux, and Bertrand Audoin. Beam distortion detection and deflectometry measurements of gigahertz surface acoustic waves. *The Review of scientific instruments*, 82(11):114905, November 2011. 31

[83] Eugene Hecht. *Optics*. Pearson Education, Limited, 2013. 32

[84] Frank L. Pedrotti and Leno S. Pedrotti. *Introduction to Optics*. Prentice Hall, 1993. 32

[85] Paul Beard Edward Zhang. Broadband ultrasound field mapping system using a wavelength tuned, optically scanned focussed beam to interrogate a Fabry Perot polymer film sensor. *IEEE Trans. Ultrason. Ferroelectr. Freq. Control*, 2006. 33

[86] Edward Zhang, Jan Laufer, and Paul Beard. Backward-mode multiwavelength photoacoustic scanner using a planar Fabry-Perot polymer film ultrasound sensor for high-resolution three-dimensional imaging of biological tissues. *Applied Optics*, 47(4):561, 2008. 33

[87] Y. Li, Q. Miao, A. V. Nurmikko, and H. J. Maris. Picosecond ultrasonic measurements using an optical cavity. *Journal of Applied Physics*, 105(8):083516, April 2009. 33

[88] Richard J. Smith, Fernando Perez Cota, Leonel Marques, Xuesheng Chen, Ahmet Arca, Kevin Webb, Jonathon Aylott, Micheal G. Somekh, and Matt Clark. Optically excited nanoscale ul-

trasonic transducers. *The Journal of the Acoustical Society of America*, 137(1):219–227, January 2015. 33, 41, 75, 113, 143, 162

[89] Gary L. Eesley, Bruce M. Clemens, and Carolyn A. Paddock. Generation and detection of picosecond acoustic pulses in thin metal films. *Applied Physics Letters*, 50(12):717, 1987. 34

[90] Hirotsugu Ogi, Tomohiro Shagawa, Nobutomo Nakamura, Masahiko Hirao, Hidefumi Odaka, and Naoto Kihara. Elastic-Constant Measurement in Oxide and Semiconductor Thin Films by Brillouin Oscillations Excited by Picosecond Ultrasound. *Japanese Journal of Applied Physics*, 48(7):07GA01, July 2009. 34, 46

[91] Yannick Guillet, Bertrand Audoin, Mélanie Ferrié, and Serge Ravaine. All-optical ultrafast spectroscopy of a single nanoparticle-substrate contact. *Physical Review B*, 86(3):035456, July 2012. 34

[92] Thomas Dehoux, Nicolas Tsapis, and Bertrand Audoin. Relaxation dynamics in single polymer microcapsules probed with laser-generated GHz acoustic waves. *Soft Matter*, 8(9):2586, February 2012. 34, 38

[93] Damien Segur, Alexander Shuvalov, Yong Dong Pan, Nikolay Chigarev, Clément Rossignol, and Bertrand Audoin. Acoustic waves generated by a laser point pulse in a micrometric fiber. *The Journal of the Acoustical Society of America*, 123(5):3157, May 2008. 34

[94] T. Dehoux and B. Audoin. Non-invasive optoacoustic probing of the density and stiffness of single biological cells. *Journal of Applied Physics*, 112(12):124702, December 2012. 39, 40

[95] Mathieu Ducousso, Omar El-Farouk Zouani, Christel Chanseau, Céline Chollet, Clément Rossignol, Bertrand Audoin, and Marie-Christine Durrieu. Evaluation of mechanical properties of fixed bone cells with sub-micrometer thickness by picosecond ultrasonics. *The European Physical Journal Applied Physics*, 61(1):11201, January 2013. 40

[96] Bertrand Audoin Atef Gadalla, Thomas Dehoux. Tranverse mechanical properties of cel walls of single living plant cells probed by laser-generated acoustic waves. *Planta*, 239:1129–1137, March 2014. 41

[97] Katsufumi Uehara, Hirotsugu Ogi, and Masahiko Hirao. Enhancement of ultrahigh-frequency vibration of an Au/Si 3 N 4 composite resonator with picosecond ultrasound. *Applied Physics Express*, 7(2):025201, February 2014. 41

[98] Thomas Dehoux, Maroun Abi Ghanem, Omar F Zouani, Mathieu Ducousso, Nikolay Chigarev, Clément Rossignol, Nicolas Tsapis, Marie-Christine Durrieu, and Bertrand Audoin. Probing single-cell mechanics with picosecond ultrasonics. *Ultrasonics*, August 2014. 41

[99] T Dehoux, M Abi Ghanem, O F Zouani, J-M Rampnoux, Y Guillet, S Dilhaire, M-C Durrieu, and B Audoin. All-optical broadband ultrasonography of single cells. *Scientific reports*, 5:8650, January 2015. 42, 113, 130

[100] Sorasak Danworaphong, Motonobu Tomoda, Yuki Matsumoto, Osamu Matsuda, Toshiro Ohashi, Hiromu Watanabe, Masafumi Nagayama, Kazutoshi Gohara, Paul H. Otsuka, and Oliver B. Wright. Three-dimensional imaging of biological cells with picosecond ultrasonics. *Applied Physics Letters*, 106(16):163701, April 2015. 42, 43

[101] P. A. Mante, J. F. Robillard, and A. Devos. Complete thin film mechanical characterization using picosecond ultrasonics and nanostructured transducers: experimental demonstration on SiO[sub 2]. *Applied Physics Letters*, 93(7):071909, 2008. 46

[102] Charalambos C. Katsidis and Dimitrios I. Siapkas. General Transfer-Matrix Method for Optical Multilayer Systems with Coherent, Partially Coherent, and Incoherent Interference. *Applied Optics*, 41(19):3978, July 2002. 55

[103] J. P. Colinge. Laser light absorption in multilayers. *Journal of Applied Physics*, 52(7):4769, jul 1981. 58

[104] P. B. Johnson and R. W. Christy. Optical Constants of the Noble Metals. *Physical Review B*, 6(12):4370–4379, December 1972. 60

[105] K. König, P. T. C. So, W. W. Mantulin, and E. Gratton. Cellular response to near-infrared femtosecond laser pulses in two-photon microscopes. *Optics Letters*, 22(2):135, January 1997. 71, 73, 130

[106] S Tornaletti and G P Pfeifer. UV damage and repair mechanisms in mammalian cells. *BioEssays : news and reviews in molecular, cellular and developmental biology*, 18(3):221–8, March 1996. 71

[107] C.M. Gedik, S.W.B. Ewen, and A.R. Collins. Single-cell Gel Electrophoresis Applied to the Analysis of UV-C Damage and Its Repair in Human Cells. *International Journal of Radiation Biology*, 62(3):313–320, January 1992. 73, 130

[108] David B. Hall, Patrick Underhill, and John M. Torkelson. Spin coating of thin and ultrathin polymer films. *Polymer Engineering & Science*, 38(12):2039–2045, December 1998. 76, 148

[109] J. Hohlfeld, J.G. Müller, S.-S. Wellershoff, and E. Matthias. Time-resolved thermoreflectivity of thin gold films and its dependence on film thickness. *Applied Physics B: Lasers and Optics*, 64(3):387–390, March 1997. 76

[110] Stanley L. Shapiro, editor. *Ultrashort Light Pulses*, volume 18 of *Topics in Applied Physics*. Springer Berlin Heidelberg, Berlin, Heidelberg, 1977. 83

[111] Martin O Culjat, David Goldenberg, Priyamvada Tewari, and Rahul S Singh. A review of tissue substitutes for ultrasound imaging. *Ultrasound in medicine & biology*, 36(6):861–73, June 2010. 97, 110

[112] Xiaoyan Ma, Jun Q Lu, R Scott Brock, Kenneth M Jacobs, Ping Yang, and Xin-Hua Hu. Determination of complex refractive index of polystyrene microspheres from 370 to 1610 nm. *Physics in Medicine and Biology*, 48(24):4165, 2003. 112

[113] D. M. Smith and T. A. Wiggins. Sound speeds and laser induced damage in polystyrene. *Appl. Opt.*, 11(11):2680–2683, Nov 1972. 112

[114] F Lanni, A S Waggoner, and D L Taylor. Structural organization of interphase 3T3 fibroblasts studied by total internal reflection fluorescence microscopy. *The Journal of cell biology*, 100(4):1091–102, April 1985. 134

[115] Richard J Smith, Roger A Light, Steve D Sharples, Nicholas S Johnston, Mark C Pitter, and Mike G Somekh. Multichannel, time-resolved picosecond laser ultrasound imaging and spectroscopy with custom complementary metal-oxide-semiconductor detector. *The Review of scientific instruments*, 81(2):024901, February 2010. 141

[116] Philip C. D. Hobbs. Ultrasensitive laser measurements without tears. *Applied Optics*, 36(4):903, February 1997. 142

[117] K F Webb. Condenser-free contrast methods for transmitted-light microscopy. *Journal of microscopy*, 257(1):8–22, January 2015. 144

[118] H. T. Grahn, D. A. Young, H. J. Maris, J. Tauc, J. M. Hong, and T. P. Smith. Sound velocity and index of refraction of AlAs measured by picosecond ultrasonics. *Applied Physics Letters*, 53(21):2023, November 1988. 150

[119] Richard D. Averitt, Sarah L. Westcott, and Naomi J. Halas. Linear optical properties of gold nanoshells. *Journal of the Optical Society of America B*, 16(10):1824, October 1999. 151

[120] Pierre Marquet, Benjamin Rappaz, Pierre J. Magistretti, Etienne Cuche, Yves Emery, Tristan Colomb, and Christian Depeursinge. Digital holographic microscopy: a noninvasive contrast imaging technique allowing quantitative visualization of living cells with subwavelength axial accuracy. *Optics Letters*, 30(5):468, March 2005. 153

[121] F.L. McCrackin, E. Passaglia, R.R. Stromberg, and H.L. Steinberg. Treasure of the Past VII: Measurement of the thickness and refractive index of very thin films and the optical properties of surfaces by ellipsometry. *Journal of Research of the National Institute of Standards and Technology*, 106(3):589, May 2001. 153

[122] Y E Korchev, C L Bashford, M Milovanovic, I Vodyanoy, and M J Lab. Scanning ion conductance microscopy of living cells. *Biophysical journal*, 73(2):653–8, August 1997. 154

[123] Gabriel Popescu, Lauren P. Deflores, Joshua C. Vaughan, Kamran Badizadegan, Hidenao Iwai, Ramachandra R. Dasari, and Michael S. Feld. Fourier phase microscopy for investigation of biological structures and dynamics. *Optics Letters*, 29(21):2503, November 2004. 156

[124] Michael A. Choma, Audrey K.. Ellerbee, Changhuei Yang, and Joseph A.. Izatt. Spectral domain phase microscopy. In *Biomedical Topical Meeting*, page SC5, Washington, D.C., April 2004. OSA. 156

[125] A. Barty, K. A. Nugent, D. Paganin, and A. Roberts. Quantitative optical phase microscopy. *Optics Letters*, 23(11):817, June 1998. 156

[126] Christopher J. Mann, Lingfeng Yu, Chun-Min Lo, and Myung K. Kim. High-resolution quantitative phase-contrast microscopy by digital holography. *Optics Express*, 13(22):8693, October 2005. 156

[127] Gabriel Popescu, Takahiro Ikeda, Ramachandra R. Dasari, and Michael S. Feld. Diffraction phase microscopy for quantifying cell structure and dynamics. *Optics Letters*, 31(6):775, March 2006. 156

[128] Wonshik Choi, Christopher Fang-Yen, Kamran Badizadegan, Seungeun Oh, Niyom Lue, Ramachandra R Dasari, and Michael S Feld. Tomographic phase microscopy. *Nature methods*, 4(9):717–9, September 2007. 156

[129] Fernando Pérez-Cota, Richard J. Smith, Emilia Moradi, Leonel Marques, Kevin F. Webb, and Matt Clark. Thin-film optoacoustic transducers for subcellular Brillouin oscillation imaging of individual biological cells. *Applied Optics*, 54(28):8388, September 2015. 162

[130] T.E.G. Alvarez-Arenas. Acoustic impedance matching of piezoelectric transducers to the air. *IEEE Transactions on Ultrasonics, Ferroelectrics and Frequency Control*, 51(5):624–633, May 2004. 166